

Final Report for the Grant Entitled

Bio-Inspired Sensing and Imaging of Polarization Information in Nature

Grant Number FA9550-05-1-0052

Duration: January 1, 2005 till December 31, 2007

PI: Nader Engheta

Co-Pis: Edward N. Pugh Jr., and Jan Van der Spiegel

Department of Electrical and Systems Engineering

University of Pennsylvania

Philadelphia, Pennsylvania 19104

Abstract

Our unaided eyes can detect two of the characteristics of image-forming visible light from a scene, namely, the intensity and the wavelength, which can then be encoded into perceptual qualities of brightness and color. Our eyes, however, are effectively blind to the third characteristic of light, its polarization. It is well known, however, that several species of animals have visual systems capable of detecting light's polarization and using the information so extracted. Understanding the biophysical mechanism behind the polarization vision and reverse engineering its functionality and utility leads to exciting novel methods and techniques in sensing and imaging with various applications. Motivated and inspired by the features of polarization-sensitive visual systems in nature, in our group we have been developing various man-made, non-invasive imaging methodologies, sensing schemes, camera systems, and visualization and display schemes that have shown exciting and promising outcomes with useful applications in system designs. These techniques provide better target detection, enhanced visibility in otherwise low-contrast conditions, longer detection range in optically scattering media, polarization-sensitive adaptation based on changing environments, surface deformation-variation detection (e.g., detection of finger prints on a smooth surface using polarization-based vision), "seeing" objects in shadows, and other novel outcomes and applications. During our efforts supported by this grant, we have investigated various exciting possibilities of bio-inspired polarization imaging with numerous potential applications. Our findings are described in the attached published papers.

REPORT DOCUMENTATION PAGE					Form Approved OMB No. 0704-0188	
<p>The public reporting burden for this collection of information is estimated to average 1 hour per response, including the time for reviewing instructions, searching existing data sources, gathering and maintaining the data needed, and completing and reviewing the collection of information. Send comments regarding this burden estimate or any other aspect of this collection of information, including suggestions for reducing the burden, to the Department of Defense, Executive Service Directorate (0704-0188). Respondents should be aware that notwithstanding any other provision of law, no person shall be subject to any penalty for failing to comply with a collection of information if it does not display a currently valid OMB control number.</p> <p>PLEASE DO NOT RETURN YOUR FORM TO THE ABOVE ORGANIZATION.</p>						
1. REPORT DATE (DD-MM-YYYY)		2. REPORT TYPE			3. DATES COVERED (From - To)	
4. TITLE AND SUBTITLE				5a. CONTRACT NUMBER		
				5b. GRANT NUMBER		
				5c. PROGRAM ELEMENT NUMBER		
6. AUTHOR(S)				5d. PROJECT NUMBER		
				5e. TASK NUMBER		
				5f. WORK UNIT NUMBER		
7. PERFORMING ORGANIZATION NAME(S) AND ADDRESS(ES)					8. PERFORMING ORGANIZATION REPORT NUMBER	
9. SPONSORING/MONITORING AGENCY NAME(S) AND ADDRESS(ES)					10. SPONSOR/MONITOR'S ACRONYM(S)	
					11. SPONSOR/MONITOR'S REPORT NUMBER(S)	
12. DISTRIBUTION/AVAILABILITY STATEMENT						
13. SUPPLEMENTARY NOTES						
14. ABSTRACT						
15. SUBJECT TERMS						
16. SECURITY CLASSIFICATION OF:			17. LIMITATION OF ABSTRACT	18. NUMBER OF PAGES	19a. NAME OF RESPONSIBLE PERSON	
a. REPORT	b. ABSTRACT	c. THIS PAGE			19b. TELEPHONE NUMBER (Include area code)	

INSTRUCTIONS FOR COMPLETING SF 298

1. REPORT DATE. Full publication date, including day, month, if available. Must cite at least the year and be Year 2000 compliant, e.g. 30-06-1998; xx-06-1998; xx-xx-1998.

2. REPORT TYPE. State the type of report, such as final, technical, interim, memorandum, master's thesis, progress, quarterly, research, special, group study, etc.

3. DATES COVERED. Indicate the time during which the work was performed and the report was written, e.g., Jun 1997 - Jun 1998; 1-10 Jun 1996; May - Nov 1998; Nov 1998.

4. TITLE. Enter title and subtitle with volume number and part number, if applicable. On classified documents, enter the title classification in parentheses.

5a. CONTRACT NUMBER. Enter all contract numbers as they appear in the report, e.g. F33615-86-C-5169.

5b. GRANT NUMBER. Enter all grant numbers as they appear in the report, e.g. AFOSR-82-1234.

5c. PROGRAM ELEMENT NUMBER. Enter all program element numbers as they appear in the report, e.g. 61101A.

5d. PROJECT NUMBER. Enter all project numbers as they appear in the report, e.g. 1F665702D1257; ILIR.

5e. TASK NUMBER. Enter all task numbers as they appear in the report, e.g. 05; RF0330201; T4112.

5f. WORK UNIT NUMBER. Enter all work unit numbers as they appear in the report, e.g. 001; AFAPL30480105.

6. AUTHOR(S). Enter name(s) of person(s) responsible for writing the report, performing the research, or credited with the content of the report. The form of entry is the last name, first name, middle initial, and additional qualifiers separated by commas, e.g. Smith, Richard, J, Jr.

7. PERFORMING ORGANIZATION NAME(S) AND ADDRESS(ES). Self-explanatory.

8. PERFORMING ORGANIZATION REPORT NUMBER. Enter all unique alphanumeric report numbers assigned by the performing organization, e.g. BRL-1234; AFWL-TR-85-4017-Vol-21-PT-2.

9. SPONSORING/MONITORING AGENCY NAME(S) AND ADDRESS(ES). Enter the name and address of the organization(s) financially responsible for and monitoring the work.

10. SPONSOR/MONITOR'S ACRONYM(S). Enter, if available, e.g. BRL, ARDEC, NADC.

11. SPONSOR/MONITOR'S REPORT NUMBER(S). Enter report number as assigned by the sponsoring/monitoring agency, if available, e.g. BRL-TR-829; -215.

12. DISTRIBUTION/AVAILABILITY STATEMENT. Use agency-mandated availability statements to indicate the public availability or distribution limitations of the report. If additional limitations/ restrictions or special markings are indicated, follow agency authorization procedures, e.g. RD/FRD, PROPIN, ITAR, etc. Include copyright information.

13. SUPPLEMENTARY NOTES. Enter information not included elsewhere such as: prepared in cooperation with; translation of; report supersedes; old edition number, etc.

14. ABSTRACT. A brief (approximately 200 words) factual summary of the most significant information.

15. SUBJECT TERMS. Key words or phrases identifying major concepts in the report.

16. SECURITY CLASSIFICATION. Enter security classification in accordance with security classification regulations, e.g. U, C, S, etc. If this form contains classified information, stamp classification level on the top and bottom of this page.

17. LIMITATION OF ABSTRACT. This block must be completed to assign a distribution limitation to the abstract. Enter UU (Unclassified Unlimited) or SAR (Same as Report). An entry in this block is necessary if the abstract is to be limited.

Adaptive algorithms for two-channel polarization sensing under various polarization statistics with nonuniform distributions

Konstantin M. Yemelyanov, Shih-Schön Lin, Edward N. Pugh, Jr., and Nader Engheta

The polarization of light carries much useful information about the environment. Biological studies have shown that some animal species use polarization information for navigation and other purposes. It has been previously shown that a bioinspired polarization-difference imaging (PDI) technique can facilitate detection and feature extraction of targets in scattering media. It has also been established [J. Opt. Soc. Am. A **15**, 359 (1998)] that polarization sum and polarization difference are the optimum pair of linear combinations of images taken through two orthogonally oriented linear polarizers of a scene having a uniform distribution of polarization directions. However, in many real environments the scene has a nonuniform distribution of polarization directions. Using principal component analysis of the polarization statistics of the scene, we develop a method to determine the two optimum information channels with unequal weighting coefficients that can be formed as linear combinations of the images of a scene taken through a pair of linear polarizers not constrained to the horizontal and vertical directions of the scene. We determine the optimal orientations of linear polarization filters that enhance separation of a target from the background, where the target is defined as an area with distinct polarization characteristics as compared to the background. Experimental results confirm that in most situations *adaptive* PDI outperforms conventional PDI with fixed channels. © 2006 Optical Society of America

OCIS codes: 260.5430, 110.2970, 330.1880, 100.2960, 330.7320.

1. Introduction

Polarization is an intrinsic feature of light that provides valuable information about a scene beyond that provided by the scene's spectral (color) and intensity distributions. Polarized light has been studied extensively since Fresnel's investigations of the wave theory, and is important in many areas of modern technology (see, e.g., Refs. 1–4). Polarization information has proven useful in several fields, including computer vision,^{5,6} target detection, particularly in imaging targets in scattering media, such as water, fog,

etc., in feature extraction,^{7–22} and in material classification.^{23,24} Polarization parameters, e.g., Stokes parameters, are in general more sensitive to the nature of a scattering surface than the total intensity is. In such a case, polarization imaging techniques offer the possibility of producing images with higher inherent visual contrast than conventional image processing of the intensity distribution.³

The polarization of light is not discernible to the unaided human eyes,²⁵ but polarization has been shown to provide valuable information to other species. In 1949, Nobel laureate Karl von Frisch established that honeybees through their perception of polarized light use the Sun as a compass through their perception of the polarization pattern of light scattered from the sky.^{26,27} After von Frisch's discovery, other researchers began to investigate polarization vision and found it in many different species, including amphibians, arthropods, desert ants, octopuses, and probably fish (see, e.g., Refs. 28–41). These animals use polarization information in many different ways, e.g., navigation, detecting water surfaces, enhancing visibility (similar to colors), and perhaps even for mutual communication.

From its utilization by animals, it is clear that the

K. M. Yemelyanov (kostya@seas.upenn.edu), S.-S. Lin, and N. Engheta are with the Department of Electrical and Systems Engineering, University of Pennsylvania, 200 South 33rd Street, Philadelphia, Pennsylvania 19104. N. Engheta is also with the Institute of Neurological Sciences, University of Pennsylvania, 200 South 33rd Street, Philadelphia, Pennsylvania 19104. E. N. Pugh, Jr. is with the F. M. Kirby Center for Molecular Ophthalmology and the Institute of Neurological Sciences, University of Pennsylvania, 422 Curie Boulevard, Philadelphia, Pennsylvania 19104.

Received 4 November 2005; revised 11 March 2006; accepted 13 March 2006; posted 14 April 2006 (Doc. ID 65745).

0003-6935/06/225504-17\$15.00/0

© 2006 Optical Society of America

pattern of polarization in an image of a scene is a potentially rich source of information. While the human eye is “polarization blind,” man-made imaging systems have been developed to collect polarization information from scenes.^{5,6} An important issue for such systems is how to process and display the polarization information after it is collected by the imaging system to enhance our vision of the scene. Inspired by polarization vision of certain animal species, in earlier studies, our group introduced,^{12,42,43} polarization-difference imaging (PDI) processing.⁴⁴ We demonstrated that optical imaging systems utilizing PDI techniques may help the detection of targets in scattering media even when the fraction of the light is polarized by only a few percent, and that such enhancement can increase by up to threefold the distance over which targets can be reliably detected near threshold visibility.^{12,42,43} We have also investigated the issue of optimal representation of polarization information for the polar-blind human eye.^{43–45}

The idea that polarization vision may involve adaptation to the environmental polarization is bioinspired as well. Insects employ a retinal filter consisting of an array of ommatidia (polarization-sensitive photoreceptors) that is approximately matched to the polarization pattern of the sky.³² This filter works as follows: The summed output from all the polarization analyzers of the polarization-sensitive area reaches a maximum when a match between the receptor array and the celestial pattern has been approximately achieved. This provides the insect with the information of how to align its longitudinal body axis with the symmetry plane of the sky. To find a proper direction, the insect has to change its orientation and perform a check of the polarization pattern for each angle of orientation.^{46,47}

Inspired by the concept of matched filters^{31,32} we develop a polarization imaging technique based on PDI, but that is adaptable to the environmental conditions, i.e., to the polarization background of a scene. The proposed polarization-based system adjusts itself to enhance the segregation of targets from the background in a manner dependent on the polarization statistics of the scene.

The paper is organized as follows: in Section 2, we give a brief overview of the polarization concept and define the polarization parameters used in the paper. In Section 3, we describe the adaptive polarization-difference imaging (APDI) algorithm. Section 4 is devoted to the validation of the proposed technique, employing both experiments and simulations. In Section 4, we illustrate the performance of the algorithm in target-against-background detection using the experimental data obtained in a natural environment. In Section 5, we apply the APDI algorithm to a scene taken under natural illumination conditions. In Section 6, we propose an APDI-based method that may be used in surveillance systems, compare APDI with several other methods in polarization-based imaging, and discuss the performance of the algorithm. Finally in Section 7, we present our conclusions.

2. Physics of Polarization Imaging

The polarization of the local field of a monochromatic coherent light source can be represented as a superposition of two mutually orthogonal wave components. A phase difference between these components produces a linearly, elliptically, or circularly polarized wave with its polarization direction determined by the relative strengths of the components. Since human eyes and most conventional camera sensors can only detect the total light intensity collected at each pixel during an exposure time many times longer than the oscillation frequency, when the light energy is uniformly distributed over all polarization directions, the detected signal will be the same for any polarization direction. Such light is called unpolarized and emitted by most common light sources, including the Sun or man-made incandescent light sources. The local polarization signal at the surface of a sensor (which cannot detect phase information) can be described as a combination of unpolarized and completely linearly polarized components.

Assuming that a perfect linear polarizer is placed in front of a normal polarization-insensitive device, such as a CCD or film camera, the observed intensity $I(x, y, \varphi)$ at the pixel located at (x, y) is in general a function of the angle φ that polarization analyzer makes with a reference direction, and can be described as

$$I(x, y, \varphi) = I_U(x, y)(1 + p(x, y)\cos\{2[\theta(x, y) - \varphi]\}), \quad (1)$$

where I_U is half of the total pixel intensity, and p is the degree of *linear* polarization defined as $[I_{\max}(x, y) - I_{\min}(x, y)]/[I_{\max}(x, y) + I_{\min}(x, y)]$, where $I_{\max}(x, y)$ and $I_{\min}(x, y)$ denote at each pixel (x, y) , respectively, the maximum and minimum observed intensity within a full rotation of the analyzer. (We note that this definition of degree of linear polarization, which is more suitable for wideband signals used here, is different from what is used as the degree of polarization in the context of the Stokes parameters.⁴⁹ Throughout this paper, we use the horizon as the reference direction, and angles increase counterclockwise relative to the direction of the horizon.

As is evident from Eq. (1), at each pixel of the image of a scene, the polarization (and intensity) of the impinging light is characterized by three independent parameters: thus to obtain complete information about the polarization features of the object, at least three measurements of light intensity at different angles φ are required. These measurements can be made either simultaneously by three CCD cameras, such that each camera has a fixed polarizer set at a different angle, or, assuming the scene is stable over time, by one camera, taking images sequentially through a polarizer oriented at three different angles. Our computational algorithm can be used with either measurement method after proper calibration.

Consider three images of a scene, I_0, I_{45}, I_{90} , corresponding to three angles of orientation of the linear

polarizer, namely, $\varphi = 0^\circ$, 45° , and 90° with respect to the reference direction. From these three images, we can calculate I_U , p , and θ at each image point as follows:

$$\begin{aligned} I_U(x, y) &= \frac{I_0(x, y) + I_{90}(x, y)}{2}, \\ p(x, y) &= \left\{ \left[1 - \frac{I_{45}(x, y)}{I_U(x, y)} \right]^2 + \left[1 - \frac{I_{90}(x, y)}{I_U(x, y)} \right]^2 \right\}^{1/2}, \\ \theta(x, y) &= \frac{1}{2} \tan^{-1} \left[\frac{I_U(x, y) - I_0(x, y)}{I_U(x, y) - I_{45}(x, y)} \right]. \end{aligned} \quad (2)$$

Once the parameters I_U , p , and θ are computed for each pixel of the scene image, one can reconstruct the image intensity that would be observed for any angle φ using Eq. (1), even though no actual pictures are taken with a polarizer oriented at φ .

3. Concept of Adaptive Polarization-Difference Imaging

A. Polarization-Difference Imaging

The concept of PDI was introduced in earlier investigations of our research group.^{12,42–45} This idea has since been utilized by other research groups (see, e.g., Refs. 13, 18, 20, and 49–51). The original PDI system captures images of a scene at two orthogonal linear polarizations. Thus one obtains a pair of images, i.e., $I_0(x, y)$ and $I_{90}(x, y)$ taken at 0° and 90° orientation of the polarizer, respectively. The polarization-sum (PS) and polarization-difference (PD) images are linear combinations of the intensity images for the two orthogonal polarizations; thus given $I_0(x, y)$ and $I_{90}(x, y)$ one computes:

$$\begin{bmatrix} \text{PS}(x, y) \\ \text{PD}(x, y) \end{bmatrix} = \underbrace{\begin{bmatrix} 1 & 1 \\ 1 & -1 \end{bmatrix}}_T \begin{bmatrix} I_{90}(x, y) \\ I_0(x, y) \end{bmatrix}, \quad (3)$$

where T identifies the transformation matrix. For an ideal linear polarizer, the PS image is equivalent to a conventional intensity image.

Tyo⁵² has shown that the two image channels PS and PD given by Eq. (3) are the principal components (PCs) of a scene in which the polarization angle has a uniform distribution; thus in such cases, PS and PD are optimal channels in the information-theoretic sense of carrying maximally uncorrelated information about the scene. Tyo's ideas were developed in analogy with a principal component analysis (PCA) of trichromatic (three-cone pigment) color vision by Buchsbaum and Gottschalk.⁵³ In Tyo's analysis, as in that by Buchsbaum and Gottschalk,⁵³ the transformation matrix T in Eq. (3) is derived by applying PCA to the covariance matrix of the input channels [e.g., I_0 and I_{90} in Eq. (3)] for a broadband distribution of the relevant property (polarization, spectral distributions) over the ensemble of scenes. In these analyses, the principal component with the largest eigenvalue

is a same-signed sum of the input channels, while the remaining components are the "opponent," involving opposite-signed weighting coefficients in the transmission matrix.^{52,53} An interesting corollary to the optimality of PCA channels in information encoding is that the opponent channels can also be understood to be optimized for the detection of change relative to the average scene to which the first principal component is tuned; thus the opponent channel(s) in effect perform a common-mode rejection of the statistically average scene or background signal, and in doing so enhance the signal-to-noise ratio (SNR), and thus the detectability by the opponent channels of targets in a scene that differs in polarization statistics from the background. This duality in the sense of optimality of PCA-derived channels led us to seek the optimum channels for an arbitrary background scene.

B. Generalization of Polarized-Difference Imaging to Nonuniform Polarization Statistics

In real scenes, both the polarization orientation and the degree of linear polarization of the scene have non-uniform distributions. In such situations, the PD signal of Eq. (6) may not be the most useful signal for detecting targets against the average background. What would then be the appropriate image (i.e., a combination of signals) to reveal hidden polarization features of the scene and improve the target detection? Answering this question is the goal of this study.

Our approach to this goal has been to enable our imaging system to adapt to the polarization statistics of the background, so that if any changes occur in the scene they will pop out on one of the channels. The adaptation of the system to the polarization statistics of the background in effect performs a common-mode rejection of the background. In such an approach, it is assumed here that the system measures the polarization statistics of the scene in the two different stages: once when only the background is present, and again when a target is present with the background. Furthermore, in describing the ideal behavior of such a system, the target is considered as a perturbation of the background scene, i.e., a minor change that does not alter the overall polarization statistics (Subsection 4.C).

Consider the general case such that the probability density function of the polarization angle over the pixels is arbitrary. Assume that images of the scene with $M \times N$ pixels have been taken with two different orientations (not necessarily orthogonal) of the polarizer, i.e., $I_1 = I(\varphi_1)$ and $I_2 = I(\varphi_2)$. Here, we examine these two signals using the PCA technique.⁵⁵ According to PCA, the covariance matrix for such an arbitrary pair of images is defined as

$$C(\varphi_1, \varphi_2) = \begin{bmatrix} E(I_1 I_1) - E^2(I_1) & E(I_1 I_2) - E(I_1)E(I_2) \\ E(I_1 I_2) - E(I_1)E(I_2) & E(I_2 I_2) - E^2(I_2) \end{bmatrix}, \quad (4)$$

where $E(W) = 1/MN \sum_{m=1}^M \sum_{n=1}^N W(x_m, y_n)$ is the mean value taken over the ensemble of pixels in the images,

and W is equal to I_1, I_2 , or a product thereof. Once the eigenvalues (λ_1, λ_2) and the eigenvectors of the covariance matrix C are determined, the transformation matrix, which has the eigenvectors as its rows, is formed as follows:

$$T(\varphi_1, \varphi_2) = \begin{bmatrix} -\beta(\varphi_1, \varphi_2) & \alpha(\varphi_1, \varphi_2) \\ \alpha(\varphi_1, \varphi_2) & \beta(\varphi_1, \varphi_2) \end{bmatrix}. \quad (5)$$

The signs of the scalars α and β may be either positive or negative. The transformation matrix is formed in such a way that the first eigenvector corresponds to the largest eigenvalue. The principal component images are then computed as follows:

$$\begin{bmatrix} \text{PC}_1(\varphi_1, \varphi_2) \\ \text{PC}_2(\varphi_1, \varphi_2) \end{bmatrix} = T(\varphi_1, \varphi_2) \begin{bmatrix} I(\varphi_1) \\ I(\varphi_2) \end{bmatrix}. \quad (6)$$

By analogy with the transformation matrix of Tyo's conventional⁵⁵ PDI system, we consider PC_1 the adaptive analog of the PS signal, and the PC_2 the analog of the PD or opponent signal. We surmise that by analyzing the PC_2 image of a scene, certain important features, e.g., the detection of a target in the presence of a standard background will be enhanced.

All the parameters in Eqs. (5) and (6) are functions of the two polarizer angles, which in general, need not be orthogonal. For the case of a uniform distribution of polarization ellipse orientations over the scene, Eq. (6) reduces to Eq. (3). Our goal is to identify a pair of analyzer angles and a pair of weighting coefficients in Eq. (6) [i.e., the components of the eigenvectors shown in Eq. (5)], which yield a PC_2 image that optimally enhances the visualization of novel targets in a specific background scene. The term "optimum" here is used by analogy with the approach previously used in the analyses of color vision and polarization vision, as described in Section 3.A. In those analyses a formal assumption was made about the properties of the ensemble distribution of signals. In the present analysis, the role of the ensemble distribution is played by the polarization distribution of a specific background scene, and so we will put the adjective "optimum" in quotations, with the understanding that it is our task to demonstrate empirically that the method indeed yields a practical optimum separation of targets from the specific background.

C. Finding a Transformation Matrix to Adapt the Polarization-Difference Imaging System to a Specific Background

To adapt the PDI system to a specific background scene, we first obtain complete polarization information on the background. Specifically, we capture three images of the background scene for three orientations of the polarizer and then compute the polarization parameters that completely characterize the scene with Eq. (2). From these results, we can synthesize images of the scene corresponding to any angle of orientation φ of the polarizer with Eq. (1). It bears emphasis that the derivation of images correspond-

ing to various polarizer orientations φ from the initial set of three images is not linear.

The next step is to perform the principal components analysis as described in Subsection 3.B for a wide selection of pairs of angles φ_1, φ_2 , deriving the transformation matrix $T_{\text{BG}}(\varphi_1, \varphi_2)$ of Eq. (6) for the background for all pairs of angles. This yields a table or map of the derived polarization parameters over the 2D space of angles: i.e., $\alpha(\varphi_1, \varphi_2)$, $\beta(\varphi_1, \varphi_2)$, $\lambda_1(\varphi_1, \varphi_2)$, and $\lambda_2(\varphi_1, \varphi_2)$ for $0 \leq \varphi_1, \varphi_2 \leq 180^\circ$. It is reasonable to expect that the "optimum" pair of angles will be that with corresponding extreme eigenvalues. When the "optimum" pair of angles is chosen, then Eq. (9) is applied to the target scene. Here we consider, in particular, the following possible choices for the "optimum" pair (φ_1, φ_2) of polarizer orientations:

Case 1. The pair that maximizes the eigenvector component α (and it minimizes the magnitude of β).

Case 2. The pair that maximizes-minimizes the eigenvalues.

Case 3. The pair of orthogonal angles that has the preferential angle of the background polarization as its bisector.

Consideration of case 3 will allow a comparison between the conventional PD algorithm and the new adaptive algorithm here. In this case, as the preferential angle of polarization, we understand the angle corresponding to the modal value of the empirical distribution of polarization angles over the pixels corresponding to the background scene. We initially focus our investigation on cases 1 and 2, and then compare the results with those obtained for case 3. Practically, the APDI system images the scene at two consecutive stages. The information obtained at the first stage is assigned to the background scene (where no target is present), and the information obtained at the second stage is assigned to the target scene (where the target and the background are present).

4. Validations of the Adaptive Polarization-Difference Imaging Algorithm and the Selection of the Optimal Set of Parameters

To develop the APDI approach and examine its utility, we conducted several sets of experiments and simulations. The first set of images was taken in our laboratory—a controlled environment with stable illumination conditions. The target was a specially designed object with known polarization properties, and the background, as we will describe, was kept simple, while still exhibiting nonuniform polarization statistics. This enabled an accurate evaluation of the performance of APDI for the target detection. The second set of images was taken with real-life targets under natural illumination (sunlight).

A. Experimental Setup in the Laboratory

The laboratory experimental setup and a specially manufactured target are shown in Fig. 1. An incandescent 150 W lamp illuminated the cylindrical Plexiglas tank (12 in. in height and 16 in. in diameter) from a side. The tank was filled with a solution of

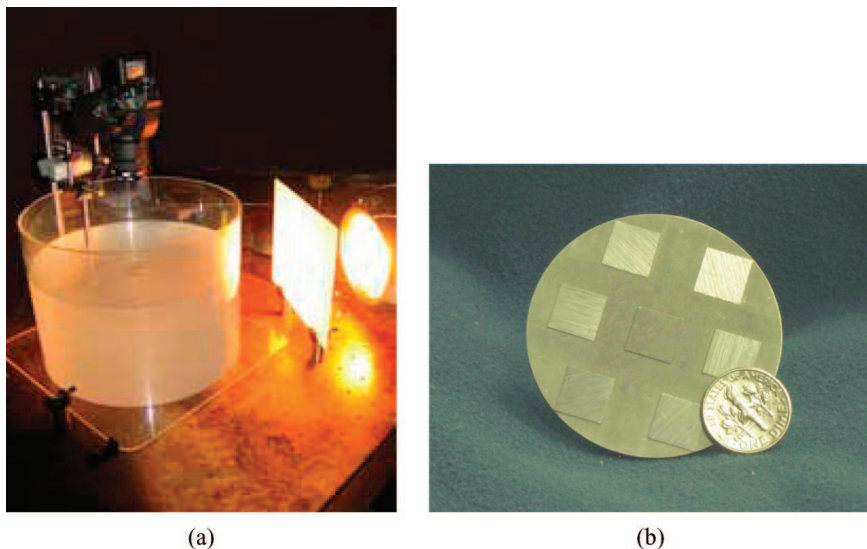


Fig. 1. (Color online) Layout of the experimental setup: (a) photograph of the setup, (b) 7-patch target together with a U.S. dime (10-cent coin).

10 ml of whole milk diluted in approximately 27 l of water. The height of the water level in the tank was 21 cm. This created a model of dispersive media (such a method of simulation of scattering media was originally used by Tyo *et al.*¹²). To produce Lambertian-type illumination, an opal glass diffuser was placed between the tank and the light source. The target was an aluminum disk 5.1 cm in diameter. The target surface was sandblasted, and there were seven 1 cm² square patches on it [see Fig. 1(b)]. The six outer patches were abraded with emory paper in such a way that they formed three orthogonally oriented pairs, i.e., 0° and 90°, 30° and 120°, and 60° and 150° (with respect to the vertical axis). Patches with orthogonal directions in the scratches are located diametrically opposite each other. The surface of the center patch was sandblasted in the same way as the base plate surface. The patches were raised a few mils from the base plate surface. The target was attached to the Plexiglas plate and faced up. The distance between the surface of the water and the plane of the aluminum disk was 55 mm. The target was observed with an Olympus E-10 SLR digital camera with a Sunpack 62 mm diameter glass polarizer attached in front of it. The images were taken sequentially for three different orientations of the polarizer, i.e., 0°, 45°, and 90° by manually rotating the polarizer between shots. All the images in the laboratory experiment were taken with an exposure time of 1 s and the *f* number of the camera equal to 4.0. During such exposure time, any fluctuations due to 120 Hz oscillations in the light source are therefore averaged out. The total time required to capture all three images was less than 10 s and was limited mainly by the time required to save the raw image of the scene to the camera's flash memory. The same digital camera and polarizer were used in our experiments in the natural (uncontrolled) environment.

All computer analyses in this study have been done using MATLAB software package with its Image Processing Toolbox. The captured images were stored in

an Olympus raw format (ORF), which gave us raw images of the scene, without the enhancements and modifications that most commercial digital cameras perform internally to make pictures look better. The Olympus E-10 has a single-chip color CCD with a RGGB Bayer primary color filter. For our computations, we extracted the R, G, and B components of the RGB (red–green–blue) output directly from the RGGB Bayer filter pattern response, so that the image had only ¼ of the total number of active pixels of the CCD chip (the G image is an average value of the two G filter responses). PCA may be applied to any pair of polarization channels capturing images representing one of the components (either R, G, B, or V). The V (luminance) component of the hue–saturation–luminance (HSV) was computed by the MATLAB Image Processing Toolbox and was, in fact, the maximum value of the R, G, or B channel at every pixel. In this paper, we present results that were obtained based on the V component of the images.

The camera zoom was adjusted in such a way that the area occupied by the aluminum disk was only a portion of the target scene. To obtain the background scene, we simply removed the aluminum disk from the scene while keeping all other experimental conditions, including the focusing distance of the camera, intact. The original image was cropped to 800 × 600 pixels for efficiency in analysis. The polarization statistics of the background scene are shown in Fig. 2. The histograms of the polarization parameters reveal a nonuniform distribution of the polarization statistics of the scene with the average degree of linear polarization of about 25%.

Throughout this paper, we present grayscale images with double precision, i.e., ranging from 0 to 1, where 0 corresponds to 0 and 1 corresponds to 255 of 8-bit gray scale. To assess the intrinsic noise of the camera, we made measurements with the camera lens covered by an opaque cap. The histograms of the standard background's half-intensity distribution, i.e., I_U are compared with the histogram of the dark

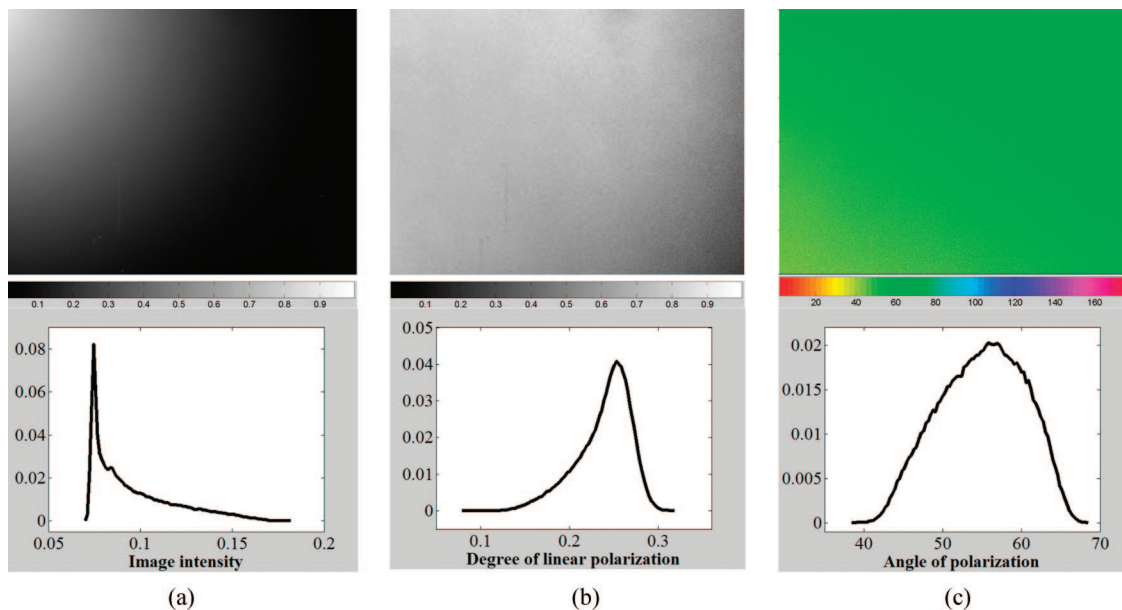


Fig. 2. (Color online) Normalized histograms of polarization parameters of the background: (a) half of total pixel intensity I_U ; (b) degree of linear polarization p ; (c) angle of polarization θ . Total number of pixels in the image was 800×600 . Images of I_U and p in the top row are stretched to cover an 8-bit gray-scale range. The reason we have systematic variations in the images of I_U and p is that the light comes from the one side (top left corner).

noise image in Fig. 3. The mean value of the camera-noise image is 0.5×10^{-2} and standard deviation is 7×10^{-4} , while for the background intensity image those parameters were 0.95×10^{-1} and 0.22×10^{-1} , respectively. Thus intrinsic camera noise is negligible in the standard conditions of the experiments.

B. Application of the Adaptive Polarization-Difference Imaging Algorithm to Images Obtained in a Controlled Environment

Equation (1) was applied to images of the background taken at three orientations ($\varphi = 0^\circ, 45^\circ$, and 90°) of the linear polarizer, and then images were generated for each angular orientation of the polarizer within the range from 0° to 180° with 5° steps (φ and $\varphi + 180^\circ$ are indistinguishable cases, since phase

information is not encoded by the camera). For each pair of images of the background corresponding to the pair of analyzer orientations (φ_1, φ_2) , we then extracted a full set of polarization parameters using PCA, i.e., $\alpha = \alpha(\varphi_1, \varphi_2)$, $\beta = \beta(\varphi_1, \varphi_2)$, $\lambda_1 = \lambda_1(\varphi_1, \varphi_2)$, and $\lambda_2 = \lambda_2(\varphi_1, \varphi_2)$ (Fig. 4).

The distributions of $\alpha(\varphi_1, \varphi_2)$ and $\beta(\varphi_1, \varphi_2)$ have similar forms and in particular have their maxima and minima at the similar locations in the space (φ_1, φ_2) . The eigenvalues λ_1 and λ_2 are symmetric functions of (φ_1, φ_2) , i.e., $\lambda_i(\varphi_1, \varphi_2) = \lambda_i(\varphi_2, \varphi_1)$ for $i = 1, 2$. The maximum and the minimum values of λ_1 are located on the line of symmetry ($\varphi_2 = \varphi_1$), which represents the situation when the angle of the linear polarizer for both source images is the same and is obviously not useful. Therefore case 2 reduces to the

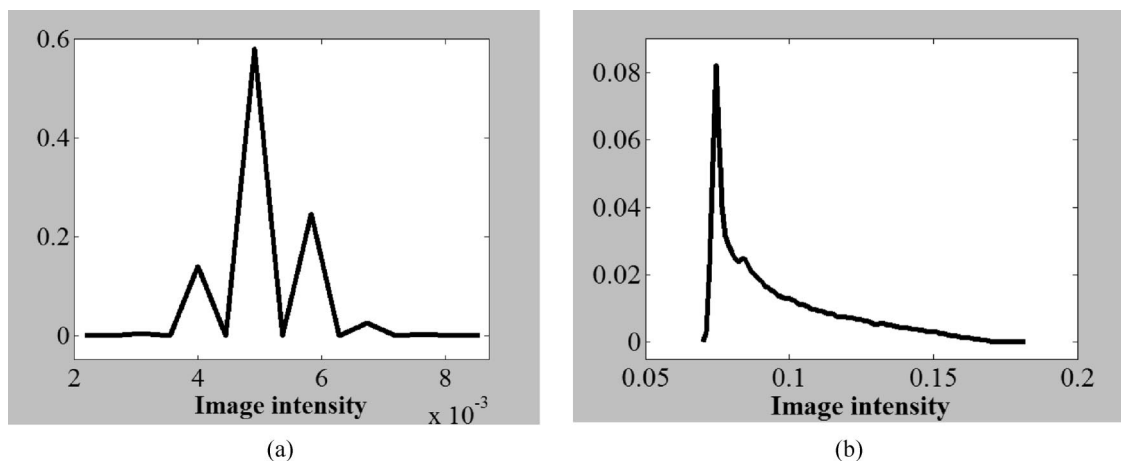


Fig. 3. Normalized histogram of the (a) dark noise of the camera compared to the normalized histogram (b) of the background image.

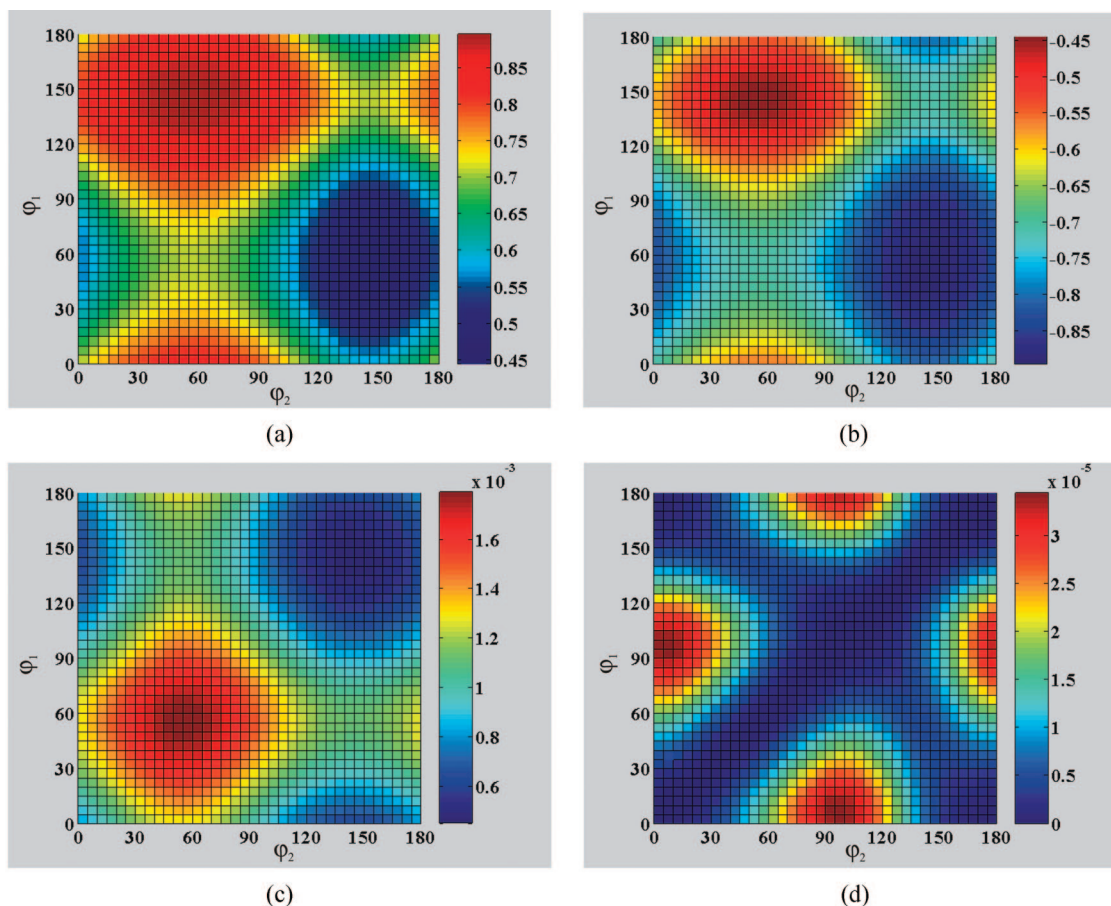


Fig. 4. (Color online) Distribution of the polarization parameters characterizing the standard background scene. Each panel presents a pseudocolor representation of the distribution of one of the parameters: (a) $\alpha(\varphi_1, \varphi_2)$, (b) $\beta(\varphi_1, \varphi_2)$, (c) $\lambda_1(\varphi_1, \varphi_2)$, (d) $\lambda_2(\varphi_1, \varphi_2)$. The scales for each parameter are provided to the right of each panel.

analysis of behavior of the smaller eigenvalue, i.e., λ_2 . The value of λ_2 represents the variance in the PC_2 image, suggesting that more interesting information can be obtained from the PC_2 image.

The APDI algorithm was applied to each target-background pair, and PC_1 and PC_2 images for all three cases described in Subsection 3.C were computed, and the corresponding parameters are given in Table 1. PC_1 and PC_2 images for all three cases are illustrated in Fig. 5. The PC_1 images for the three cases are very similar, and in particular, the nonuniform illumination of the scene is clearly visible in each. The PC_2 images in panels (b) and (c) of Fig. 5 are similar because the pairs of angles derived for cases 2 and 3 are close to each other, as well as the corresponding polarization parameters (see Table 1). However, the PC_2 image corresponding to case 1 [Fig. 5(a)]

is noticeably different: The margins of the disk are more clearly outlined, and the direction of scratches in all the patches (which vary in polarization orientation) are distinguishable. The clear segregation of the disk from the background in the PC_2 image is achieved in a large part due to the lower variance of the background scene in this channel, as we now describe.

In Fig. 6, we present normalized (i.e., unit area) histograms of the PC images for all cases considered. The distributions and, in particular, the standard deviations of the PC_1 images are very close for all three cases ($\sigma_i^2 \approx 0.5 \times 10^{-2}$). In contrast, for the PC_2 images the standard deviation for case 1 ($\sigma_1^2 = 3.68 \times 10^{-3}$) is more than 50% lower than in the other two cases (case 2, $\sigma_2^2 = 8.62 \times 10^{-3}$; case 3, $\sigma_3^2 = 8.53 \times 10^{-3}$). Thus the PC_2 image for case 1 has the smallest variance in the distribution of pixel intensities, suggesting that case 1 may provide an “optimum” set of adaptive parameters for the detection of novel targets in PC_2 images.

C. Performance Evaluation of Adaptive Polarization-Difference Imaging: Sensitivity Index

The selection of the “optimum” transformation matrix for a specific background should both lead to a

Table 1. Adaptive Parameters Corresponding to the Cases Considered for the Benchmark Target

Case	φ_1°	φ_2°	α	β	$\lambda_1 \times 10^{-3}$	$\lambda_2 \times 10^{-5}$
1	145	55	0.895	-0.446	1.116	0.611
2	95	5	0.680	-0.733	1.005	3.447
3	100	10	0.707	-0.707	1.004	3.327

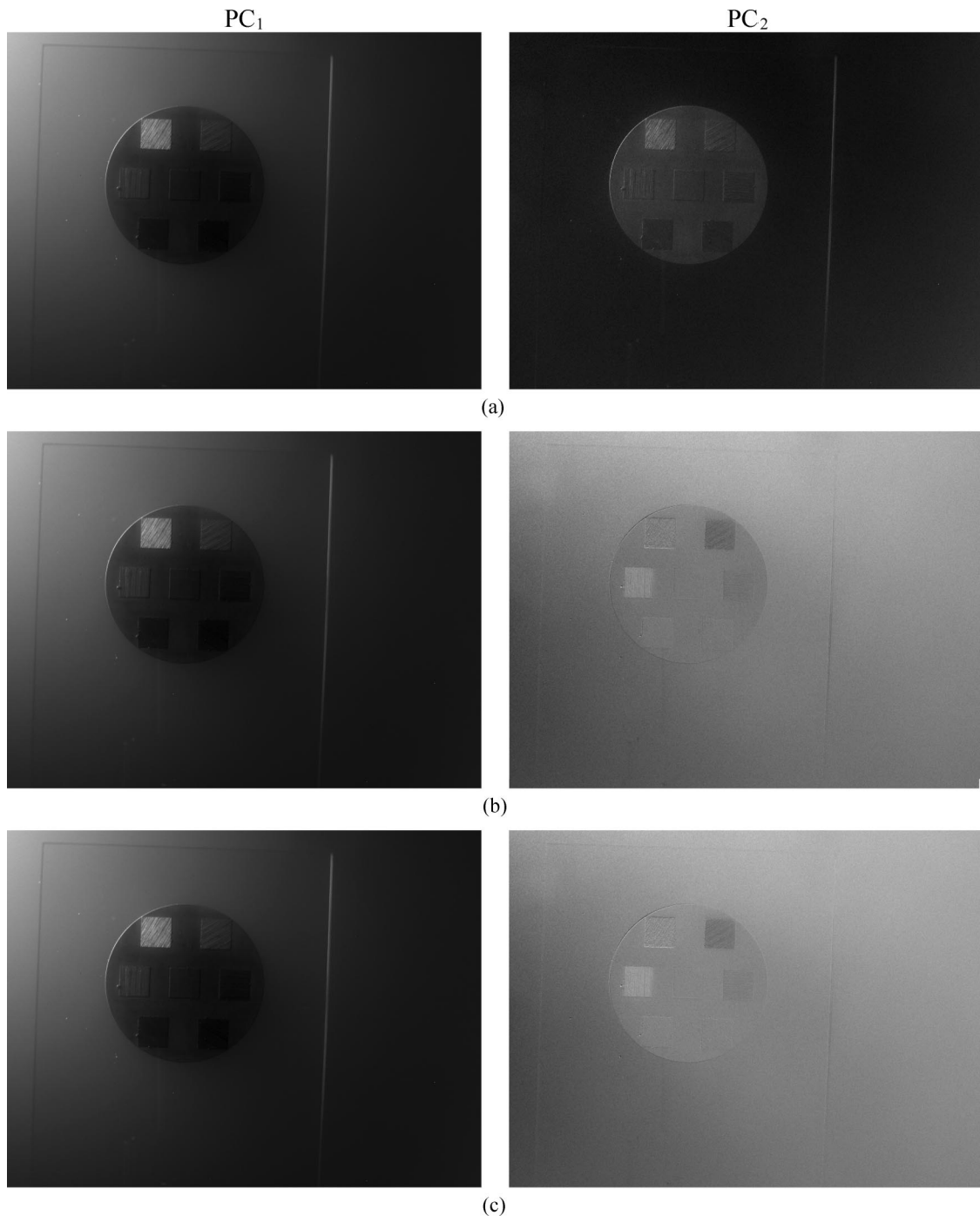


Fig. 5. Principal components of the scene corresponding to three cases of interest. Left column shows PC_1 , and right column PC_2 images, respectively. Panels (a)–(c) correspond to cases 1–3, respectively. All the images are linearly rescaled to exploit the 8-bit displayable range. The size of the images was 800×600 pixels.

minimum variance in the PC_2 image of the background, and enable targets with novel polarization properties to pop out in the PC_2 channel. To avoid relying only on the evaluation of the images of the targets by human viewing, we employed an objective numerical evaluation: the sensitivity index calculation. The sensitivity index is based on the signal-detection theory (SDT), which quantifies an observer's ability to discriminate a target from a background.⁵⁶ In

SDT, an observation taken at some moment may arise from a noise-alone distribution, or from the signal-plus-noise distribution, with the means of these distributions separated by a certain amount d_a specified in units of the standard deviations; d_a is called the sensitivity index. With an increase of d_a , the probability of successful target detection (a hit) will increase, since the overlap between the distributions decreases, and the probability of a false alarm will also

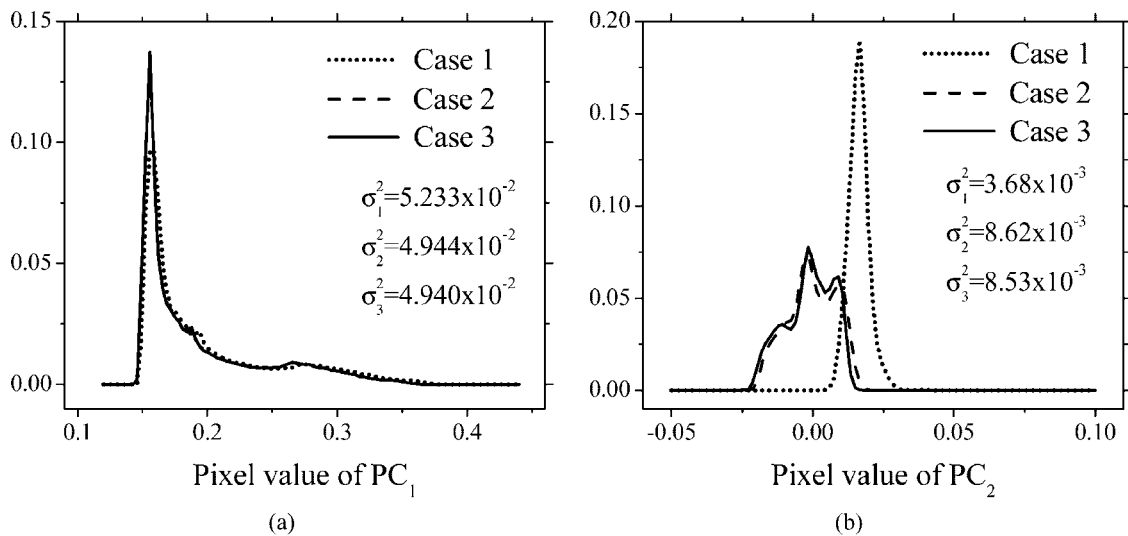


Fig. 6. Normalized histograms of (a) PC₁ and (b) PC₂ for all the cases shown as images in Fig. 5. The standard deviations of PCs for all three cases considered are shown in the figures.

decrease. In our study as the signal-plus-noise distribution, we consider the scene distribution including both the target and the background, while the noise-alone distribution is taken as the scene distribution without the target present.

To estimate d_a empirically, we performed a series of measurements with 3 min separation between each set. The experimental setup was as described in Subsection 4.A. We first captured 20 sets of images of the background alone, and then 20 sets of images of the background-plus-target scenes; each set of images is composed of three images collected at $\varphi = 0^\circ$, 45° , and 90° , allowing the derivation of an equivalent image for any polarizer orientation φ and PCA, yielding PC₁ and PC₂ images for cases 1–3. An observation for the SDT analysis was computed over two square regions of 5×5 pixels, determined by the imaged location of special portions of the target (Fig. 7). For each of the 20 sets of images of the background and the background-plus-target scenes, the average intensities of these regions in the PC₁ and PC₂ images were calculated. In summary, we ended up with 20

pairs of observations of the PC₁ and PC₂ values for these two specific regions of the scene for each of the three cases. We then estimated the sensitivity index as

$$d_a = \left| \frac{\mu_T - \mu_B}{\sqrt{(\sigma_T^2 + \sigma_B^2)/2}} \right|, \quad (7)$$

where μ_B and σ_B^2 are the mean and the variance of the background scene in the specific region, and μ_T and σ_T^2 are the mean and the variance of the same region when the target object is present.⁵⁶ The values of the sensitivity index for PC₂ images corresponding to the three cases (and the two target regions, respectively) were as follows: case 1, $d_a = 1.703$ and $d_a = 1.687$; case 2, $d_a = 0.772$ and $d_a = 1.371$; case 3, $d_a = 1.419$ and $d_a = 0.908$, respectively. Here, the first value of d_a in each case corresponds to the left-hand side target region, and the second value corresponds to the right-hand side region, (Fig. 7). The parameters determined by case 1 clearly yield a superior detectability of the polarization targets than those determined by cases 2 and 3. Remarkably, the case 1 PC₂ channel outperforms the PC₂ channel of the other two cases on *both* the left and the right targets, even though each of these other channels performs much better on one of the two targets. These observations suggest that the PC₂ channel generated with the maximum components of eigenvectors (α , β) correspond to the “optimum” pair of angles for the detection of the polarization targets against a polarized background.

5. Target Detection Against a Nonuniformly Polarized Background Under Natural Illumination Conditions

In addition to the experiments in the laboratory, we performed several experiments under natural illumination conditions. As in the laboratory, every experiment session includes capturing three images of both

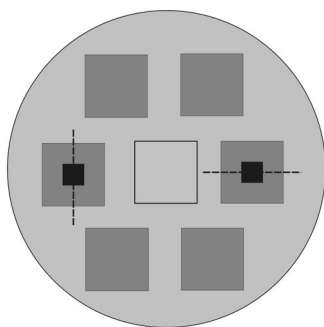


Fig. 7. Scheme of the specially created target where regions used for the sensitivity index calculation are marked in black. Dashed lines identify the direction of scratches in the specific patch. The left region is referred to as region one and the right region is referred to as region two, respectively.

the background scene and the target scene. Unlike the laboratory experiments, where the background was a largely a uniform scene, in this situation the background is a relatively complex one, and contains several different objects.

The first experiment presented here was done inside the Levine Hall of the University of Pennsylvania. The images for this experiment show the floor surface of the hall (Fig. 8). The scene consisted of the shadow region formed on the floor by the combined shadows of a person standing upright and the window frame. The rest of the scene was illuminated by the sunlight passing through the window glass. The camera was located opposite the window and elevated above the floor; thus the scene was illuminated by sunlight in such a way that the light beam coming from the Sun and a beam reflected from the scene formed the same plane. The floor was a dark gray color with a broad pattern. The target object was the translucent plastic case of a CD. We took three images of the background and of the target scenes. The camera settings were kept the same for both the background-only image sets and the image sets with the target in the scene. The exposure time for each image was $1/8$ and the f number of the camera was equal to 8. Figure 8 shows three polarization components (I_U , p , and θ) for both the background and the target scenes, placed side by side for easy comparison: The target object has a lower degree of polarization than the surrounding background.

Using the ADPI case 1 algorithm, the “optimum” pair of angles are found to be $\varphi_1 = 140^\circ$ and $\varphi_2 = 50^\circ$, with eigenvector components $\alpha = 0.9965$ and $\beta = -0.0834$. The histogram of the background angle of polarization shows that the preferential angle of polarization of the background is approximately $\theta_B = 140^\circ$, which means that the optimal angle pair is the angle of preferential polarization and the angle orthogonal to it. The angles corresponding to the maximum and the minimum of the larger eigenvalue (i.e., λ_1) are found in the bisector line of the eigenvalue surface, where λ_1^{\max} is located at the point $\varphi_1 = \varphi_2 = \theta_B$, and λ_1^{\min} is located at the point $\varphi_1 = \varphi_2 = \theta_B \pm 90^\circ$. This information can be useful: If the preferential polarization angle is known *a priori*, then the optimal angle pairs can be found directly without time-consuming computation. On the other hand, this can be an effective way to recover the preferred polarization direction in a scene.

Comparing the principal component images of the scene [panels (b) and (d) in Fig. 9], one may see a significant improvement in the target-background contrast of the PC_2 image over the conventional PD image. To have a more comprehensive comparison, we also included images that correspond to the pair of angles bringing the smaller eigenvalue to the maximum (case 2); i.e., consider images with the minimum variance in intensity. For this experiment, the maximum value of λ_2 is found at $\varphi_1 = 105^\circ$, $\varphi_2 = 15^\circ$, and the corresponding coefficients are $\alpha = 0.5016$, $\beta = -0.8650$. Principal component images created in

this case are also presented in Fig. 9 [panels (g) and (h)]. Although an improvement over the conventional PD image (case 3) is noticeable [comparing panels (d) and (h) in Fig. 9], the pair of angles determined by case 1 yields better results. Overall, then, we conclude that case 1 yields the “optimum” PC_2 channel.

6. Discussion

We have presented the mathematical basis of a novel adaptive PDI technique, and experimental results that demonstrate its performance in target detection applications. For scenes with uniform distributions of polarization parameters, APDI reduces to a conventional PDI technique. However, in many real-world situations, APDI will yield superior performance, so that targets with polarization features can be more readily detected against a background.

A. Summary of the Adaptive Polarization-Difference Imaging Algorithm

For the discussion to follow, it is useful to summarize the APDI algorithm:

1. Capture three images of the background scene for three different orientations φ of the linear polarization analyzer.
2. Process those three images and obtain complete polarization statistics of the background scene according to Eq. (2).
3. Synthesize polarization images of the scene for the full range of angles of orientation φ of the polarization analyzer using Eq. (1).
4. Perform PCA on all possible pairs of angles and obtain four adaptive parameters as the functions of angle of the polarizer's orientation, the two eigenvector components, and the two eigenvalues.
5. Find the “optimum” set of adaptive parameters (case 1) and create the transformation matrix of the background scene, i.e., $T_{BG}(\varphi_1^{\text{opt}}, \varphi_2^{\text{opt}})$.
6. Repeat steps 1 and 2 for the scene with the target present.
7. Synthesize a pair of polarization images of the target scene for optimal pair of angles $(\varphi_1^{\text{opt}}, \varphi_2^{\text{opt}})$ as found in step 5.
8. Using the transformation matrix that was obtained from the background scene, $T_{BG}(\varphi_1^{\text{opt}}, \varphi_2^{\text{opt}})$, create principal component images of the target scene according to Eq. (6).

Since the APDI algorithm deals with the polarization statistics of the scene, if the target occupies only a small portion of the scene, adaptive coefficients and optimal pairs of angles obtained from statistics of the background scene will differ little from those obtained from the statistics of the target scene. Thus the APDI algorithm may be applied to the target scene directly without gathering additional information from the background. However, if the target object occupies a significant portion of the image, a complete set of measurements of the background is required to segregate the target object from the background. Although in this study we dealt with scenes that had a nonuni-

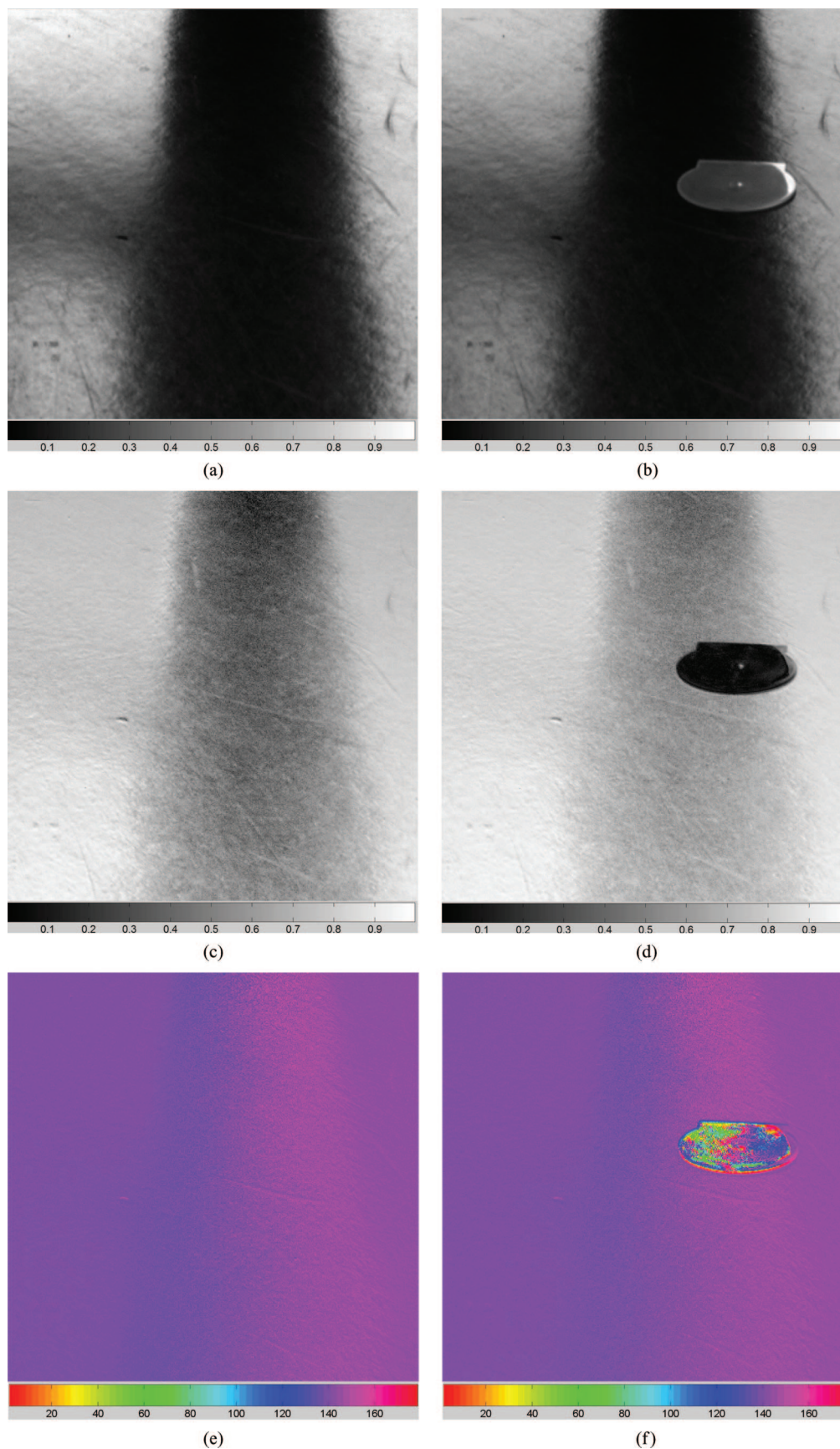


Fig. 8. Polarization components for the nontarget and target scenes of the experiments under natural lighting. The left panel shows I_U , p , and θ (top to bottom) images of the nontarget scene, and the right panel shows those for the target scene. The I_U plots in both cases are linearly rescaled to use the full 8-bit gray-scale display range.

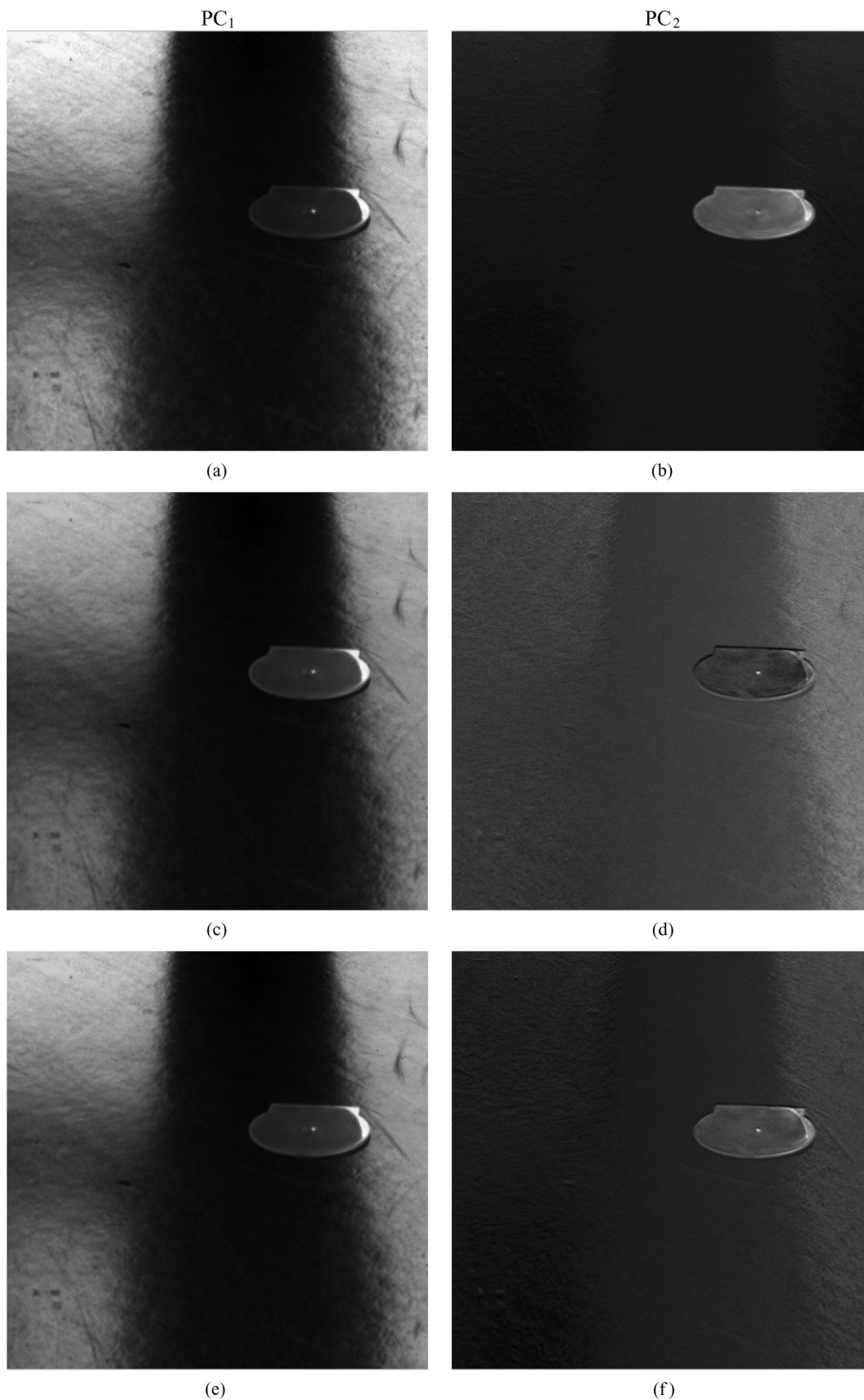


Fig. 9. Comparison in target detection between images obtained by our new adaptive algorithm and by the conventional PDI algorithm. They are the principal component images obtained from the images shown in Fig. 8. Panels (a) and (b) are PC₁ and PC₂ for case 1. Panels (c) and (d) are conventional PS and PD images (case 3). Panels (e) and (f) are PC₁ and PC₂ for case 2. All images were linearly rescaled to cover an 8-bit gray-level display range.

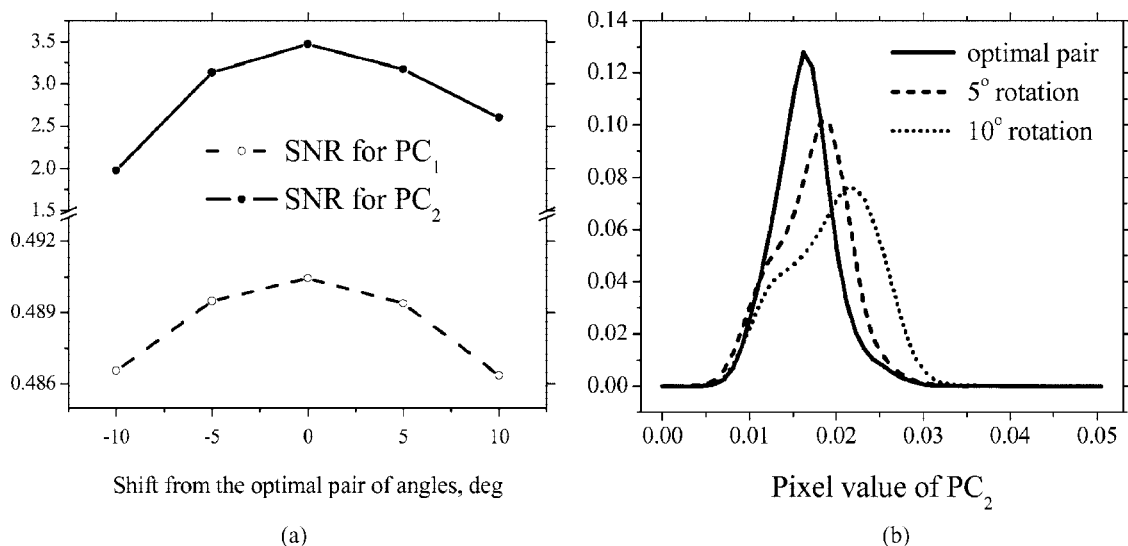


Fig. 10. (a) SNR for PC₁ and PC₂. Here, the signal is the area of the aluminum disk, and the noise is the rest area of the corresponding PC. (b) Normalized histograms of the PC₂ images with a shift from the optimal (case 1) pair of angles. Increasing variance in the PC₂ image with rotation of the optimal pair of angles is shown.

form distribution in polarization parameters, the polarization of the background had only one preferential direction of polarization. If the scene has two or more regions of significant areas that have different angles of preferential polarization, further improvements may be required, such as segmentation of the scene based on its polarization statistics. Such results will be reported in a subsequent paper.

The APDI algorithm is relatively fast and does not require significant computer resources. For the computer workstation with a Pentium 4 550 processor and 2 GB of RAM, the total computational time was about 30 s using the code written in MATLAB. Rewriting the code using a less resource aggressive programming language, such as C++ will significantly reduce the processing time. The time required for capturing the images may also be reduced. Currently, in the laboratory, we employ a setup where the rotation of the polarizer is performed by a stepping motor and the entire process can be controlled from the computer. Use of this setup will automate the procedure of capturing images and their transition to the computer.

B. Potential Applications

Based on the computer simulations and experiments presented above, we propose the APDI algorithm for use in the detection of targets with polarization features. To speed the process, the initial pair of angles may be selected such that one of the angles is equal to the preferential polarization angle of the background and the other angle is chosen to be orthogonal to the preferential angle. To ensure that the selected pair is "optimum," the calculations of adaptive coefficients for a few pairs of polarizer orientations around the selected point should be performed. The pair with the maximum component value of the eigenvectors is then used as the optimal pair. This approach may

significantly decrease the computational time, as is very important for real-time applications.

C. Sensitivity of the Adaptive Polarization-Difference Imaging Algorithm to the Rotation of the Pair of Angles

Since the APDI algorithm may be used as an effective tool in a visual surveillance system,⁵⁷ an important issue in this application is: "How sensitive are the adaptive pairs to the rotation of the polarization channels?"

Assume that by applying the APDI algorithm, an "optimum" set of (case 1) parameters has been found. Consider, then, rotating this pair by a certain angle clockwise or counterclockwise. Would it be possible to obtain a PC₂ image of the same quality? A simulation of the sensitivity of the APDI algorithm to such rotations was undertaken with the same set of experimental data reported above. The adaptive coefficients were applied to the pair of images corresponding to angles rotated by 5° and 10° from the "optimum" (case 1) pair. The goal was to check in which case the aluminum disk is better able to be detected against the surrounding water solution. For each case, we calculated the SNR, considering the output from the aluminum disk as the signal and the output from the surrounding water solution as the noise or background. Thus we derived

$$\text{SNR} = \left| \frac{\mu_D - \mu_W}{\sigma_W} \right|, \quad (8)$$

where μ_D is the mean value of pixels belonging to the aluminum disk, μ_W , σ_W are the mean value and the standard deviation of all the images except the aluminum disk, respectively. Figure 10(a) shows SNR for PC₁ and PC₂ corresponding to optimal pair angles and for pairs of angles rotated by 5° and 10° with respect to the optimal pair. We note that the SNR for the optimal

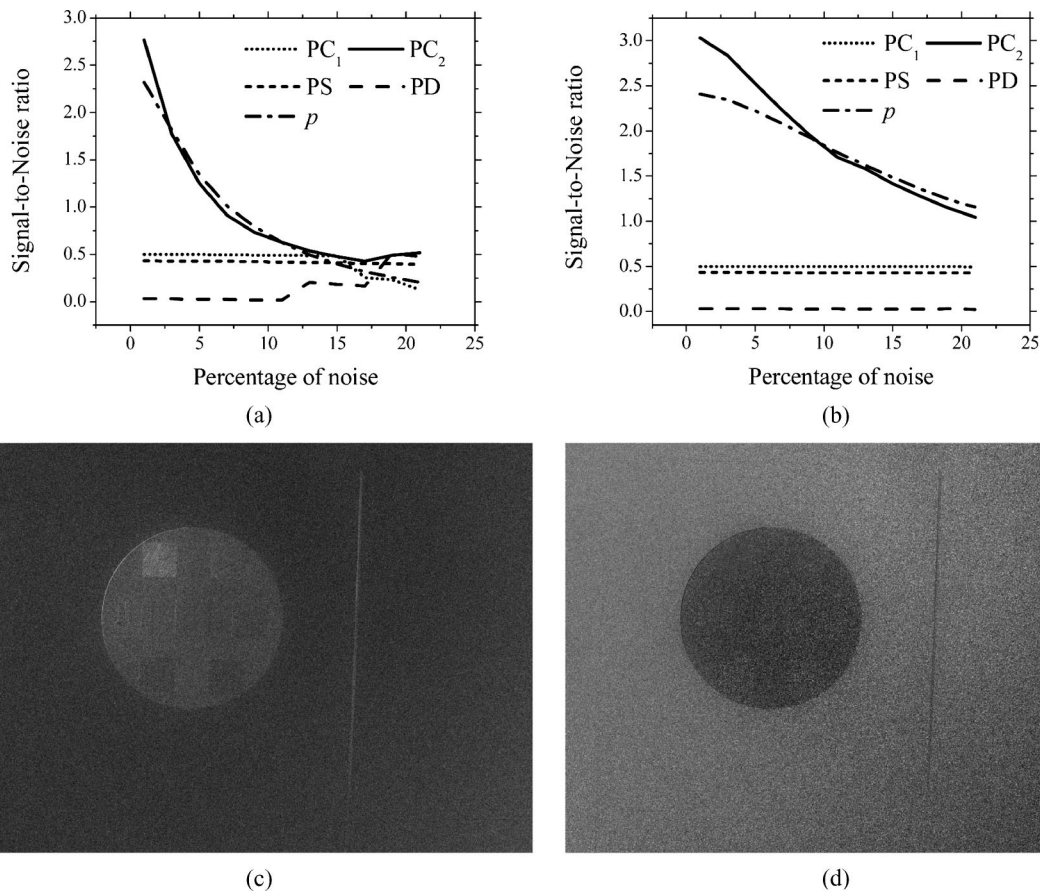


Fig. 11. SNRs for the PC_1 , PC_2 , PS , PD , and p with the presence of (a) artificially added Gaussian noise, and (b) white noise. Images of (c) PC_2 and (d) p for 5% of added Gaussian noise. Individual features of the aluminum disk, such as the appearance of patches, is better visible in the PC_2 image.

pair of angles is the highest and rapidly decreases with a rotating of the polarizers. With rotation of the angle pair, both the background level and its variance increase, while the intensity level of the target remains at approximately the same level. This can be seen in the histograms of the PC_2 images for the area surrounding the aluminum disk [see Fig. 10(b)]. These results show that a shift in the pair of angles from those determined by case 1 may decrease the SNR for a target object against the surrounding background.

D. Effects of Noise on the Performance of the Adaptive Polarization-Difference Imaging

In this subsection, we discuss the influence of noise on the performance of our technique. To evaluate the performance of APDI, we artificially added noise to a set of input images, I_0 , I_{45} , and I_{90} for both background and target scenes. We used two types of noises, i.e., white noise and Gaussian noise with mean values in both cases equal to the mean values of the input images. The standard deviation for the Gaussian noise was selected as a certain percentage of the dynamic range of the input images; i.e., the mean value of the input images was multiplied by a coefficient that varied from 0.01 to 0.21. For the white noise, the range of variations was the same as the standard deviation in the

case of the Gaussian noise. Once the noise was added to the input images, the polarization components were recovered, and then the APDI procedure as described in Subsection 6.A was done. For each percentage of noise, we calculated SNR according to Eq. (8) for both PCs corresponding to optimal pair of angles, for conventional PS and PD images, and for the degree of linear polarization p . The results are shown in Fig. 11. We may note that APDI is more sensitive to the presence of the Gaussian noise than to the white noise. After a certain amount of noise, the SNR calculated using the image of p becomes slightly higher than those for the PC_2 , although individual features of the target, such as patches are not detected in the image of p ; it is detected in PC_2 [compare panels (c) and (d) in Fig. 11, where the images are shown with an addition of 5% of noise]. With an increasing amount of noise, the performance of the APDI algorithm decreases, but still for the case of white noise even with the amount of noise about 20%, the performance of APDI is higher than those of the conventional PDI.

E. Adaptive Polarization-Difference Imaging Compared to Other Polarization Analysis Techniques

To produce the PD images, either a scene is illuminated by natural light and the scattered light is an-

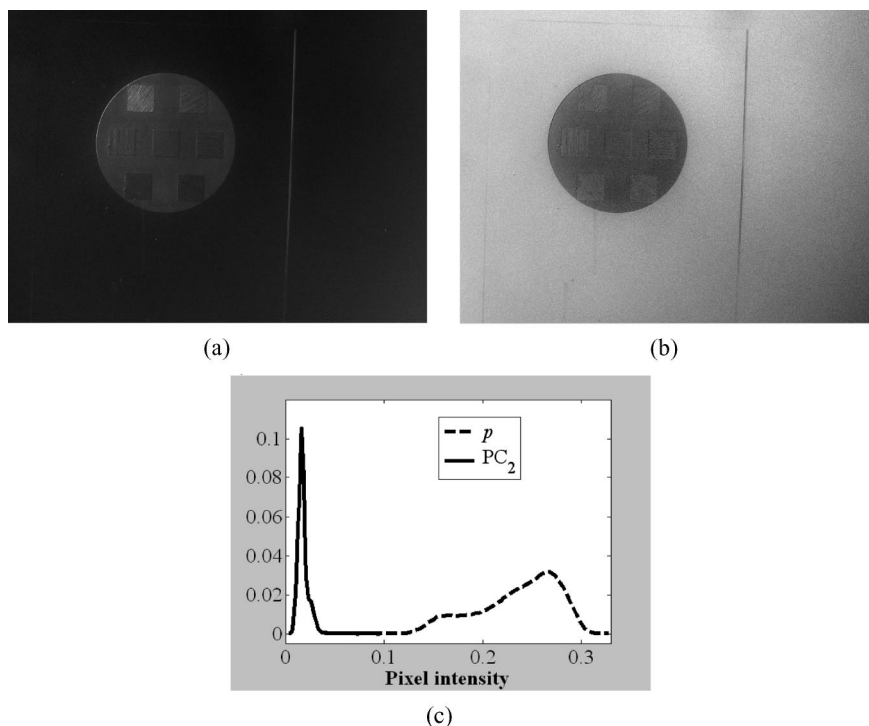


Fig. 12. Stretched images of (a) PC_2 and (b) p . (c) Normalized histograms of images shown in panels (a) and (b). Standard deviations for PC_2 and p are $\sigma^2 = 0.0054$ and $\sigma^2 = 0.041$, respectively.

alyzed with the two orthogonal polarizers, or a scene is illuminated with the two light sources of orthogonal polarizations. The idea of weighted subtraction of the two orthogonal components of the scene was first introduced by Walker *et al.*¹⁸ Their method involves subtraction of a scaled image obtained at one polarization from the oppositely polarized image, and shows improvement over methods in which subtraction is done without scaling. In this study, the image contrast was evaluated as a function of the scaling of the subtracted image, and the orthogonal polarization axes were fixed. In contrast, the APDI algorithm presented here adaptively selects two orientations of the polarizer, and also finds the “optimum” weighting of the resultant images by employing PCA to derive the transformation matrix [Eqs. (5) and (6)], and thereby the resultant PC_1 and PC_2 images.

Several publications have discussed the nonlinear aspects of polarization imaging techniques (see, e.g., Refs. 10, 11, and 13). The APDI algorithm proposed here is essentially linear once PCA analysis has been applied to the background [derivation of the images of the background corresponding to a full set of orientations of the polarizer involves the nonlinear equations, Eq. (1) and (2)]. An advantage of the APDI method is that it is readily applicable to many different kinds of scenes in which polarization affects image intensities, including scenes that include specular reflection (e.g., Fig. 9), underwater scenes (Fig. 5), and low-light scenes in which either natural or artificial illumination is used. Moreover, APDI can be implemented without using specialized equipment: only a digital camera and a polarizer are required for capturing images.

It has been proposed that images of the degree of

linear polarization in a scene^{6,7,19} [cf. $p(x, y)$ in Eq. (2)] may provide a valuable tool for the detection and discrimination of objects. Such images, no doubt, have considerable value, and can be readily implemented with the tools employed here. While we have not performed an exhaustive comparison, we can confidently assert that the signal obtained with PC_2 of APDI outperforms that obtained from p images in the cases we have examined; one such comparison is provided in Fig. 12. In this case, the variance of the background in the PC_2 image is about 1/10 that of the p image. As a result, the SNR calculated according to Eq. (8) is higher for the PC_2 versus the p image: 3.056 versus 2.417. Nonetheless, for the superior SNR of APDI, under conditions where speed is critical, use of the p image for rapid initial inspection should be quite valuable, and it bears emphasis that the p image data are automatically generated in the APDI algorithm.

7. Conclusions

We have developed a set of techniques to form an “optimum” linear combination for the polarization channels that is adapted to the polarization statistics of a scene. Utilizing the technique of PCA, we have determined an optimum linear combination of polarization channels [Eqs. (5) and (6)] to produce PC_2 images that efficiently provide information for discriminating a target with polarization properties from the background scene. The adaptive transformation is readily adjusted as the imaging system observes different environments or varying lighting conditions. The adaptive transformation is particularly suitable for environments with preferential polarization distribution. This approach may point to

an interesting research direction in the polarization vision in certain aquatic species, which may have detector arrays that act like an adaptive PC₂ channel. A further utility of the APDI system is that once the polarization information [see Eq. (2)] fully characterizing the background scene has been collected (e.g., by a surveillance system that routinely takes images at three orientations of a linear polarizer), the image data may be processed off-line to yield an optimum presentation of the polarization features of the scene that may otherwise escape attention.

This work was supported by the U.S. Air Force Office of Scientific Research (AFOSR), through grants F49620-01-1-0470, F49620-02-1-0140, FA9550-05-1-0052, and the Defense University Research Instrumentation Program (DURIP) grant F49620-02-1-0241. We thank the anonymous reviewers for their useful comments.

References and Notes

- W. A. Shurcliff, *Polarized Light, Production and Use* (Harvard U. Press, 1962).
- D. Goldstein, *Polarized Light* (Dekker, 2003).
- J. E. Solomon, "Polarization imaging," *Appl. Opt.* **20**, 1537–1544 (1981).
- S. Demos and R. Alfano, "Optical polarization imaging," *Appl. Opt.* **36**, 150–155 (1997).
- L. B. Wolff, "Polarization camera for computer vision with a beam splitter," *J. Opt. Soc. Am. A* **11**, 2935–2945 (1994).
- L. B. Wolff, T. A. Mancini, P. Pouliquen, and A. G. Andreou, "Liquid crystal polarization camera," *IEEE Trans. Rob. Autom.* **13**, 195–203 (1997).
- L. B. Wolff and A. G. Andreou, "Polarization camera sensors," *Image Vis. Comput.* **13**, 497–510 (1995).
- W. G. Egan, W. R. Johnson, and V. S. Whitehead, "Terrestrial polarization imagery obtained from the Space Shuttle: characterization and interpretation," *Appl. Opt.* **30**, 435–442 (1991).
- F. Goudail, P. Terrier, Y. Takakura, L. Bigue, F. Galland, and V. DeVlaminck, "Target detection with a liquid-crystal-based passive Stokes polarimeter," *Appl. Opt.* **43**, 274–282 (2004).
- F. Goudail and P. Réfrégier, "Statistical algorithms for target detection in coherent active polarimetric images," *J. Opt. Soc. Am. A* **18**, 3049–3060 (2001).
- F. Goudail and P. Réfrégier, "Statistical techniques for target detection in polarization diversity images," *Opt. Lett.* **26**, 644–646 (2001).
- J. S. Tyo, M. P. Rowe, E. N. Pugh, Jr., and N. Engheta, "Target detection in optically scattered media by polarization-difference imaging," *Appl. Opt.* **35**, 1855–1870 (1996).
- Y. Y. Schechner, S. G. Narasimhan, and S. K. Nayar, "Polarization-based vision through haze," *Appl. Opt.* **42**, 511–525 (2003).
- Y. Y. Schechner and N. Karpel, "Clear underwater vision," in *Proceedings of IEEE Computer Society Conference on Computer Vision and Pattern Recognition (IEEE, 2004)*, pp. 536–543.
- Y. Y. Schechner and N. Karpel, "Recovery of underwater visibility and structure by polarization analysis," *IEEE J. Ocean. Eng.* **30**, 570–587 (2005).
- Y. Y. Schechner, J. Shamir, and N. Kiryati, "Vision through semireflecting media: polarization analysis," *Opt. Lett.* **24**, 1088–1090 (1999).
- P. C. Y. Chang, J. C. Flitton, K. I. Hopcraft, E. Jakeman, D. L. Jordan, and J. G. Walker, "Improving visibility depth in passive underwater imaging by use of polarization," *Appl. Opt.* **42**, 2794–2803 (2003).
- J. G. Walker, P. C. Y. Chang, and K. I. Hopcraft, "Visibility depth improvement in active polarization imaging in scattering media," *Appl. Opt.* **39**, 4933–4941 (2000).
- H. Wang, C. Sun, Y. Wang, Y. Kiang, and C. Yang, "Determination of the depth of a scattering target in a turbid medium with polarization discrimination of transmitted signals," *Opt. Lett.* **28**, 25–27 (2003).
- S. G. Demos, W. B. Wang, and R. R. Alfano, "Imaging objects hidden in scattering media with fluorescence polarization preservation of contrast agents," *Appl. Opt.* **37**, 792–797 (1998).
- A. M. Wallace, B. Liang, E. Trucco, and J. Clark, "Improving depth acquisition using polarized light," *Int. J. Comput. Vis.* **32**, 87–109 (2001).
- R. Nothdurft and G. Yao, "Expression of target optical properties in subsurface polarization-gated imaging," *Opt. Express* **13**, 4185–4195 (2005).
- H. Chen and L. B. Wolff, "Polarization phase-based method for material classification and object recognition in computer vision," in *Proceedings of IEEE Computer Society Conference on Computer Vision and Pattern Recognition (IEEE, 1996)*, pp. 128–135.
- L. B. Wolff, "Polarization-based material classification from specular reflection," *IEEE Trans. Pattern Anal. Mach. Intell.* **12**, 1059–1071 (1990).
- Although a human visual system does not have an ability to sense polarized light, the polarization still might be perceptible in the form of Haidinger's brush.
- K. von Frisch, "Die polarisation des himmelslichtes als orientierender faktor bei den tanzen der biener," *Experimentia* **5**, 142–148 (1949).
- K. von Frisch, *Tanzsprache und Orientierung der Bienen* (Springer-Verlag, 1965).
- K. von Frisch, "Nobel lecture," The Nobel Foundation, <http://www.nobel.se/medicine/laureates/1973/frisch-lecture.pdf>.
- R. Wehner and G. D. Bernard, "Photoreceptor twist: a solution to the false colour problem," in *Proceedings of the National Academy of Sciences of the United States of America*, **90**, 4132–4135 (1993).
- R. Wehner, "Polarized-light navigation by insects," *Sci. Am.* **235**, 106–114 (1976).
- R. Wehner, "Neurobiology of polarization vision," *Trends Neurosci.* **12**, 353–359 (1989).
- R. Wehner, "Matched filters': neural models of the external world," *J. Comp. Physiol. A* **161**, 511–531 (1987).
- I. Pomozi, G. Horváth, and R. Wehner, "How the clear-sky angle of polarization pattern continues underneath clouds: full-sky measurements and implications for animal orientation," *J. Exp. Biol.* **204**, 2933–2942 (2001).
- G. Horváth, J. Gál, T. Labhart, and R. Wehner, "Does reflection polarization by plants influence colour perception in insects? Polarimetric measurements applied to a polarization-sensitive model retina of Papilio butterflies," *J. Exp. Biol.* **205**, 3281–3298 (2002).
- T. Labhart, "Polarization opponent interneurons in the insect visual system," *Nature* **331**, 435–437 (1988).
- C. W. Hawryshyn, "Polarization vision in fish," *Am. Sci.* **80**, 164–175, 1992.
- C. W. Hawryshyn, "Ultraviolet polarization vision in fishes: possible mechanisms for coding e-vector," *Philos. Trans. R. Soc. London, Ser. B* **355**, 1187–1190 (2000).
- N. Shashar and T. W. Cronin, "Polarization contrast vision in octopus," *J. Exp. Biol.* **199**, 999–1004 (1996).
- T. W. Cronin and N. Shashar, "The linearly polarized light field in clear, tropical marine waters: spatial and temporal

- variation of light intensity, degree of polarization and e -vector angle," *J. Exp. Biol.* **204**, 2461–2467 (2001).
40. N. Shashar, P. S. Rutledge, and T. W. Cronin, "Polarization vision in cuttlefish: a concealed communication channel?" *J. Exp. Biol.* **199**, 2077–2084 (1996).
 41. T. W. Cronin, N. Shashar, R. L. Caldwell, J. Marshall, A. G. Cheroske, and T.-H. Chiou, "Polarization vision and its role in biological signaling," *Integr. Comp. Biol.* **43**, 549–558 (2003).
 42. M. P. Rowe, E. N. Pugh, Jr., J. S. Tyo, and N. Engheta, "Polarization-difference imaging: a biologically inspired technique for observation through scattering media," *Opt. Lett.* **20**, 608–610 (1995).
 43. J. S. Tyo, E. N. Pugh, Jr., and N. Engheta, "Colorimetric representation for use with polarization-difference imaging of objects in scattering media," *J. Opt. Soc. Am. A* **15**, 367–374 (1998).
 44. K. M. Yemelyanov, M. A. Lo, E. N. Pugh, Jr., and N. Engheta, "Display of polarization information by coherently moving dots," *Opt. Express* **11**, 1577–1584 (2003).
 45. K. M. Yemelyanov, S.-S. Lin, W. Q. Luis, E. N. Pugh, Jr., and N. Engheta, "Bio-inspired display of polarization information using selected visual cues," in *Polarization Science and Remote Sensing*, J. A. Shaw and J. S. Tyo, eds., *Proc. SPIE* **5158**, 71–84 (2003).
 46. T. Labhart, "How polarization-sensitive interneurons perform at low degrees of polarization," *J. Exp. Biol.* **199**, 1467–1475 (1996).
 47. T. Labhart and E. P. Meyer, "Neural mechanisms in insect navigation: polarization compass and odometer," *Curr. Opin. Neurobiol.* **12**, 707–714 (2002).
 48. M. Born and E. Wolf, *Principles of Optics*, 7th ed. (Cambridge U. Press, 2002).
 49. W. B. Wang, S. G. Demos, J. Ali, and R. R. Alfano, "Imaging fluorescent objects embedded inside animal tissues using polarization-difference technique," *Optics Commun.* **142**, 161–166 (1997).
 50. C. K. Hamett and H. G. Craighead, "Liquid-crystal micropolarizer array for polarization-difference imaging," *Appl. Opt.* **41**, 1291–1296 (2002).
 51. S. P. Schilders, X. S. Gan, and M. Gu, "Resolution improvement in microscopic imaging through turbid media based on differential polarization gating," *Appl. Opt.* **37**, 4300–4303 (1998).
 52. J. S. Tyo, "Optimum linear combination strategy for an N -channel polarization-sensitive imaging or vision system," *J. Opt. Soc. Am. A* **15**, 359–366 (1998).
 53. G. Buchsbaum and A. Gottschalk, "Trichromacy, opponent colors coding and optimum color information transmission in the retina," *Proc. R. Soc. London, Ser. B* **220**, 89–113 (1983).
 54. I. T. Jolliffe, *Principal Component Analysis* (Springer-Verlag, 1986).
 55. As regular or conventional PDI in this paper, we always refer to the technique introduced in Ref. 42.
 56. N. A. Macmillan and C. D. Creelman, *Detection Theory: A User's Guide* (Cambridge U. Press, 1991).
 57. S.-S. Lin, K. M. Yemelyanov, E. N. Pugh, Jr., and N. Engheta, "Polarization enhanced visual surveillance techniques," in *Proceedings of IEEE International Conference on Networking, Sensing, and Control (IEEE, 2004)*, pp. 216–221.

Separation and contrast enhancement of overlapping cast shadow components using polarization

Shih-Schön Lin, Konstantin M. Yemelyanov

*Electrical and Systems Engineering Department, University of Pennsylvania, 220 South 33rd Street Moore 203
Philadelphia, PA 19104-6390, USA*

shschon@seas.upenn.edu, kostya@ee.upenn.edu

Edward N. Pugh, Jr.

*F. M. Kirby Center for Molecular Ophthalmology and Institute of Neurological Sciences, University of Pennsylvania
422 Curie Boulevard, Philadelphia, PA 19104-6390, USA*

pugh@mail.med.upenn.edu

Nader Engheta

*Electrical and Systems Engineering Department and Institute of Neurological Sciences, University of Pennsylvania,
Philadelphia, PA 19104, USA*

engheta@ee.upenn.edu

Abstract: Shadow is an inseparable aspect of all natural scenes. When there are multiple light sources or multiple reflections several different shadows may overlap at the same location and create complicated patterns. Shadows are a potentially good source of information about a scene if the shadow regions can be properly identified and segmented. However, shadow region identification and segmentation is a difficult task and improperly identified shadows often interfere with machine vision tasks like object recognition and tracking. We propose here a new shadow separation and contrast enhancement method based on the polarization of light. Polarization information of the scene captured by our polarization-sensitive camera is shown to separate shadows from different light sources effectively. Such shadow separation is almost impossible to realize with conventional, polarization-insensitive imaging.

©2006 Optical Society of America

OCIS Codes: (150.0150) Machine vision; (110.0100) Image processing; (260.5430) Polarization; (230.5440) Polarization-sensitive devices

References and Links

1. M. Nagao, T. Matsuyama, and Y. Ikeda, "Region extraction and shape analysis in aerial photographs," *Comput. Vis. Graph. Image Process.* **10**, 195-223 (1979).
2. R. Gershon, A. D. Jepson, and J. K. Tsotsos, "Ambient illumination and the determination of material changes," *J. Opt. Soc. Am. A* **3**, 1700-1707 (1986).
3. R. Irvin and D. McKeown, "Methods for exploiting the relationship between buildings and their shadows in aerial imagery," *IEEE Trans. on Syst. Man..Cybern.* **19**, 1564-1575 (1989).
4. J. M. Scanlan, D. M. Chabries, and R. W. Christiansen, "A Shadow Detection and Removal Algorithm for 2D Images," in *Proc. of Int. Conf. on Acoustics, Speech, and Signal Processing* (1990) pp. 2057-2060.
5. Y. Liow and T. Pavlidis, "Use of shadows for extracting buildings in aerial images," *Comput. Vis. Graph. Image Process.* **49**, 242-277 (1991).
6. C. Wang, L. Huang, and A. Rosenfeld, "Detecting clouds and cloud shadows on aerial photographs," *Pattern. Recogn. Lett.* **12**, 55-64 (1991).
7. D. Koller, K. Danilidis, and H.-H. Nagel, "Model-based object tracking in monocular image sequences of road traffic scenes," *Int. J. Comput. Vis.* **10**, 257-281 (1993).
8. C. Jiang and M. O. Ward, "Shadow segmentation and classification in a constrained environment," *CVGIP: Image Understanding* **59**, 213-225 (1994).

9. G. Funka-Lea and R. Bajcsy, "Combining color and geometry for the active visual recognition of shadows," in *Proc. Int. Conf. on Computer Vision* (1995) pp. 203-209.
10. J. Stauder, R. Melch, and J. Ostermann, "Detection of moving cast shadows for object segmentation," *IEEE Trans. Multimedia* **1**, 65-77 (1999).
11. J. A. Marchant and C. M. Onyango, "Shadow-invariant classification for scenes illuminated by daylight," *J. Opt. Soc. Am. A* **17**, 1952-1961 (2000).
12. G. Finlayson, S. Hordley, and M. S. Drew, "Removing shadows from images," in *ECCV* (2002) pp. 823-836.
13. R. Cucchiara, C. Grana, M. Piccardi, and A. Prati, "Detecting moving objects, Ghosts, and shadows in video streams," *IEEE Trans. Pattern Anal. Mach. Intell.* **25**, 1337-1342 (2003).
14. T. Gevers and H. Stokman, "Classifying color edges in video into shadow-geometry, highlight, or material transitions," *IEEE Trans. Multimedia* **5**, 237-243 (2003).
15. A. Prati, I. Mikic, M. M. Trivedi, and R. Cucchiara, "Detecting Moving Shadows: Algorithms and Evaluation," *IEEE Trans. Pattern Anal. Mach. Intell.* **25**, 918-923 (2003).
16. I. Sato, Y. Sato, and K. Ikeuchi, "Illumination from shadows," *IEEE Trans. Pattern Anal. Mach. Intell.* **25**, 290-300 (2003).
17. S. Nadimi and B. Bhanu, "Physical models for moving shadow and object detection in video," *IEEE Trans. Pattern Anal. Mach. Intell.* **26**, 1079-1087 (2004).
18. E. Salvador, A. Cavallaro, and T. Ebrahimi, "Cast shadow segmentation using invariant color features," *Comput. Vis. Image Understand.* **95**, 238-259 (2004).
19. J. M. Wang, Y. C. Chung, C. L. Chang, and S. W. Chen, "Shadow Detection and Removal for Traffic Images," in *Proc. 2004 IEEE Int. Conf. on Networking, Sensing and Control* (IEEE Syst. Man Cybern. Society, Taipei, Taiwan, 2004) pp. 649-654.
20. K. Frisch, "Die polarisation des himmelslichtes als orientierender faktor bei den tanzen der bienen," *Experientia* **5**, 142-148 (1949).
21. R. Wehner, "Polarized-light navigation by insects," *Scientific American* **235**, 106-114 (1976).
22. R. Schwind, "Zonation of the optical environment and zonation in the rhabdom structure within the eye of the backswimmer, *Notonecta glauca*," *Cell and Tissue Research* **232**, 53-63 (1983).
23. G. Horváth, "Reflection polarization patterns at flat water surfaces and their relevance for insect polarization vision," *J. Theor. Biol.* **175**, 27-37 (1995).
24. M. P. Rowe, E. N. Jr. Pugh, and N. Engheta, "Polarization-difference imaging: a biologically inspired technique for observation through scattering media," *Opt. Lett.* **20**, 608-610 (1995).
25. J. S. Tyo, M. P. Rowe, E. N. Jr. Pugh, and N. Engheta, "Target detection in optically scatter media by polarization-difference imaging," *Appl. Opt.* **35**, 1855-1870 (1996).
26. S.-S. Lin, K. M. Yemelyanov, E. N. Jr. Pugh, and N. Engheta, "Polarization Enhanced Visual Surveillance Techniques," in *Proc. IEEE Int. Conf. on Networking, Sensing and Control* (IEEE Syst. Man. Cybern. Society, Taipei, Taiwan, 2004), **1**, pp. 216-221.
27. S.-S. Lin, K. M. Yemelyanov, E. N. Jr. Pugh, and N. Engheta, "Polarization- and specular-reflection-based, non-contact latent fingerprint imaging and lifting," *J. Opt. Soc. Am. A* (to be published).
28. K. M. Yemelyanov, S.-S. Lin, E. N. Jr. Pugh, and N. Engheta, "Adaptive Algorithms for 2-channel polarization sensing under various polarization statistics with non-uniform distributions," *Appl. Opt.* (to be published).
29. J. S. Tyo, E. N. Jr. Pugh, and N. Engheta, "Colorimetric representation for use with polarization-difference imaging of objects in scattering media," *J. Opt. Soc. Am. A* **15**, 367-374 (1998).
30. K. M. Yemelyanov, M. A. Lo, E. N. Jr. Pugh, and N. Engheta, "Display of polarization information by coherently moving dots," *Opt. Express* **11**, 1577-1584 (2003).
31. W. G. Egan, "Dark-target retroreflection increase," in *Polarization: Measurement, Analysis, and Remote Sensing II*, D. H. Goldstein and D. B. Chenault, eds., *Proc. SPIE* **3754**, 218-225 (1999).
32. M. J. Duggin, "Imaging polarimetry in scene element discrimination," in *Polarization: Measurement, Analysis, and Remote Sensing II*, D. H. Goldstein and D. B. Chenault, eds., *Proc. SPIE* **3754**, 108-117 (1999).
33. D. H. Goldstein, D. B. Chenault, and J. L. Pezzaniti, "Polarimetric characterization of Spectralon," in *Polarization: Measurement, Analysis, and Remote Sensing II*, D. H. Goldstein and D. B. Chenault, eds., *Proc. SPIE* **3754**, 126-136 (1999).
34. E. Hecht, *Optics* (Addison Wesley Longman, Inc., Reading, MA, USA 1998).
35. K. M. Yemelyanov, S.-S. Lin, W. Q. Luis, E. N. Jr. Pugh, and N. Engheta, "Bio-inspired display of polarization information using selected visual cues," in *Polarization Science and Remote Sensing*, J. A. Shaw and J. S. Tyo eds. *Proc. SPIE*, **5158**, 71-84 (2003).
36. A. P. Pentland, "Finding the illuminant direction," *J. Opt. Soc. Am.* **72**, 448-455 (1982).
37. Y. Zhang and Y. Yang, "Illuminant direction determination for multiple light sources," in *Proc. CVPR* (IEEE, 2000) pp. 269-276.
38. J. Pinel and H. Nicolas, "Estimation 2d illuminant direction and shadow segmentation in natural video sequences," in *Proc. VLBV* (2001) pp. 197-202.
39. M. W. Powell, S. Sarkar, and D. Goldgof, "A simple strategy for calibrating the geometry of light sources," *IEEE Trans. Pattern Anal. Mach. Intell.* **23**, 1022-1027 (2001).

1. Introduction

Shadows are formed whenever an occlusion partially blocks the illumination of a surface or object by a light source. With the exception of the ambient light, which is assumed to be omnidirectional, light sources illuminate surfaces from only one specific direction. In addition to classification by the source direction, shadows are further classified into “self” and “cast”. A “self” shadow refers to the regions of an object not directly illuminated by a light source due to its surface orientation, whereas “cast” shadow refers to a region not illuminated by a source due to occlusion by other objects. Shadowed regions usually appear darker than the lit regions and their color properties (e.g., hue and saturation) can also appear different than the directly illuminated regions. Such differences in intensity and color create patterns and boundaries/edges that often confuse human observers or machine vision algorithms which attempt to segment scenes and identify objects using these cues. For this reason many techniques have been developed to identify, segment, and remove shadows from an image or a video sequence[1-19]. However, all previously published methods use only two aspects of light, its intensity and/or spectral (“color”) distribution as information in shadow segmentation, though; in some cases these are combined with temporal and geometric information available. It appears that a third fundamental property of light, its polarization, has not heretofore been used for the purpose of shadow segmentation. Furthermore, most existing shadow segmentation algorithms assume a relatively simple shadow model: an area of a scene is classified either as shadow or non-shadow. In fact it is possible for a specific region of a scene to be both shadow for one source and illuminated simultaneously by another source or sources, as explained below, and polarization information can assist in “parsing” such complications in scene segmentation.

Polarization is an intrinsic property of light. Light from the dominant natural source, the sun, is not polarized but light scattered from small particles in the sky and most light reflected or scattered from object surfaces is partially polarized. The unaided human eye and most machine vision cameras are “blind” to polarization, but some animal species can detect and utilize polarization information and use it for a variety of purposes, including navigation and object recognition [20-23]. Inspired by biological polarization vision, our group has developed polarization sensitive cameras and processing methods for the detection of targets in scattering media, detecting latent fingerprints and enhancing surveillance [24-28]. We have also developed methods for displaying polarization information effectively to human observers [29,30]. It has been reported that polarization increase in dark surface area [31], and that polarization can be used to enhance details in shadow [32]. It has also been reported that polarization increases with increasing incident light angle [33]. In this investigation we show that complex overlapping cast shadows that are almost impossible to distinguish in images generated with only intensity and color information can be readily segmented from each other in images generated from the polarization parameters of a scene.

2. Polarization and Shadow

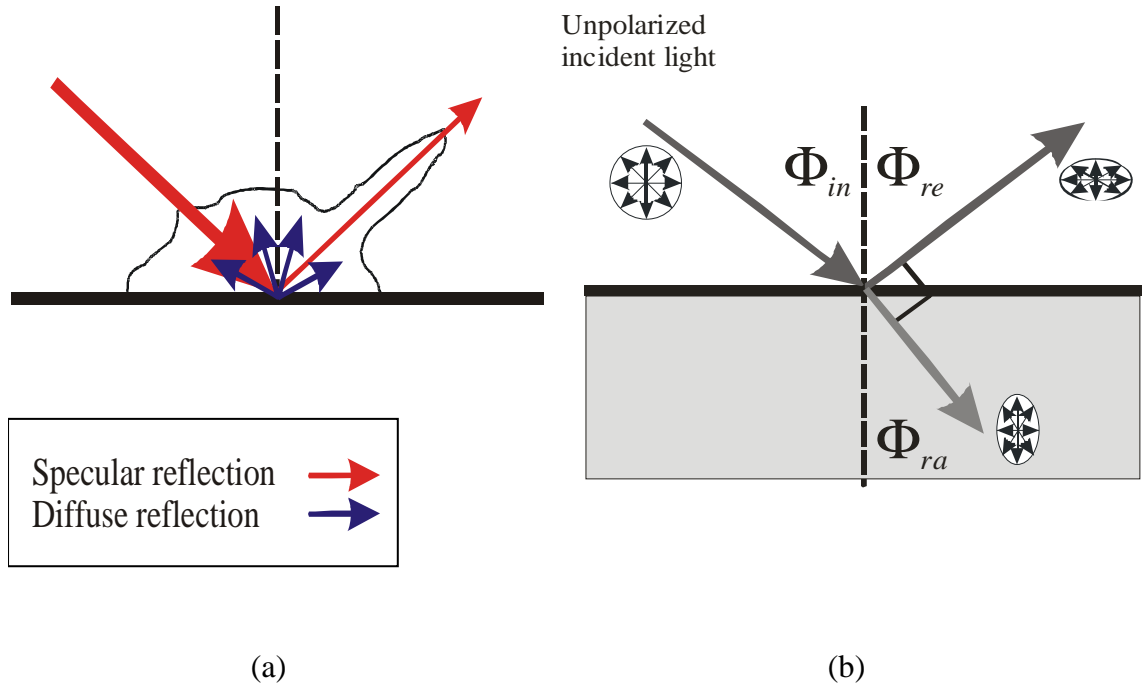


Fig. 1. (a) General macroscopic reflection model (b) Polarization of light resulting from specular reflection from a dielectric surface.

According to the generally accepted macroscopic description of the interaction of light with a surface, reflected light can be subdivided into specular and diffuse components [Fig. 1(a)]. The ratio of energy carried by the diffuse and specular components depends on the angle of incidence and the material properties of the surface. The diffusely reflected components often undergo multiple random reflections microscopically, so statistically they tend to be unpolarized. In contrast, the specularly reflected component is usually at least partially polarized, with the polarization direction (dominant axis of E-field oscillation) parallel to the local tangent plane of the surface [Fig. 1(b)]. These physical phenomena can be formalized through appropriate application of Fresnel's analysis and Eq. [34].

In addition to the scattering by surfaces, another important natural source of polarization is the scattering of light by the atmosphere of the earth. The polarization of sun light by the air particles can be explained by the theory of *Rayleigh scattering* [34], which describes the particles as electric dipoles: because oscillating dipoles do not radiate in the direction of oscillation, a polarization-sensitive observer will see the dome of the sky to exhibit polarization pattern that depends on the location of the sun. Since pioneering investigations of von Frisch it has been well established that many insects can avail themselves of this polarization for navigation [20-23]. Such polarization has consequences for the segmentation of shadows: thus, as we will show below, an area that is inside a shadow cast by direct sunlight, but which is lit by the polarized ambient sky light will show a distinctive polarization, whereas an area that is inside both the shadow cast by sunlight and the shadow cast by skylight will show no polarization at all.

Because most imaging devices integrate light energy over a time epoch that is long relative to the oscillation period (fs), phase information is not recorded. With the phase information lost, when a linear polarization analyzer is placed in front of the camera, the measured intensity I at a specific image location or pixel, as a function of the angle of orientation φ of the polarization analyzer is given by

$$I(\varphi) = I_U + I_A \cos[2(\theta - \varphi)] = I_U \{1 + p \cos[2(\theta - \varphi)]\}, \quad (1)$$

where θ is the orientation angle of the major axis of the polarization ellipse, I_U is 50% of the total intensity at each pixel, and $p \equiv I_A / I_U$ defines the degree of linear polarization at the pixel. The reference axis for the two angles φ and θ can be arbitrarily chosen, and complete information about the polarization state of the light can be obtained by capturing images with the polarizer oriented at three different angles, for example $\varphi = 0, 45$ and 90 degrees [26,35]. From these three images, one can recover I_U , I_A , and θ for each pixel of the image using the following expressions:

$$\begin{aligned} I_U &= (I_0 + I_{90})/2 \\ I_A &= \sqrt{(I_{45} - I_U)^2 + (I_{90} - I_U)^2} \\ \theta &= \arctan[(I_{45} - I_U)/(I_{90} - I_U)]/2. \end{aligned} \quad (2)$$

Here indices 0, 45, and 90 indicate the orientation of the polarizer in degrees when each specific image was taken. Because θ and $\theta + \pi$ are indistinguishable for phase-blind sensors, the meaningful range of θ is restricted to π , and θ ranges from 0 to π . In the work presented here we sample three angles (0, 45 and 90) by manually or mechanically rotating a single linear polarizer mounted in front of an intensity integrating camera. The camera used in our experiments is a calibrated Olympus E-10 digital camera with 4 Mega pixels and 10 bit pixel depth (we use the RAW mode).

3. Experiments

The first example is an outdoor scene of a walkway in front of a building with all-glass walls (Fig. 2 to Fig. 4, the glass-walled building is visible in Fig. 4). To help reader grasp the relationship between pictures in Fig. 2 to Fig. 4, we overlay a yellow circle over a sewer drainage cover that is visible in all pictures but Fig. 4 Left to call attention to readers that this is the exact same object in all the pictures. Then a green square is overlaid on the same glass door that is visible in both Fig. 4 Left and Fig. 4 Right. The sun illuminated the scene from the right hand side of the picture: shadows cast by trees are seen along the walkway, most clearly in the upper portion of the image. Most existing shadow handling algorithms would simply segment the dark areas as shadows, reducing or eliminating the contrast in brightness caused by the shadow. However there is a more complicated overlapping shadow pattern hidden inside the scene that is not detectable from analysis of the intensity distribution.



Fig. 2. Left: “Intensity-only” image of an outdoor scene with light and shadow. Right: “Degree-of-polarization” image of the same scene; this image plots the quantity $p = I_A/I_U$ [see Eq. (2)], extracted for each image pixel. Hidden patterns of shadows within shadows are clearly visible in high contrast. The glass-walled building is shown in Fig. 4. The yellow circle points out the same sewage drain cover that is visible in all related pictures up to Fig. 4 except Fig. 4 Left to help orientation.

In this scene the glass-wall building to the left rear side of the scene reflected sunlight from its glass panels, but not from the thinner frames around each piece of glass. The reflected light was partially polarized, and the reflection pattern cast on the scene overlapped with the shadow pattern cast by the direct sunlight. The light reflected by the glass was weaker than the direct sunlight, and the pattern it creates is essentially invisible in the “intensity-only” image at left. However, when our polarization-sensitive camera was used to extract the “degree of polarization” image, the hidden pattern of overlapping shadow was revealed (Fig. 2, right panel). The area that was lit neither by direct sunlight, nor by the reflected light from the glass, is both dark and unpolarized, and thus appears dark in both images. These are the cast pattern of the glass frames of the glass-wall building to the left of the picture. The areas that were not lit by direct sunlight – and thus appear as shadows in the intensity-only image – but which were illuminated by the partially polarized reflected light from the glass-wall building, exhibit strong polarization. The degree-of-polarization image normalizes the polarization signal with respect to the total intensity [Eq. (2)], so these areas show up as a bright pattern in the degree-of polarization-image (Fig. 2, right). To establish that this pattern is unique to the polarization analysis, and not hidden in the intensity-only image due to low contrast in the shadow area, we performed linear contrast enhancement, followed by gamma correction of 0.5 to both images of Fig. 2: from the results (Fig. 3) it is clear that the shadow patterns are only revealed in the degree-of-polarization image. To further document the nature of the sunlight and glass wall sources to the shadows revealed by polarization analysis we provide images of the glass-wall and frames of the building (Fig. 4, left), and of the walkway when the bright direct sunlight is blocked (Fig. 4, right). Note that pictures in Fig. 4 are taken with the camera at about the same position and general view direction as when the pictures in Fig. 2 and Fig. 3 were taken. The only difference is that in Fig. 4 the camera zooms out and points more upward in order to put the tall glass-walled building into view. In sum, the patterns revealed in the degree-of-polarization image are indeed caused by shadows created by polarized light reflected from the glass source.



Fig. 3. Images in Fig. 2 are contrast-enhanced by linear intensity range stretch followed by gamma correction of 0.5 to show the details in the dark area. Left: intensity image. Right: degree of polarization image. It is clear that the pattern revealed in the polarization image is not present in the intensity image even after contrast enhancement. The yellow circle points out the same sewage drain cover that is visible in all related pictures up to Fig. 4 except Fig. 4 Left to help orientation.

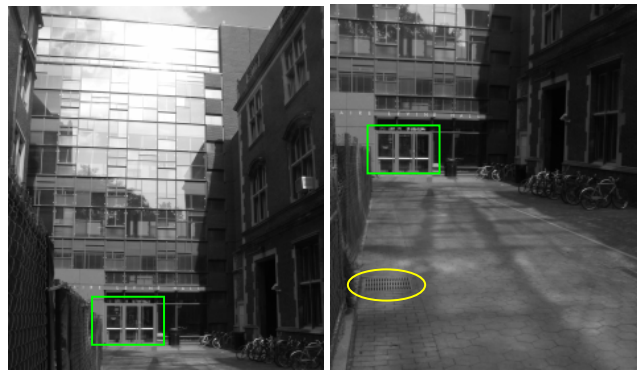


Fig. 4. (Pictures shown in this figure are all regular intensity images with no polarization information) Left: the glass-wall building showing big glass rectangles and frames. Right: A picture of the same walk way as in Fig. 2 and Fig. 3 taken another day when the direct sun light is blocked due to nearby construction scaffolding. The shadow pattern cast on the walk way by the glass-wall and frames is visible. The yellow circle in the Right picture points out the same sewer drain cover as seen in Fig. 2 and Fig. 3. The left and right pictures in this figure can be related by the same glass door bracketed by the overlaid green rectangle. Note that pictures in Fig. 4 are taken with the camera at about the same position and general view direction as when taking pictures in Fig. 2 and Fig. 3. The only difference is that in Fig. 4 the camera zooms out and points more upward in order to put the tall glass-walled building into view.

We performed a controlled laboratory experiment to further confirm the results obtained outdoors. The setup comprises a 150W incandescent light source illuminating a scene from the direction opposite the camera, and a 15W fluorescent light illuminating the same scene from the direction corresponding to right hand side of the picture (Fig. 5).

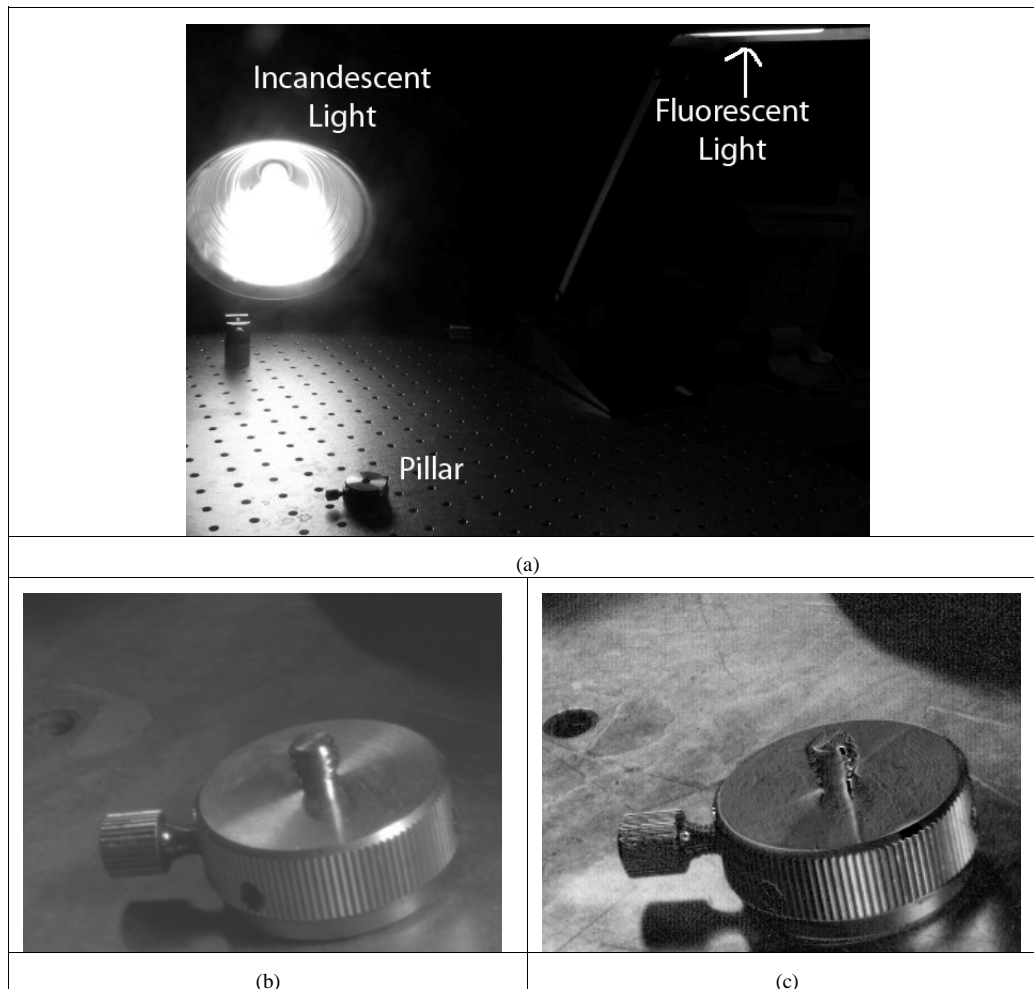


Fig. 5. Controlled lab experiment of complex overlapping shadow: (a) Overview of the experiment setup. A metal pillar on a optical table illuminated by a strong incandescent light from the side opposite to the camera, while another much weaker fluorescent light illuminating from the right hand side of the picture. The polarization of the observed reflection from the side illuminating fluorescent light is weaker because they are all diffusely scattered reflection, as opposed to the mostly Fresnel reflection [34] coming from the incandescent light shining directly opposing the view of the camera. (b) Intensity-only image. (c) Degree-of-polarization image.

In the intensity-only image only the shadow of the knob cast by the dominant (incandescent) light source is visible. However, in the degree-of-polarization image, additional information is visible and separated clearly in high contrast. Specifically, a “shadow” cast by the much weaker fluorescent light from the right hand side is revealed as a bright area to the left of the metal pillar. The reason that this region appears bright in the degree-of-polarization image is due to the viewing geometry: the strong light reflected from the table is highly polarized, whereas the light reflected to the camera from the side source is only weakly polarized, and so where there is a shadow cast by the weaker source, the degree of polarization is less diluted by the weak unpolarized source and higher degree of polarization is detected. In addition, the area that is not illuminated by either source is very dark in the intensity-only image and is least polarized and seen as the darkest area in the degree-of-polarization image. Similarly, the polarization of the image regions corresponding to areas lit by both strong and weak light

sources is lessened by the unpolarized light reflected to the camera from the weak source at the right hand side of the picture. Segmentation algorithms operating on the degree-of-polarization image can readily extract the distinctive “shadow” cast by the weak source. A sample analysis (Fig. 6 left) shows a segmentation obtained by a growing algorithm that starts with 2×2 regions. The side shadow area is cleanly separated from the image when 21 or more regions are segmented (Fig. 6, right).

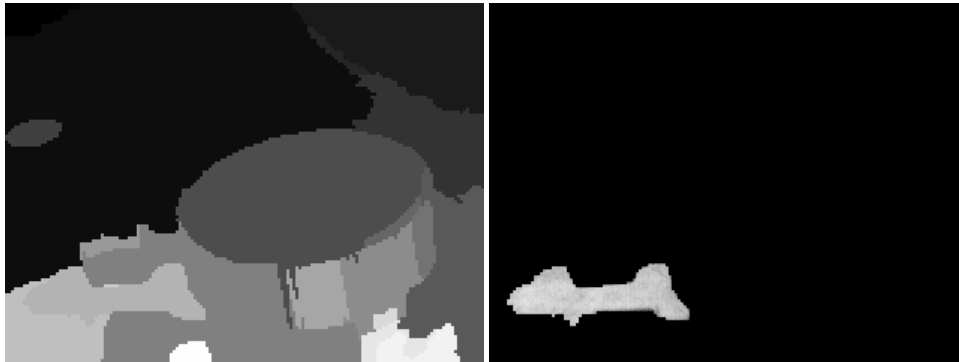


Fig. 6. Left: Segmentation results from region-growing analysis (starting with the entire image divided into 2×2 regions and with adjacent similar regions merging in each iteration) of Fig. 5 (c) into 21 regions. Right: Hidden shadow area extracted from Fig. 5 (c). Note that this pattern is only a portion of a larger shadow of the metal pillar cast by the source at right, and that this larger shadow is partially obscured by both the small knob and the shadow of the small knob cast by the source opposing the camera.

4. Discussion

The processing of shadows in images presents many difficulties for scene segmentation, and all existing methods for analyzing shadows based on intensity-only information have limitations. Many methods are designed for specific applications like aerial photography or traffic monitoring [1-19], so that the lighting condition is simplified or known *a priori*. Many applications using extant methods require a specific geometry of the illumination and camera, and/or very precise calibrations of the pixel sensitivity of the camera. The use of polarization in shadow analysis and segmentation appears to be robust and certainly provides new and useful information that may facilitate segmentation and reveal new features of the scene and the sources that illuminate it. The polarization based shadow segmentation method suggested here does have its own limitations. While this method is not strictly tied to a specific scene geometry, the method does not work when the scene signals happens to be unpolarized everywhere, a rare but possible scenario. Nonetheless, because signals extracted with Eq. (2) are strongest when there is specular reflection, the use of the degree-of-polarization image for segmentation can be expected to give the best results when the source is opposite and directed toward the imaging system. A valuable feature of the method presented here is that it can readily reveal the presence of multiple sources of widely varying “strength”. As methods have already been developed for estimating the illumination directions of multiple light sources from information in the image [36-39], it can be anticipated that combining polarization analysis with these methods will produce valuable new tools for determining the direction of illumination sources. Investigations along these lines are underway. This use of polarization information in shadow detection, separation and contrast enhancement will also be further enhanced when it is combined with other well known cues like intensity, color, and geometry to achieve more accurate shadow segmentation and give more detailed information on the origin of distinct shadow components. While the present investigation has based its shadow-segmentation solely on degree-of-polarization information, the additional cue provided by the orientation of the local polarization ellipse [θ in Eq. (1)] can also be used for image segmentation (in much the manner in which color is used), and it can also be

anticipated that this will further contribute to the method. Moreover, as expected from the independence of polarization from the other physical attributes of light and demonstrated by our experiments, information extracted by polarization about shadows is unique and in general cannot be extracted from other cues alone.

5. Conclusion

We have presented a novel method of shadow segmentation based on the local degree of polarization in images captured by a polarization-sensitive imaging system. This analysis reveals that the polarization of light conveys distinct and valuable information about a scene that can be extracted at modest cost. Polarization have been used in many other vision tasks such as removing glare and target detection, but to the best of our knowledge has not previously been used to aid the segmentation of complex shadows in a scene. Polarization information enables our system to extract information about the complexities of multiple light sources and the overlapping shadows they create. Such shadows are very difficult even to detect in intensity-only images, and their extraction with polarization analysis provides a new means of identifying the direction and nature of light sources illuminating a scene.

Acknowledgments

This work is supported in part by the U.S. Air Force Office of Scientific Research (AFOSR), through grants F49620-02-1-0140, FA9550-05-1-0052, and the DURIP grant F49620-02-1-0241. Correspondence should be addressed to Shih-Schön Lin, TEL: +1-215-898-2102; e-mail: shschon@seas.upenn.edu or Nader Engheta, TEL: +1-215-898-9777; fax; 215-573-2068; e-mail; engheta@ee.upenn.edu.

Polarization-based and specular-reflection-based noncontact latent fingerprint imaging and lifting

Shih-Schön Lin and Konstantin M. Yemelyanov

Electrical and Systems Engineering Department, University of Pennsylvania, 220 South 33rd Street, Moore 203, Philadelphia, Pennsylvania 19104-6390

Edward N. Pugh, Jr.

F. M. Kirby Center for Molecular Ophthalmology and Institute of Neurological Sciences, University of Pennsylvania, 422 Curie Boulevard, Philadelphia, Pennsylvania 19104-6390

Nader Engheta

Electrical and Systems Engineering Department and Institute of Neurological Sciences, University of Pennsylvania, Philadelphia, Pennsylvania 19104

Received December 22, 2005; accepted February 25, 2006; posted April 6, 2006 (Doc. ID 66822)

In forensic science the finger marks left unintentionally by people at a crime scene are referred to as latent fingerprints. Most existing techniques to detect and lift latent fingerprints require application of a certain material directly onto the exhibit. The chemical and physical processing applied to the fingerprint potentially degrades or prevents further forensic testing on the same evidence sample. Many existing methods also have deleterious side effects. We introduce a method to detect and extract latent fingerprint images without applying any powder or chemicals on the object. Our method is based on the optical phenomena of polarization and specular reflection together with the physiology of fingerprint formation. The recovered image quality is comparable to existing methods. In some cases, such as the sticky side of tape, our method shows unique advantages. © 2006 Optical Society of America

OCIS codes: 150.0150, 110.0110, 100.0100, 260.5430.

1. INTRODUCTION

Fingerprinting is one of the most widely used biometric methods for identifying and authenticating individual persons. The modern science of fingerprinting started in the second half of the 19th century. For an interesting historical review, see Refs. 1–3. There are two types of fingerprint data, distinguished by their formation processes. In forensic science, finger marks left unintentionally at a crime scene are referred to as latent fingerprints. Fingerprints acquired directly from human fingers using ink or scanners in controlled environments are referred to as exemplar fingerprints.^{1–4} Although both types of fingerprints are related to some extent, the recovery of latent and exemplar fingerprints poses very different technical challenges. There have been considerably more successful optical methods for exemplar fingerprints than for latent fingerprints, and sometimes the classification can be confusing. For example, there exist methods that use laser and polarization for extracting fingerprint images directly from live human fingers⁵; such methods are for acquiring exemplar fingerprints. The purpose and the detailed physical background of that system are different from those involved in the application of laser or polarization to latent fingerprints. Another example is a device that claims that it “optically reads a latent fingerprint.”⁶ However, the main function of the particular device is to read

directly from a human finger (and simultaneously compare with a known fingerprint pattern), and such a device should be classified as an exemplar fingerprint reader. Recovery of latent fingerprints is much more difficult than the recovery of exemplar fingerprints because the physical and chemical composition of latent fingerprints and the surfaces on which they are found vary greatly and can often undergo unknown degradation before being examined. In this paper we present a new method for the detection and recovery of latent fingerprints.

Latent fingerprints differ from exemplar fingerprints in that they are very difficult to detect with unaided human vision under most ordinary viewing conditions (hence their name); they are usually also of lower quality than exemplar fingerprints, although high-quality fingerprint marks can at times be found at a crime scene. To be precise, nonexemplar fingerprints that can be easily seen by a human observer should be called patent fingerprints.^{1–4} In practice, however, the term latent fingerprints is often used to refer to all fingerprints that are not exemplar. It is really latent fingerprints that are more common at a crime scene and require greater efforts to render visible. Most techniques employed for this purpose utilize a chemical or physical process that applies some kind of material directly to the surface suspected to bear fingerprints.^{1–4,7–9} Once the contrast of the fingerprint

mark is sufficiently enhanced by such treatments, the mark is either photographed or lifted to be permanently archived as evidence. The term lifting the fingerprint originates from the oldest, but still widely used, fingerprint detection method—powdering—in which the powders applied adhere to the fingerprint material, and then are physically lifted out of the original crime scene object by sticky tape.

Since applying chemicals or powders onto a surface on which fingerprints reside changes the chemical and/or physical composition of the surface, the use of such invasive methods can potentially interfere with subsequent forensic testing of different types, and can sometimes inflict deleterious side effects on the surface or the operator. Therefore, in the past 30 years several techniques that can recover latent fingerprints without the need to apply foreign material directly onto the fingerprints have been developed. Many of these methods use specialized light sources (e.g., laser, UV), filters, and detectors.^{1–4,7–12} They are successful in some cases. However, like all other existing techniques, they do not work in all possible cases and are known to fail completely with certain types of latent fingerprints or object surfaces. As a result, chemical enhancers are often reintroduced to aid in the detection of latent fingerprints.^{1–3,9,12–19} Further studies show that techniques using special light sources and filters work much better and in more cases when combined with the application of certain chemicals on the fingerprint sample first.^{1,9,12–19} However, the application of chemicals directly onto the fingerprints effectively negates the advantages of noncontact methods, and the composite methods revert back into invasive.

It has been known by experienced law enforcement officers that by varying the angle of a flashlight shining onto a surface suspected to bear latent fingerprints, one can potentially locate latent fingerprints that are otherwise difficult to see.⁷ However, to lift the latent fingerprints in a form that can be documented and presented as evidence in a court trial, some invasive enhancement treatments are usually considered necessary. Pfister^{9,20} devised an optical method that uses a semitransparent mirror that can project light onto a surface at a right angle, while at the same time allowing a camera or observer to view the surface at a right angle. A smooth surface is expected to appear bright due to strong specular reflection, while a fingerprint mark would appear darker due to much less specular reflection. Margot and Lennard^{9,21} reported that such a method works better when the sample is pretreated with cyanoacrylate. The use of only a right angle in Pfister's method sacrificed quite a bit of flexibility, and polarization-based techniques cannot be applied to further improve the contrast because the specular reflection observed at a right angle from the surface is not preferentially polarized. It is widely known that specularly reflected light from dielectrics would be partially polarized at a certain range of viewing angles. However, to the best of our knowledge, no known application of polarization has been reported for latent fingerprints, with the exception of using a polarizing filter to remove glare when taking pictures, which is considered a standard photographic technique. Menzel²² briefly mentioned the possibility of using optical polarization to en-

hance visibility of latent fingerprints left on glass, but it appears that no further development took place.

We propose here a new method that allows the detection and lifting of latent fingerprints into clearly identifiable digital images without the application of chemical treatments or, indeed, without any physical contact with the surface and fingerprint material. Rather than employing extraneous material, our method takes advantage of the optical properties. In particular we exploit those properties related to specular reflection and polarization of the latent fingerprint, which usually consists of tiny ridges of skin residue material including sweat (salty water), grease, and lipid,^{2,3,23} all of which are rather transparent dielectric materials, making them difficult to detect under most viewing conditions. Our method is also applicable to latent fingerprints left on a smooth but pliable dielectric surface. The recovered fingerprint images have comparable or better quality than those obtained by conventional methods.

2. NONCONTACT OPTICAL LATENT FINGERPRINT ENHANCEMENT AND LIFTING: CORE TECHNIQUE OUTLINE AND EXPERIMENTAL SETUP

We start with the principal physical and physiological basis of our noncontact optical latent fingerprint enhancement and lifting in this section. The actual formulas used in our computation will follow later. The physics underlying the method is illustrated in Fig. 1. When a finger touches the object surface, a dielectric residue mark bearing the fingerprint pattern is imprinted on it. The residue on the surface induces differences in optical polarization or reflection or both between the clean part of the surface and that bearing the print. The optical information is captured and enhanced by our unique optical setup and stored as digital images. Further digital processing of the captured images enables us to develop or lift the latent fingerprint pattern without applying any powder or other chemicals to the object. Our optical setup is based on the well-known Fresnel reflection theory for orthogonal polarizations and the theories for macroscopic surface reflectance developed for computer vision and graphics. As an aside, it is interesting to note that biologists and zoologists have found that certain animal species have visual systems that sense and utilize (in or near) visible light's polarization in the natural environment, e.g., backswimmer *Notonecta glauca* can detect the polarization of light reflected from smooth water surfaces and use it to land and plunge safely on the water surface.^{24,25} Indeed, our original step to design our optical setup for latent fingerprint detection was inspired from this ability of *Notonecta glauca* in detecting the surface of the water.

In Fig. 1(c), we illustrate a cross-section view of the fingerprint on a surface. The ridge area corresponds to a small amount of residue on the surface, while the furrow area does not. All existing enhancement methods take advantage of this situation by applying materials that selectively attach to or interact with only the residue area and produce a colored or fluorescent pattern of the residue area. Our noncontact method exploits this situation in a different way [Fig. 1(d)], with a common household light

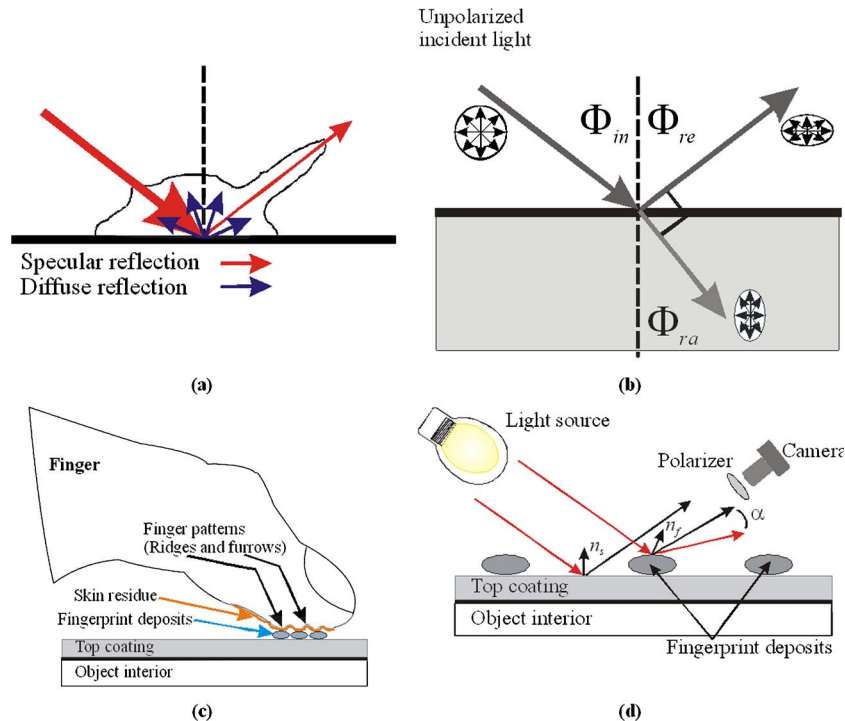


Fig. 1. (Color online) Schematic of the physical principles concerning noncontact latent fingerprint enhancement and lifting. (a) Macroscopic reflection from a surface consists of two distinct kinds, i.e., specular and diffuse. For specular reflection the angles of incidence and reflection are equal, while for the diffuse case the reflected intensity may approximately have an effectively uniform distribution over all directions in a hemisphere. Most surfaces exhibit both types of reflection, but one type may be stronger than the other. (b) Partial polarization of specularly reflected light from a semitransparent dielectric surface. It is known that the light reflected from the smooth surface is partially polarized with the polarization being perpendicular to the plane of reflection. (c) Live human skin is kept soft and pliable by the constant oily secretion of hypodermic glands. The ridge area of the skin pattern tends to leave a dielectric residue on a surface touched by a finger. (d) The residue left in (c) forms the latent fingerprint. Using a method that generates a sufficient contrast difference between the latent fingerprint and the rest of the surface in the camera image, a successful detection and extraction can be achieved without applying physical or chemical treatments to the surface. Note that the camera position in (d) is oriented in a such a way that it captures the specular component of reflected light from the clean surface only while the specular reflection component of the residue is not captured. Additionally, when a finger touches a pliable dielectric surface it could cause a plastic print on the surface. In this case the difference in the surface normal caused by the plastic print ridges will serve the same purpose of creating contrast in intensity and polarization under proper lighting.

source (incandescent or fluorescent, does not really matter here), a camera, and the surface being inspected and arranged in such a way that the geometry conforms approximately to the law of (specular) reflection. Thus, the incident angle of light from the source approximately equals the viewing (reflection) angle of the camera, so that the camera will capture the light reflected specularly from the nonresidue area, and also only the light reflected diffusely from the residue-laden area. The reason for this arrangement is that the residue stain area is likely to have different surface normal directions and indices of refraction as compared with the uniform or smoothly varying surface normal direction of the unstained surface area. The localized nature of specular reflection energy distribution makes it sensitive to changes in the direction of the surface normal caused by the presence of fingerprint residue on the surface. Since the specular reflection component is, in general, much stronger than the diffuse reflection component²⁶ [see Fig. 1(a)], one potentially finds an enhanced contrast between the residue-laden ridge mark and the clean surface furrow negative mark. Another often-encountered case is a plastic fingerprint left on a pliable dielectric surface. There may or may not be biological residue left on the surface, but the ridge and

furrow patterns formed by the pliable dielectric material itself create differences in surface normal compared with the undisturbed surface area and will serve the same purpose.

Note that Fig. 1(d) is not drawn to scale. The microstructure of the fingerprint ridges has been magnified hundreds of times for illustration purposes and the sizes of the light source and the camera and the distances from each of them to the sample surface have been greatly scaled down to fit in the limited figure space. In Fig. 1, if one tries to draw straight lines linking a point on the light source to a ridge and another straight line from the same point on the light source to a valley point in Fig. 1(d), it would appear that the two lines are far from parallel. The fact is that it does not make any sense to draw these two lines in Fig. 1(d) where sizes and distances were not drawn to scale. A typical fingerprint is quite small, ~ 1 in. (25.4 mm) by 0.3–0.5 in. (7.6–12.7 mm) while a typical light bulb is ~ 3 in. (76 mm) in diameter and needs to be placed at least 7 in. (177.8 mm) from the sample surface to avoid blocking the field of view of the observing camera or overheating the surface. In Fig. 2 we show a drawing that is more to scale. The area occupied by the print mark of one finger extends to only the small area around the

point P in Fig. 2. There are typically more than 50 ridges and valley periodic patterns within this small area. The distance from a ridge point to its immediate adjacent valley point is typically only ~ 0.5 mm. Note that we only need to make sure that the contrast between one valley and its immediate adjacent ridge area is high enough for detection. So the only thing we need to check is whether light coming from the same point source would have practically the same incident direction for a point on a fingerprint ridge area compared with a point on the valley area immediately adjacent to the ridge. This is indeed the case. For Fig. 2, if we have typical setup dimensions of $OP = 177.8$ mm and $OL = 177.8$ mm, with an incident angle of 45 deg, then the incident angles of light from the same source point L to the immediate adjacent valley points (suppose that P is a ridge point) are $\arctan[(177.8 + 0.5)/177.8] = 45.08$ deg and $\arctan[(177.8 - 0.5)/177.8] = 44.92$ deg, respectively. They are indeed practically parallel. All realistic light sources are extended light sources that can be modeled as a group of a countless number of point sources. The illumination effects can be found by integrating the contribution from every light-emitting point source comprising the whole light source. Since we are using an ordinary incoherent light source, the contributions to the irradiance from each point source simply add up and we do not need to consider interference here. Figures 2(a) and 2(b) also describe how the directional reflecting nature of specular reflection and the directional light acceptance of the observing camera work together to create the desired contrast between adjacent fingerprint ridge and valley areas using a simple noncollimated extended light source like a light bulb with a diffuser plate. Because a camera placed at point C records only light energy reflected from P along the direction PC, only light incident along the direction LP would have almost all its specular reflection component being recorded by the camera at point C for the specular irradiance (I_S) of point P. The diffuse reflection components have energy almost evenly spread in all directions and only those small fractions of energy directed toward the direction LP would be recorded by the camera at C for the diffuse reflection irradiance (I_D) for point P. In Fig. 2(a), if we set up collimated light beams, then every incident light beam would contribute about the same ratio of specular irradiance and diffuse reflection irradiance. In Fig. 2(b) we show what happens when a noncollimated extended light source is used. First, while there can be many incident light rays parallel to the direction LP, they do not contribute to the specular reflection irradiance of point P in the observed image because the camera at point C does not see them reflecting from the point P, except only the ray LP. Any light ray incident from a direction different from the direction LP will have its specular reflection component reflected to directions other than the direction PC, but the camera only collects irradiance energy emitted along the direction PC for the point P, so this has no effect on our images. The light rays coming from different angles do contribute to the diffuse reflection component because diffuse reflection energy is almost evenly distributed along all directions regardless of the incident direction. Since the recorded irradiance is the algebraic sum of all collected irradiance, the observed specular reflection

irradiance would come from only the incident light along the direction of LP. Thus the specular reflection signal I_S remains the same for both Figs. 2(a) and 2(b). The diffuse reflection signal I_D would be stronger in Fig. 2(b) than in 2(a). Thus the effect of using a noncollimated extended light source is just some decrease in contrast between I_S and I_D . Note that, although I_D receives contribution from more light source points than I_S , each contribution is rather small compared with the strength of the specular reflection. Thus in many cases we can still observe the fingerprint pattern easily. Note also that when the distance S is large compared with the dimension of the light source, then the incident angle differences α will be negligible. In other words, an ordinary household light source like a lamp can nicely approximate an ideal point light source as long as the distance S is several times that of the dimension of the light source.

Another point we want to mention here is the use of a diffuser in front of the light bulb in our experiment. Specular reflection is the same type of reflection we see from a mirror, which means that by observing the specular reflection we will be seeing the mirror image of our light source. A bare light bulb without a diffuser will project its own image, e.g., the filament and its shade,...etc., on top of the fingerprint sample. This would add clutter to the fingerprint image we want to recover. Adding a diffuser in front of a light bulb would diffuse the mirror image pattern of the light source so that we get a cleaner fingerprint image. The image of a lighted diffuser plate is almost featureless, so its image projected on the surface would not add its own patterns over potential fingerprint patterns on the surface being illuminated. One should not confuse this diffuser with the term diffuse re-

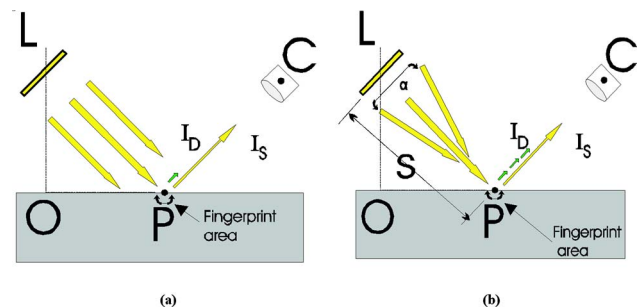


Fig. 2. (Color online) Drawings depicting the same setup as in Fig. 1(d) but with relative distances and object sizes drawn to scale to explain the effects of a real light source compared with an idealized collimated light source. In both (a) and (b), L is the position of the light source; O is the orthogonal projection on the surface for L; P is a ridge or valley point around the center of the fingerprint pattern; C is the camera view point. I_D is the irradiance of the point P from diffuse reflection and recorded by the camera at C. It is typically weak and is also represented here as the small arrow(s) along the direction PC. I_S is the irradiance of the point P from specular reflection and recorded by the camera at C. It is typically much stronger compared with irradiance from diffuse reflection, and is depicted here by the large arrow along the direction PC. (a) The simple condition when the light source is effectively collimated along the direction of LP. (b) The situation for when a noncollimated extended light source is used. The I_S remains the same as in (a) but I_D is stronger due to the contribution from more point sources. The end result is decreased contrast between I_S and I_D . However, since only I_S contains a polarized component, the polarization-based method is equally effective in both conditions.

flection we mentioned elsewhere in this paper. Diffuse reflection and specular reflection are two different types of reflection from a surface (although in reality they coexist in virtually every surface reflection). A surface reflects any incident light partially in the form of diffuse reflection and partially in the form of specular reflection, regardless of how and where the incident light comes from. In other words, any incident light, whether it is directly from a light bulb or has undergone scattering by a diffuser, will be reflected by the surface we are examining partially via specular reflection and partially via diffuse reflection. The diffuser we put in front of the light bulb has nothing to do with the surface on which we look for fingerprints. The diffuser does not even have anything to do with reflection on the fingerprint-bearing surface that is the main topic of our detection method. The function it performs in our setup is scattering and transmitting the light before it reaches the surface-bearing fingerprint.

The trade-off of using a diffuser is a stronger observed diffuse reflection for every point, and thus reduced fingerprint contrast in the specular-reflection-only-based method. In some cases the contrast between the diffuse reflection component and the specular reflection effect becomes too low to be useful. It is also possible that the object itself may have a complicated high-contrast pattern under the top coating of the surface [see Figs. 1(c) and 1(d)] that interferes with the fingerprint pattern even after the enhancement. This problem has been recognized by many practitioners.^{27,28} Discrete Fourier-transform analysis has been shown to be able to remove regular patterns that vary periodically, but cannot deal with a general background that is not periodic. In cases where the intensity difference caused by specular reflection alone is not enough to detect fingerprints, we use polarization imaging to accomplish the fingerprint detection. An additional characteristic of specular reflection is that it tends to be partially polarized in a plane perpendicular to the plane of reflection [see Fig. 1(b)]. One or more polarization analyzers collecting polarization components at different angles can provide complete information about the polarization state of the reflected light. On the basis of the polarization information, we can further extract only the specular component of this reflection and get a much cleaner fingerprint image because for the most part the light coming from the pattern beneath the top coating of the object surface is due mostly to unpolarized, diffuse reflection. We have also found that in some cases some of the polarization images simply show higher contrast between the fingerprint and its background than the fingerprint images recovered using specular reflection alone.

The general expression for the observed intensity of partially polarized light I as a function of the angle φ of orientation of a polarization analyzer can be written as follows^{29,30}:

$$I(\varphi) = I_U + I_A \cos[2(\theta - \varphi)] = I_U \{1 + p \cos[2(\theta - \varphi)]\}, \quad (1)$$

where θ is the orientation angle of the major axis of the polarization ellipse, I_U is half of the total pixel intensity, and $p = I_A/I_U$ is the degree of linear polarization at a given pixel in a digitized image. The reference axis for φ and θ can be arbitrarily chosen. Since there are more than one unknown parameters, putting one polarizer at a

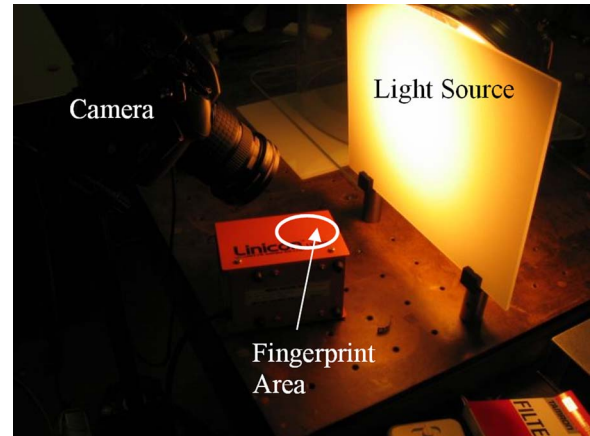


Fig. 3. (Color online) Example experimental setup overview for Fig. 5.

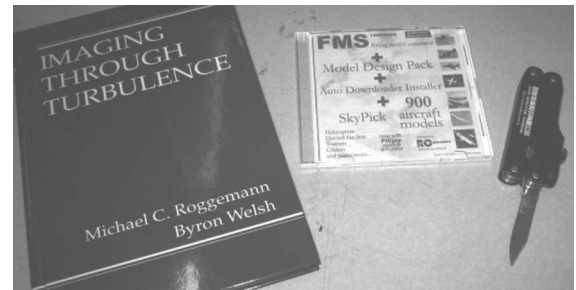


Fig. 4. Picture of the three sample items bearing latent fingerprints: a hardcover book, a plastic CD case with underlying insert patterns, and a stainless steel blade of a Swiss army knife. Experimental results on these items are presented in Figs. 8–10.

given orientation angle in front of the camera and taking a picture cannot provide complete information about the polarization state of the received light. By taking three pictures with the polarizer oriented at three different angles, for example, $\varphi = 0, 45$, and 90 deg, we can recover I_U , I_A , and θ for each pixel of the image using the following expressions:

$$I_U = (I_0 + I_{90})/2,$$

$$I_A = \sqrt{(I_{45} - I_U)^2 + (I_U - I_{90})^2},$$

$$\theta = \arctan[(I_{45} - I_U)/(I_U - I_{90})]/2. \quad (2)$$

Here indices 0, 45, and 90 indicate the orientation of the polarizer in degrees when the image was taken. Because θ and $\theta + \pi$ are indistinguishable for phase-blind visual sensors in most conventional cameras, the meaningful range of θ is restricted to $(0 \sim \pi)$. We usually use θ in the range from 0 to π . Polarization camera systems able to rapidly take the required pictures have been developed by Wolff and his colleagues.^{31–33} The formulation and symbols used here follow from our previous work^{29,30} and are slightly different from those used by Wolff. Since the background object pattern is most likely caused by pigments beneath the transparent substrate that is used to hold them, the object pattern intensity signals are mostly due to diffuse reflection, which is nearly unpolarized, and thus I_A and sometimes p are close to zero. Thus, with our polarization technique we can extract the purely specular

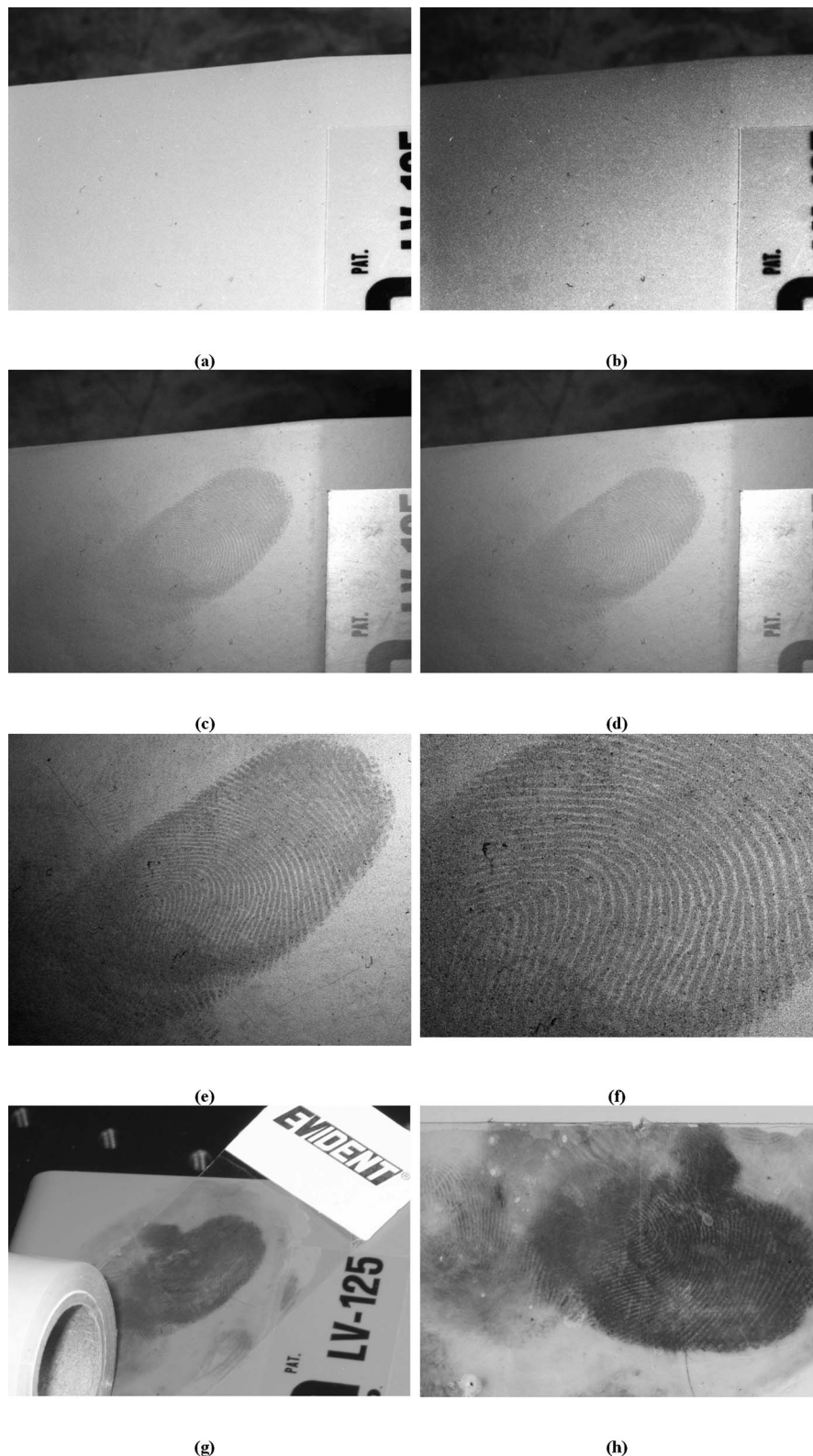


Fig. 5. Fingerprint detection experiment on a sample surface, a metal case of a pump painted orange. (a) Sample surface picture taken under ordinary lighting, linearly scaled. (b) Same as (a), but by histogram equalization for contrast enhancement. (c) The same surface as (a) and (b) taken under our special lighting setup in which the clean surface without fingerprint residue is showing strong specular reflection. The fingerprint residue disrupts the specular reflection geometry so its pattern is revealed as a dark diffuse reflection pattern. This image is linearly rescaled. (d) Same as (c), only the contrast enhancement is done using histogram equalization. (e) Zoom-in view of the fingerprint revealed in (c) and (d). (f) Further zoom-in view of (e), showing the very fine details of the recovered fingerprint pattern. (g) The same fingerprint being lifted with tape after being dusted with forensic black magnetic powder. (h) The fingerprint lifted using the traditional powdering and tape lifting. The fingerprint lifted by the proposed new method as shown in (e) and (f) is cleaner.

reflection component from the top surface by computing images of I_A or p for every image point. Such images often carry a substantial contrast between the fingerprint residue pattern and the clean area in between. Note that if only 0 and 90 deg orientation images are taken, the fingerprint may still be enhanced in the polarization-difference image,^{34–38} but the 0 or 90 deg direction must be nearly parallel to either the object surface or the fingerprint ridge surface, which can be challenging to arrange when the surface is not flat. Figure 3 is a view of our experimental setup that is arranged according to the geometry shown in Fig. 1(d). Figure 4 shows some of our test items that are often found to bear fingerprints.

3. EXPERIMENTS

A step-by-step application of the new optical method is presented in Fig. 5. Figure 3 gives an overview of the ex-

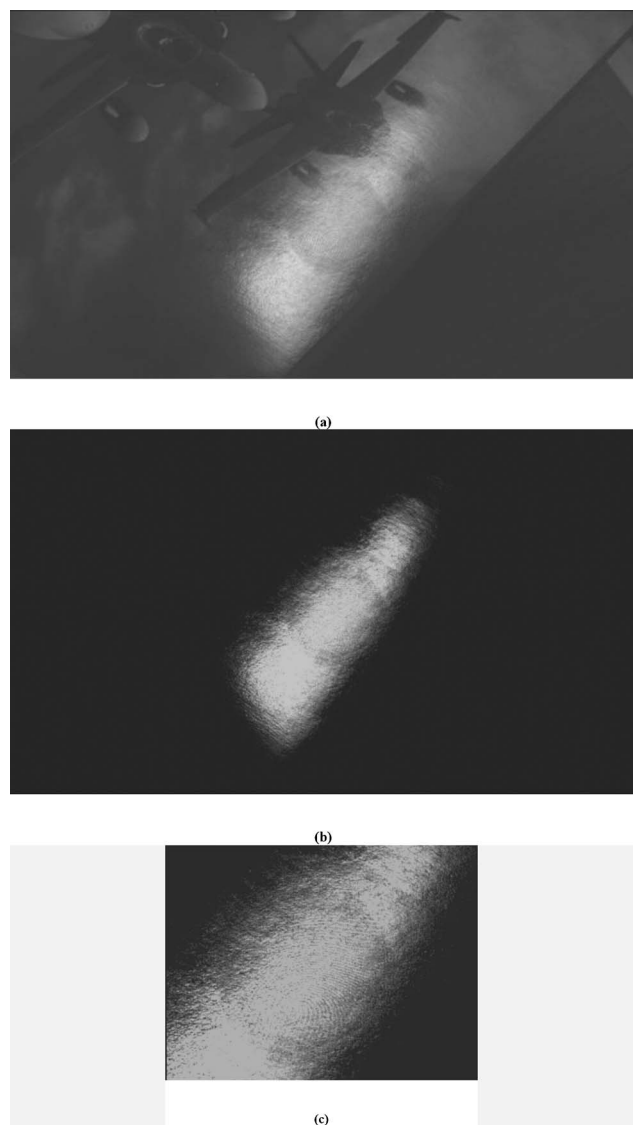


Fig. 6. Paper calendar cover with underlying picture. (a) A fingerprint is revealed by specular lighting. (b) Same item as in (a) but with polarization processing. This is the I_A image; background is completely removed. (c) Zoom-in view of the fingerprint in (b).

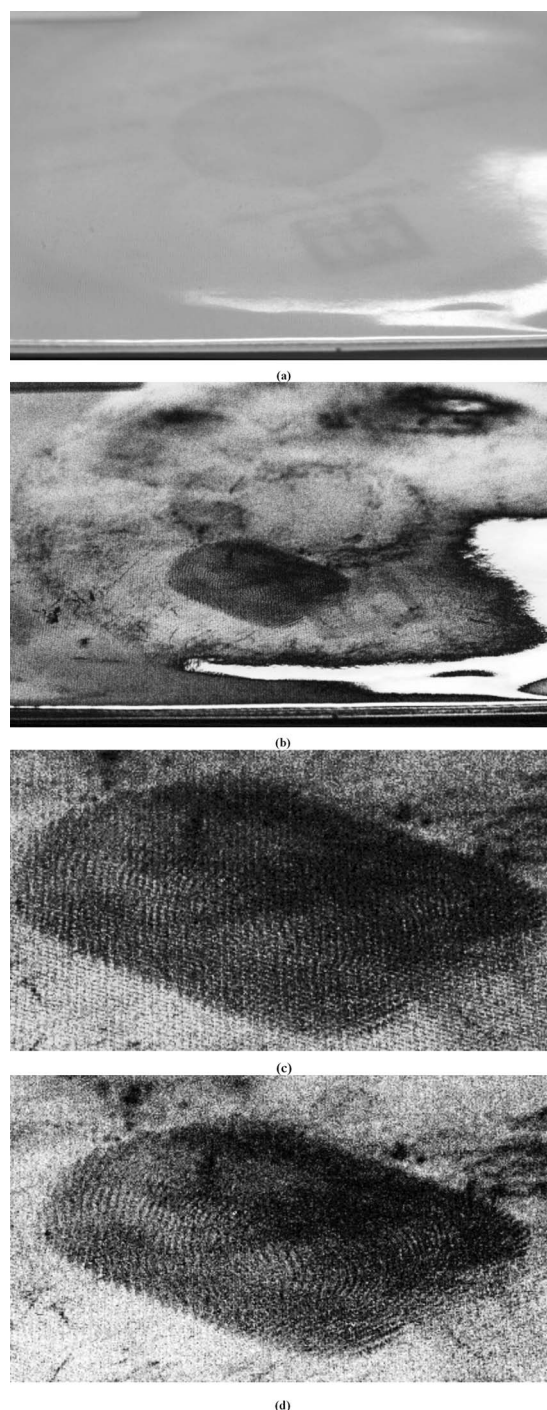


Fig. 7. Soft plastic CD sleeve with white cotton lining underneath. (a) Under ordinary lighting. (b) Polarization I_A image. The latent fingerprint on the CD sleeve is exposed in high contrast. (c) Zoom-in view of the fingerprint in (b). (d) The periodic pattern caused by the cotton lining as seen in (c) can be removed by Fourier-transform processing.

perimental setup when the specially arranged light is on and the ordinary room light is turned off. We have performed the experiments with both the room light on and off and found that the results are very similar. This means that our method can be easily applied to a crime scene without strict ambient lighting control. The surface being inspected is the metal casing of an electric air pump (Linicon), which is painted orange. Figures 5(a) and 5(b)

show how the surface looks with the specially arranged lighting turned off and the ordinary diffuse fluorescent room light on. The image in Fig. 5(a) is shown with a common digital enhancement available in most image-processing software, setting the brightest pixels in the image to the maximum possible value allowed by the display, and the darkest pixels to the lowest display value and linearly rescaling the rest of the pixel intensity val-



(a)



(b)

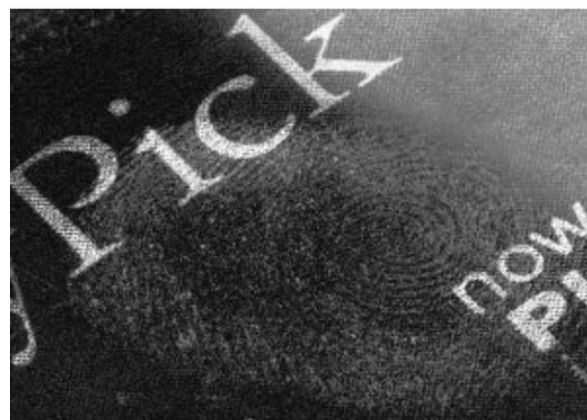


(c)

Fig. 8. (a) Close-up view of the hardcover book bearing a latent fingerprint under normal (no polarizer, no special lighting arrangements) viewing conditions. Note that this image has undergone digital linear contrast enhancement but the fingerprint mark is still not visible. (b) The same area as in (a) but taken with our specially arranged specular lighting condition. The latent fingerprints are revealed. (c) The same area as in (a) but taken with our specially arranged specular lighting condition plus polarization image processing. This is the I_A image linearly rescaled to fit an 8 bit display. The latent fingerprints are revealed, and at the same time the background pattern from the book title is greatly suppressed.



(a)



(b)



(c)

Fig. 9. (a) Close-up view of the plastic CD case with insert pattern under normal viewing conditions. No fingerprint is visible although the image has undergone digital linear contrast enhancement. (b) The same area of the plastic CD cover with the insert pattern as in (a), but taken with our specially arranged specular lighting condition with three different polarizer orientations and then the degree of polarization image computed. The latent fingerprints are revealed. (c) The same area of the plastic CD cover with the insert pattern as in (a), but taken with our specially arranged specular lighting condition plus polarization image processing. This is the I_A image linearly stretched to fit an 8 bit display. The latent fingerprints are revealed and at the same time the background pattern from the CD insert is greatly suppressed. The upper right corner of images (b) and (c) appears brighter because those areas are showing the specular reflection image of the light source. This is an example where the fingerprint stained area, rather than the adjacent clean surface, shows specular reflection.

ues. Figure 5(b) presents the same image data as in Fig. 5(a), but enhanced instead by histogram equalization. This enhancement method remaps the pixel values according to the histogram distribution of their magnitudes, distributing them more evenly over the dynamic range of

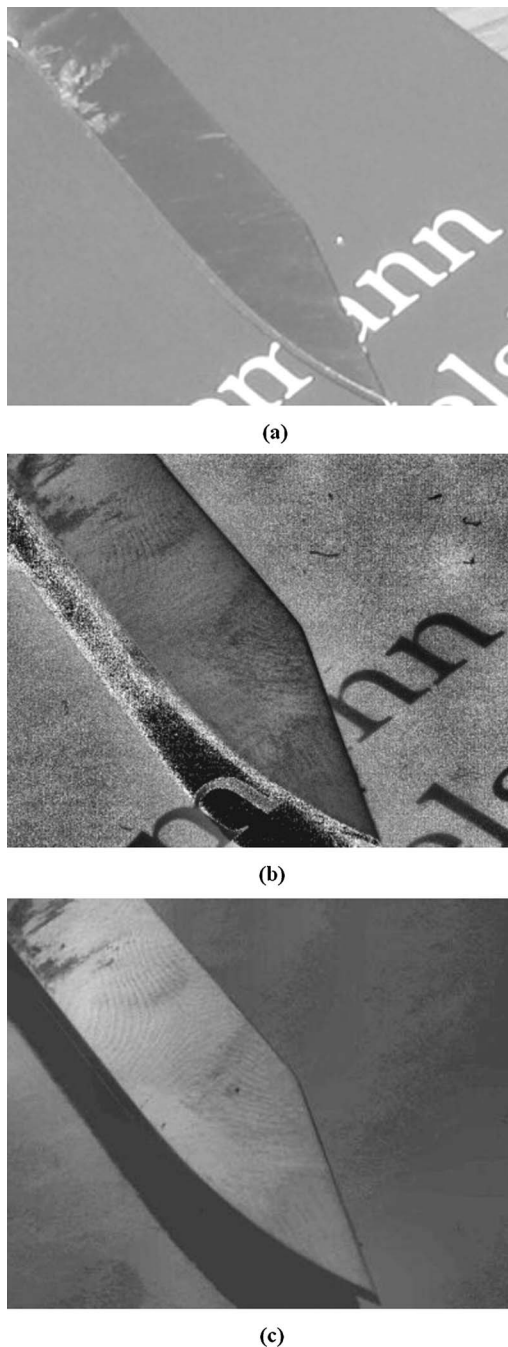


Fig. 10. (a) Close-up view of the stainless-steel Swiss army knife under normal viewing conditions. No fingerprint is visible although the image has undergone digital linear contrast enhancement. (b) The same area of the stainless-steel Swiss army knife as in (a) but taken with our specially arranged specular lighting condition plus polarization processing. The latent fingerprints are revealed in the degree of polarization image. (c) The same area of the stainless-steel Swiss army knife as in (a), but taken with our specially arranged specular lighting condition plus polarization image processing. This is the I_A image. The latent fingerprints are revealed and at the same time the background pattern from the book cover is greatly suppressed.

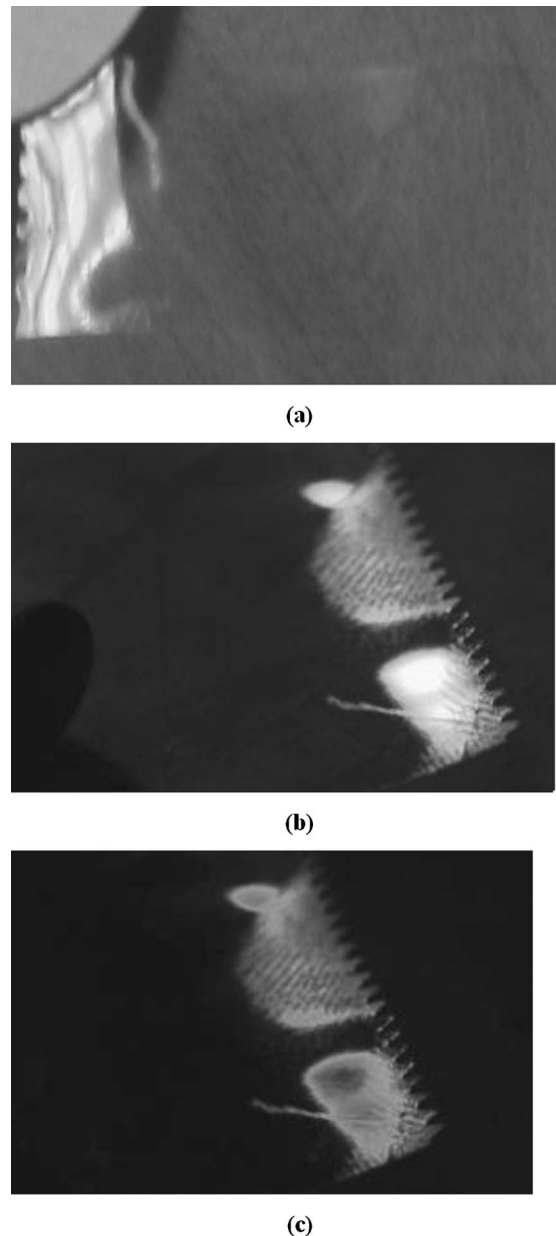


Fig. 11. (a) Transparent tape under normal viewing conditions. No fingerprint is visible. The tape itself is barely recognizable since it is transparent. (b) Fingerprint found on the sticky side of the tape using specular reflection. (c) Fingerprint found on the sticky side of the tape using polarization. The image is the I_A image. Note that no ordinary digital contrast enhancement is used on any of the images in this figure.

the display (see Ref. 39). These two images illustrate the latent nature of the fingerprint: The natural contrast is so low that not only can the unaided human eye not detect it, but even widely used digital image enhancements do not reveal its presence. Figures 5(c) and 5(d) present images taken with only the specular illumination turned on and digitally enhanced with the same methods as used to produce Figs. 5(a) and 5(b), respectively. Imaging the light specularly reflected from the surface yields a major enhancement not achievable with the digital enhancements alone, an enhancement traditionally achieved with powders and chemicals, but completely without destructive side effects. Figures 5(e) and 5(f) are zoomed-in views

showing the detailed quality of the recovered fingerprint images. As an example comparison with the fingerprint quality lifted by a conventional method, Fig. 5(g) shows the same fingerprint being lifted after being dusted with forensic black magnetic powder. Figure 5(h) shows the fingerprint lifted by a forensic sticky tape after dusting. The fingerprint image quality recovered by the proposed noncontact method is more consistent compared with the results obtained by powdering. It is difficult to spread the powder evenly across the whole fingerprint, and an area with too much or too little powder will be lifted with lower quality. Furthermore, the process of lifting by sticky tape can itself introduce missing parts in the fingerprint.

The results of another experiment employing our non-invasive optical method are illustrated in Fig. 6. In this case, the surface with the latent fingerprint was the paper cover of an ordinary desk calendar [Fig. 6(a)], which presented a greater challenge than the solid colored metallic surface. The paper surface contained a printed pattern whose light absorption interferes with the optical detection of the fingerprint. We used both specular reflection and polarization analysis to extract the latent fingerprint. For the polarization analysis, images were taken with a linear polarization analyzer mounted in front of the camera and oriented at three different angles. The picture displayed in Fig. 6(b) is the value image of the derived quantity I_A [see Eqs. (2)]. We emphasize here that Fig. 6(b) is not an image of the ordinary intensity distribution, but rather a mapping of a certain physical quantity derived from the polarization distribution of the light comprising the image. The specular component of the surface reflection is now evident, and the background pattern is gone. Figure 6(c) shows a cropped close-up of the fingerprint area of the image seen in Fig. 6(b). These results lead to two additional conclusions: First, the noninvasive optical method can extract latent prints from some paper surfaces as well as from smoother surfaces; and second, the processing of the polarization information in the image can further enhance the quality of the recovered latent fingerprint under certain conditions.

Sometimes the specular reflection component can be obscured by more intense diffuse reflection. We applied our methods to such a case, deliberately picking one of the strongest diffuse reflectors, a white cotton lining underneath a soft clear plastic CD sleeve (Fig. 7). Figure 7(a) shows an image taken without a polarizing filter in front of the camera. The diffuse white light is so strong that the specular reflection output can barely enhance the latent fingerprint on the plastic surface. However, the polarization-based analysis followed by the histogram equalization readily enhances the latent fingerprint [Figs. 7(b) and 7(c)].

Figures 8–10 illustrate the fingerprint detection and lifting capabilities of our new methods applied to several common items and surfaces. Note that our method is not restricted to viewing the surface at a right angle, and our use of polarization is not restricted to glass and is not used for removing glare.

The sticky side of a tape has traditionally caused trouble with invasive methods, especially methods that apply powder to the surface. Most powders and reagents can stick easily anywhere on the sticky surface, not just

the fingerprint area. In contrast, the sticky side of the tape is ideally suited to our method. The sticky material is a thin coat of pliable semitransparent dielectric that fits our surface model perfectly. Whether the latent fingerprint mark is formed by skin residue or by a plastic mark formed on the sticky surface, our surface model predicts that high-contrast intensity or polarization images can be formed with proper lighting. We tested our method on a piece of transparent packing tape and the results are very good (Fig. 11). An example of plastic fingerprint mark detection using our method is shown in Fig. 12.

Figure 13 shows a series of experiments using both the specular-reflection-only-based and the polarization-based method detecting a fingerprint on the metal case of a pump (the same pump surface as appeared in Fig. 5). Here the observing view angle of the camera is varied (with a corresponding change in the incident light direction to maintain the specular reflection relationship). Three angles, 30, 45, and 75 deg, are chosen to represent near-frontal, near-Brewster's, and near-grazing view angles. It is clear that the near-grazing angle is unsuitable because it is difficult to see the fingerprint pattern. On the other hand, the light from the light source used here is definitely unpolarized. As predicted by the Fresnel equation, near the Brewster incidence angle of the sample surface, the reflected light from the clean sample surface has a large degree of polarization while the light reflected

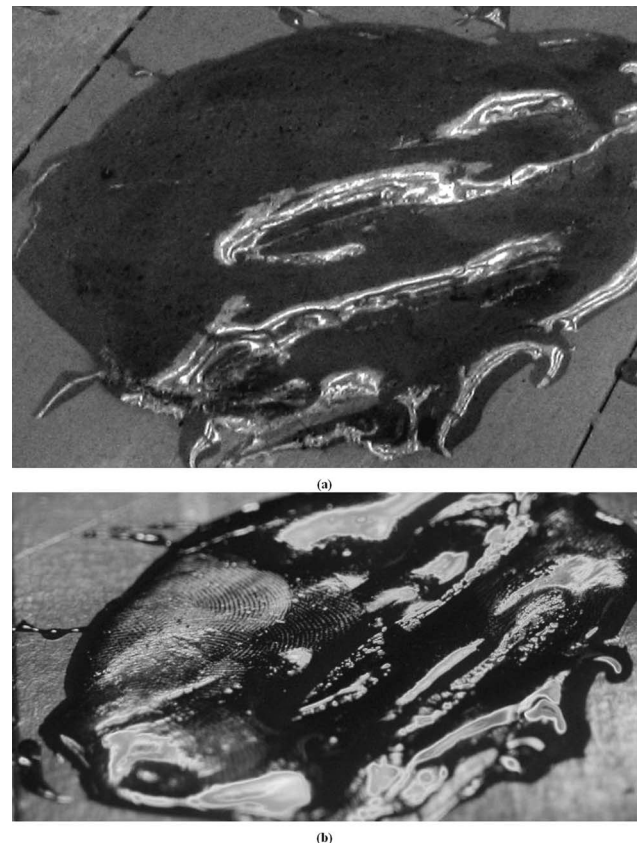


Fig. 12. (a) Piece of hardened epoxy resin under ordinary lighting conditions and view. No fingerprint is visible even after a linear rescale to fit an 8 bit display. (b) Plastic fingerprint mark revealed on the same piece of hardened epoxy resin as in (a) in the degree of polarization image. No ordinary digital contrast enhancement is used on this image.

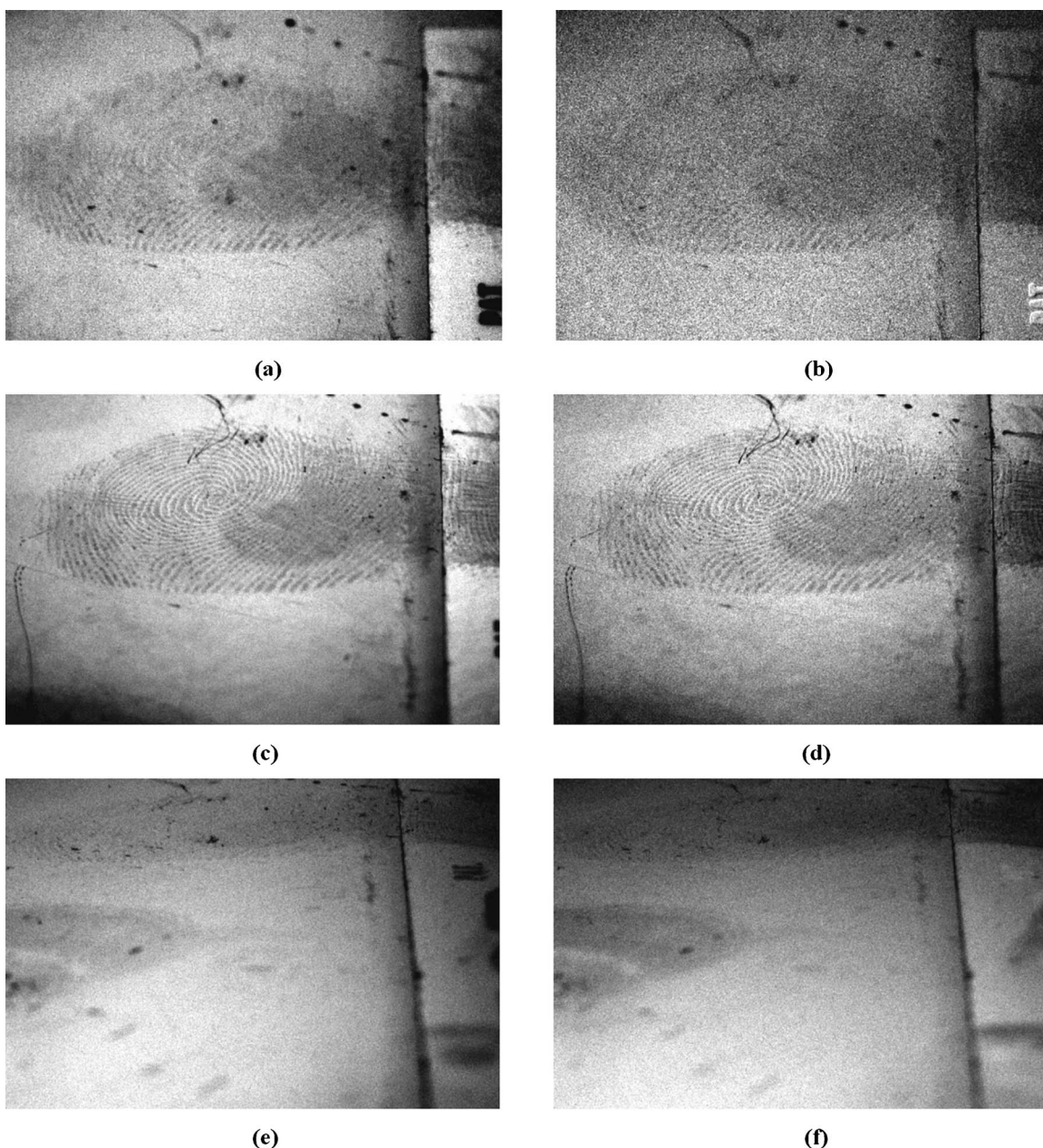


Fig. 13. Comparison of fingerprint lifting at different view angles (varying both the incident angle of the light source and the view angle of the camera simultaneously to maintain the specular reflection condition described in our theory). All images are for the same fingerprint taken within ~ 1 h of the experiment session. View angles (the angle between the surface normal of the sample to the view direction of the camera) are ~ 30 deg for (a) and (b), 45 deg for (c) and (d), and 75 deg for (e) and (f). Images (a), (c), and (e) are contrast enhanced (linear gray-level stretch) U , representing the specular-reflection-based method. Images (b), (d), and (f) are contrast enhanced (linear gray-level stretch) A , representing the polarization-based method. It is clear that at a near-grazing angle (75 deg) it is difficult to see the fingerprint pattern. At near-frontal view (30 deg) the polarization signal is very weak, so after contrast enhancement the result is very noisy. We get the best results at ~ 45 deg.

from the fingerprint-tainted area is still relatively unpolarized. This creates a good contrast in several kinds of polarization images when the incident light angle is near the Brewster incidence angle of the sample surface and relatively poor contrast at other angles. However, at exactly normal incidence to the sample surface the reflected polarization from the clean sample surface is the same as the incident one, unpolarized, and is not much different from the light reflected from the fingerprint-deposited area. Therefore we see poor results in all polarization images when light from our light source is incident at an ex-

actly normal-incidence angle to the sample surface. In summary it is best to pick a viewing angle close to Brewster's angle, typically from 45 to 60 deg from the surface normal.

Figure 14 is exactly the same experiment setup as in Fig. 13, except that these images were taken under an almost darkroom environment (room lights turned off, doors and windows shut) while Fig. 13 was taken under no special control of ambient room light. In fact we would like to point out that *all* experiment pictures except Fig. 14 in this paper were taken without special control of am-

bient room light (i.e., room light from the ceiling was left on; doors and windows were left as is). We note that our method works well without the need of a highly controlled laboratory darkroom. Please compare corresponding images in Figs. 13 and 14. One can hardly see any significant improvement in Fig. 14 where experiments were taken in a controlled darkroom environment. In fact they are almost identical. The reason behind this result can be described as follows: Irradiance is related to both the

power of the light source and the distance between the light source and the surface. In a typical office or residence room the lighting is not much stronger than a flashlight or desk lamp that would be used in our setup. Furthermore the light used to detect fingerprints can easily have the advantage of being much closer to the surface under examination. In our experiment we put a lux meter on the surface and we got ~ 2000 lux reading when both the room light and the dedicated light source were on and

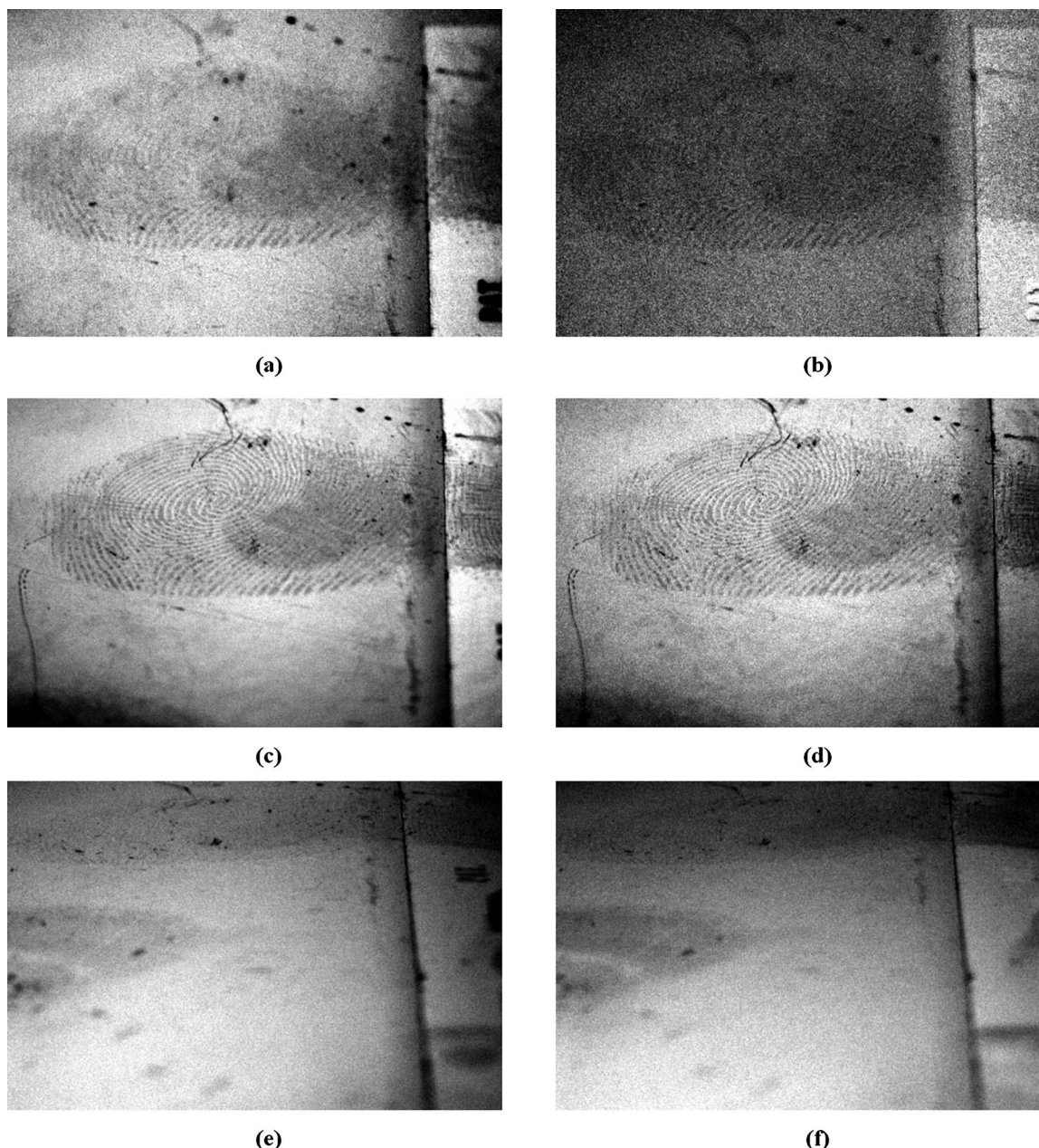


Fig. 14. Exact same fingerprint target and the same experiment as shown in Fig. 13, with only one important difference: The pictures shown here were taken with all ordinary room light shut off and the door shut to create a almost darkroom environment. We would like to point out that all experiment pictures shown in this paper except pictures in this figure were taken without any particular ambient light control, i.e., the room lights from the ceiling were not shut off and doors were not closed. It is clear that our method performs equally well with a reasonable amount of ambient light and does not need a special photography darkroom. The corresponding images in Fig. 13 look practically identical. We used a flux meter to measure the irradiance difference at the surface of the fingerprint sample for both ambient light on and ambient light off, and the readings are around 2000 and 1900 lux, respectively. It is clear that as long as our controlled light source dominates the irradiance at the surface of interest, the ambient light has little effect on the effectiveness of our method and thus we can safely apply our method directly at many crime scenes without the need to bring the sample to a dedicated laboratory darkroom.

a 1900 lux reading when we turned off the room light and shut the doors and windows to create a darkroom environment leaving only the dedicated light source illuminating the surface. These numbers indicate that the ambient light accounted for only $\sim 5\%$ total irradiance of the surface, and the dedicated light source clearly dominated. This means that our method can be applied directly at many crime scenes without the need to bring samples back to a special laboratory class darkroom. This statement should not be misinterpreted to mean that we claim that our method works in all possible ambient light conditions without some control. It is well known that the irradiance of direct sunlight on a sunny day is several orders of magnitude stronger than any man-made light source, so one should not try to perform this method under direct sunlight. For indoor environments it may generally not be a problem to control stray light by either turning off some lights or avoiding direct illumination of a room light or temporarily blocking certain ambient light. If a particularly strong light is coming from a particular direction, one may simply use that light as the main light source. The main point we are raising here is that our method does not require a darkroom as much as does developing a traditional camera film, where any stray light would expose and ruin the film. Our method only needs to have one dominating light source with a known and controllable direction of illumination.

4. THEORY OF THE APPLICATION OF SPECULAR REFLECTION TO LATENT FINGERPRINTS

Modeling surface reflection on a microscopic scale is complicated and depends heavily on the detailed knowledge of the molecular material composition of the surface material. However, macroscopically, a more general model can be used that applies to a wider range of surfaces without the need for details about the surface with acceptable reduction in accuracy. This is desirable in many practical applications, notably in computer vision and graphics, where the details of the chemical and physical composition of surfaces are not known or are not of vital importance. Beginning with Refs. 40 and 41, many surface reflection models based not on the exact chemical composition but rather on a plausible statistical model of the surfaces were proposed (see also Refs. 42 and 43). A review of various models can be found in Refs. 44 and 45. Because in our applications we intend to extract the fingerprint without using any chemical analysis, the possibility of knowing the properties of the surface material beforehand is excluded. However, a simple model that describes a general trend is good enough, because the ultimate form required for a fingerprint image is that of binarized black-and-white regions separating the ridge and furrow areas. There is no need to recover or to predict the exact brightness differences in the gray-level images taken for the purpose of recovering fingerprint marks. The simple Phong model⁴³ and Lambertian model,⁴⁰ both widely used in many computer vision and graphics algorithms, satisfy these purposes.

Macroscopically, two well-known general types of reflection can be named. The Lambertian model describes a surface producing perfectly diffuse reflection as

$$I = I_p k_d \cos \theta = I_p k_d (\hat{n} \cdot \hat{l}), \quad (3)$$

where I is the intensity of the image point sensed by the camera, I_p is the point light source's intensity, k_d is the reflection coefficient (either for a particular wavelength or for a particular camera's spectral response), and θ is the angle between the surface normal \hat{n} and the unit vector \hat{l} in the direction of the light source as viewed from the point of reflection (see Ref. 44). Note that the diffusely reflected light has the same intensity for all viewing directions.

Another type of reflection is that of highlights, or mirrorlike reflection observed on many smooth surfaces. A more subdued version is usually called sheen. The Phong model is given by

$$I_\lambda = I_{a\lambda} k_a O_{d\lambda} + f_{att} I_{p\lambda} [k_d O_{d\lambda} \cos \theta + W(\theta) \cos^n \alpha], \quad (4)$$

where λ is the wavelength of the light, subscript a denotes the ambient light source, subscript p denotes the point light source, subscript d denotes a diffuse reflection component, the new symbol O denotes color components in human and digital color vision components, f_{att} is the inverse square of the decay distance of a point light source intensity, $W(\theta)$ is the diffuse reflection coefficient of the surface with a point light source angle of incidence θ , and α is the angle between the exact view direction predicted by the law of reflection and the actual view direction [as shown in Fig. 1(d)]. For the current study, the most important information derived from Eq. (4) is that the intensity is proportional to $\cos^n \alpha$. This gives a simple way to model a rapid decay in intensity if the view angle is different from that predicted by the law of reflection. This term suggests that if the camera, the light source, and the surface being inspected are arranged in a way predicted by the reflection law [see Fig. 1(d)], the image point for the original smooth surface without skin residue will show an intensity typical for specular reflection, while the area with skin residue will have much less specular reflection due to the slight change in the direction of surface normal caused by the skin residue. The more mirrorlike a surface can be modeled, the larger the power of cosine decay it exhibits, which means better contrast in our specular-reflection-based latent fingerprint detection and lifting technique.

Providing that all other factors are equal, the intensity of the specular reflection component is in general much stronger than the diffuse reflection component. Although this statement is not always true, it has been widely accepted as a good rule of thumb in the majority of practical situations.²⁶ Since specular reflection has a tendency of concentrating reflected energy in a small solid angle, as opposed to the diffuse reflection that spreads all the reflected energy into a full hemisphere, the same amount of reflected energy will result in a much greater flux density in specular reflection and thus in image brightness. Specular reflection tends to be reflected only once from the smooth surface, while diffuse reflection gives light that experiences a multiple scattering inside the surface before reemerging. Each scattering only weakens the intensity but seldom enhances it. Wolff²⁶ experimentally measured the ratio between specular and diffuse reflec-

tion intensities for several different surfaces and reported ratios varying from $\sim 150:1$ to $250:1$. For many digital sensors with 8 bit brightness resolution, this is close to the maximum intensity ratio of $255:1$. This gives a strong support to our main assumption that the specular reflection component is in general stronger than the diffuse one. Our experimental results so far also support the validity of such an assumption.

In Ref. 26 another important theoretical result relating to a fingerprint detection issue was reported, i.e., if the reflection coefficient of the diffuse component is more than $\sim 1/33$ the reflection coefficient of the specular component, the diffuse component can be stronger or at least comparable to the specular component. If the underlying surface consists of complicated patterns similar in strength and spatial frequency to the latent fingerprint pattern on top of it, the method based on purely specular reflection is not satisfactory. This is the point where the polarizer should be used.

The behavior of the specular component is governed by the well-known Fresnel reflection coefficients formula⁴⁶:

$$r_{\perp} \equiv \left(\frac{E_{0r}}{E_{0i}} \right)_{\perp} = \frac{n_i \cos \theta_i - n_t \cos \theta_t}{n_i \cos \theta_i + n_t \cos \theta_t} = \frac{\sin(\theta_i - \theta_t)}{\sin(\theta_i + \theta_t)},$$

$$r_{\parallel} \equiv \left(\frac{E_{0r}}{E_{0i}} \right)_{\parallel} = \frac{n_t \cos \theta_i - n_i \cos \theta_t}{n_i \cos \theta_t + n_t \cos \theta_i} = \frac{\tan(\theta_i - \theta_t)}{\tan(\theta_i + \theta_t)}, \quad (5)$$

where the subscripts i , t , and r stand for incident, transmitted, and reflected components, respectively. The subscripts \perp and \parallel are related to the plane of incidence. In Fig. 1(b) the plane of this paper is the plane of incidence. In the case of specular reflection it contains both the incident and the reflected light-wave vectors. It is well known (see, e.g., Ref. 46) that r_{\parallel} can be exactly zero at Brewster's angle θ_B , which is given as

$$\tan \theta_B = n_t/n_i. \quad (6)$$

If light is incident from the air, $n_i \approx 1$, while n_t varies from 1.4 to 2.0 for most of dielectrics in the visible band (wavelength of ~ 400 – 700 nm).⁴⁶ Equation (6) shows that the corresponding Brewster's angles vary from 55 to 74 deg, respectively. Although there are certain materials with a higher refractive index,⁴⁶ we confine our discussion to the above-mentioned range of n_t . Therefore, when we consider the angle of incidence between 55 and 74 deg, the reflected light is highly partially polarized with the plane of polarization perpendicular to the plane of incidence. This case is referred to as horizontal polarization with respect to the surface being inspected. So far we have only discussed dielectric surfaces that are adequate in most cases since pure metallic surfaces are rather rare in everyday life. Pure metal surfaces are oxidized quickly and the actual layer responsible for specular reflection is often either the oxides on the surface or the protective painting layer that is also a dielectric material. In fact, a lot of metallic-looking merchandise today is actually coated with highly reflective dielectric paints. In cases when the underlying pure metal reflects more light than the upper dielectric coating, the proposed method may not work.

5. DISCUSSION

The currently popular latent fingerprint detection and extraction methods used by law enforcement agencies include, but are not limited to, powdering, Sudan Black staining, iodine fuming, ninhydrin (sometimes followed by further enhancement with zinc chloride) and 1,8-diazafluoren-9-one (DFO) application, silver nitrate development, cyanoacrylate (glue) fuming, Gentian Violet staining, vacuum metal deposition, laser-excited luminescence, and reflected ultraviolet imaging system (RUVIS).^{1–4} While this list may seem long, there is still need for new methods, because every existing method tends to be unsuitable for some surfaces, due either to its inadequacy in lifting the print from or to its damaging side effects to the surfaces. In particular, the chemical and physical processing directly applied to the fingerprint-bearing surface to extract latent fingerprints can potentially inflict deleterious effects upon the fingerprint, the operator, and/or the object surface being examined.^{1–3,10,18} For example, the iodine vapor in the iodine fuming method is highly corrosive and toxic.² Thus, in practice, often valuable and/or irreplaceable objects are not searched for fingerprints at all,^{2,3,7} except in a few major cases involving extremely serious crimes. Furthermore, the chemicals used to enhance fingerprint contrast or to induce luminescence may need a long processing time, are sometimes toxic, environmentally unfriendly, or radioactive. The process to speed up the chemical reaction can be dangerous, e.g., sodium hydroxide used to speed up cyanoacrylate fuming can generate extreme heat if the two come into contact.⁴ Samples are often baked to high temperature after many fuming procedures to speed up the print development. Chemicals used for fingerprint enhancement can often be harmful to the operator if not handled correctly using proper procedures and protective equipment because they are designed to react with or adhere to the fingerprint residues, which are the same material found on human skin.³ Some chemicals require specific solvents that have undesirable side effects, e.g., the phenol in the solution for Gentian Violet is highly caustic and poisonous.²

Laser-induced fluorescence was one of the first optical methods for lifting latent prints, utilizing induced luminescence of the fingerprint material.^{1–3,10} However, there are several factors limiting its use. The natural fluorescence signal (without the prior application of strongly fluorescent chemicals or powders) is in general very weak. Thus the laser used must operate in a specific frequency, and must have a high enough power rating. Such a laser device is fairly expensive and bulky (due to power and cooling requirements), and thus it can be deployed only to a few large and well-funded crime laboratories and is not easily made portable outside a dedicated crime laboratory.¹⁸ A less powerful laser or arc lamp with a filter can be used as a substitute but will be less effective. As a result, these alternative systems need chemical enhancements. The fact that many commonly encountered fingerprint-laden objects found at a crime scene contain organic substances that also fluoresce when excited by a laser often cause significant background noise.^{1,2,10,13,17–19} Thus, laser-excited luminescence, like other existing methods, cannot be applied to certain types of surfaces. It

has also been found that the signal strength of the natural fluorescence of fingerprints varies greatly from person to person and even from time to time of the same person.¹⁰ As a result, in real applications laser-excited luminescence techniques are more often used with the aid of fluorescence-enhancing chemicals to get better and more consistent results.^{1,2,13,17–19} However, the use of chemical fluorescence enhancers negates the noncontact advantage and the combined method reverts back to an invasive method.

RUVIS was pioneered by research at the National Police Agency of Japan and was originally targeted for enhancing cyanoacrylate-developed latent prints. It is found that the cyanoacrylate-developed latent prints that are translucent under visible light become opaque under UV. Latent prints deposited in sebaceous matter or oily residue can sometimes be detected by RUVIS before the application of enhancing materials. The oil strongly absorbs UV and shows up as dark patterns under UV light and detector. RUVIS can sometimes detect fingerprints up to a year old in a purely noncontact style.¹ The drawback is the need of a relatively expensive specialized UV light source and sensors. UV light can be harmful to both human eyes and skin, so proper precaution and protective gear are necessary. Bramble *et al.*⁴⁷ proposed using a laser in the UV band to induce luminescence that is also in the UV band. Although the UV laser is not considered invasive, they find that the luminescence property of the fingerprint material decreases significantly after being exposed to a UV laser for an extended period of time.⁴⁷

The episcopic coaxial illumination method proposed by Pfister²⁰ uses the intensity difference between specular and diffuse reflection to enhance the visibility of latent fingerprints. The design always looks at the surface from a right angle. The advantage is that the picture will always appear in frontal view suitable for archiving. However, with the advent of digital image processing, an oblique view can be easily reprojected back to the frontal view, so it is not that crucial. We have shown that by varying the observation angles we can get a better contrast in some cases [compare, e.g., Figs. 12(a) and 12(b)]. We have also shown that the partially polarized nature of oblique specular reflection can significantly enhance the contrast of latent fingerprints and at the same time suppress the interfering background pattern. Viewing the surfaces only at a right angle precludes the use of polarization because the specular reflection at a right angle is not partially polarized by the surface.

There is a commercial product called the fingerprint camera that has existed for a long time.⁴ Some may confuse it as yet another noncontact optical method for the detection of latent fingerprints. However, this device is in fact an ordinary camera customized to record nonexemplar fingerprints that have been enhanced by other methods (e.g., by an application of chemicals) or for patent fingerprints that are already visible. The customization includes dedicated lighting to reduce uneven lighting, shadow, and glare; a fixed-object distance and fixed focus, aperture, exposure time, etc. These preset camera settings enable law enforcement officers who may not be photographic experts to be able to take good fingerprint pictures consistently for court use. Such a fingerprint

camera does not have any contrast enhancement or detection capability for hidden latent fingerprints.

The novel optical method we propose here is capable of recovering high-quality digital images of hidden latent fingerprints without the application of any chemicals or physical contact with the examined object. Like any other existing latent fingerprint enhancement technology, our method has its limitations. Our method is designed to take advantage of the intensity and polarization differences between specular and diffuse reflections, so it works best on a relatively smooth and nonporous surface. The chance of detecting fingerprints on a highly porous and absorbing surface like certain kinds of paper using our method is fairly low. However, our method possesses unique advantages over existing methods on smooth surfaces in that complex patterns on the surface can be easily suppressed optically using our polarization method. Note that while the most common use of a photographic polarization filter is to remove glare, our use of the polarizer is quite the opposite. Our polarization method, in a sense, extracts only the specular glare that was usually treated as a mere nuisance. Specifically we discovered that inside the specular glare under certain conditions a high-contrast clean latent fingerprint image is present.

Menzel²² briefly mentioned the possibility of using polarization to detect fingerprints on glass. We have shown that polarization can be used to enhance fingerprint visibility on a wide variety of surfaces, not just on glass. We also show that polarization can be used to remove interfering background patterns that have not been mentioned before. Another advantage of our method is that it is less affected by the degradation of latent fingerprints over time compared with methods that rely on chemical reactions with the organic residues or water in latent fingerprint marks. Over time an exposed latent fingerprint mark will lose its water contents via evaporation, and the amino acid components will degrade and its chemical properties will change.^{1–4} Since our method does not rely on water or detailed chemical composition of the fingerprint mark, our method is less likely to be affected by chemical decomposition. As long as the geometric difference in the surface remains, our method can be used effectively. The example pictures shown were taken up to several weeks after the fingerprint was made (and kept in our laboratory/office environment undisturbed) and they show little degradation of quality.

We have shown that our method can work under regular room light without the need of a highly controlled laboratory darkroom. This may enable law enforcement officers to use our method right at the crime scene without the delay of sending samples back to a special crime laboratory. This effectively means that our method can usually examine the most fresh fingerprint samples. The only requirement is a strong dominating light source illuminating the surface examined from a known direction. This can be easily achieved by either using a strong portable light source close to the target surface or by simply using the strongest directional ambient light source found at the crime scene. For most indoor crime scenes, the standard fingerprint search procedure calls for restricting the access to the crime scene with only the fingerprint specialists working at the scene during the fingerprint

search. The specialists have total control over the scene during the search so it is generally not a problem to turn on and off any room light. It is also quite easy to use something like a shade to temporarily block some ambient light, e.g., a piece of cloth, an umbrella, or even the body of the specialist because the size of a fingerprint is very small. In other words, our method can be performed directly in most crime scenes and even more cases with simple common sense regarding light control. There is essentially no need for a special darkroom similar to a film developing darkroom.

Because of the great variety of latent fingerprints that can potentially be found in very different crime scenes, no single latent fingerprint enhancement method can handle all possible cases. Since every method targets different physical and chemical properties of different kinds of fingerprints, it is often found that applying more than one method on the same surface will unveil different fingerprints for different methods.¹⁸ Thus the introduction of a new latent fingerprint detection method that uses different physical principles than those used by existing methods and one that will not interfere with other methods should be beneficial to law enforcement efforts.

6. CONCLUSION

We have introduced a novel optical method to detect, enhance, and lift latent fingerprints that are otherwise difficult to see. The method is noninvasive and so will not interfere with other forensic examinations and will not inflict deleterious side effects on the surface. The equipment required is much less expensive than most other noncontact methods proposed so far. The new method is not applicable to highly porous and absorbing surfaces but works well on most other surfaces. The new method also works on the sticky side of tape, which is a particularly problematic surface for many invasive methods. The new method can be easily performed right at the crime scene without the need to bring samples to a specialized laboratory. The recovered latent fingerprint image has good quality compared with other existing methods. Since it does not interfere with other methods, it is advisable to try this method before other invasive or destructive methods.

ACKNOWLEDGMENTS

This work has been supported by the U.S. Air Force Office of Scientific Research through grants F49620-02-1-0140, FA9550-05-1-0052, and the Defense University Research Instrumentation Program grant F49620-02-1-0241.

REFERENCES

1. H. C. Lee and R. E. Gaensslen, eds., *Advances in Fingerprint Technology* (CRC Press, 1994).
2. H. C. Lee and R. E. Gaensslen, eds., *Advances in Fingerprint Technology*, 2nd ed. (CRC Press, 2001).
3. C. A. Coppock, *Contrast: An Investigator's Basic Reference Guide to Fingerprint Identification Concepts* (Thomas, 2001).
4. Federal Bureau of Investigation, *The Science of Fingerprints: Classification and Uses* (U.S. Government Printing Office, 1984).
5. S. G. Demos and R. R. Alfano, "Optical fingerprinting using polarisation contrast improvement," *Electron. Lett.* **33**, 582–584 (1997).
6. K. H. Fielding, J. L. Horner, and C. K. Makekai, "Optical fingerprint identification by binary joint transform correlation," *Opt. Eng.* **30**, 1958–1961 (1991).
7. W. R. Scott, *Fingerprint Mechanics, A Handbook: Fingerprints from Crime Scene to Courtroom* (Thomas, 1951).
8. R. D. Olsen, Sr., *Scott's Fingerprint Mechanics* (Thomas, 1978).
9. P. Margot and C. Lennard, *Fingerprint Detection Techniques* (Institut de police scientifique et de criminologie, Université de Lausanne, Lausanne, Switzerland, 1994).
10. B. E. Dalrymple, J. M. Duff, and E. R. Menzel, "Inherent fingerprint luminescence—detection by laser," *J. Forensic Sci.* **22**, 106–115 (1977).
11. E. R. German, "Computer image enhancement of latent prints and hard copy output devices," in *Proceedings of the International Forensic Symposium on Latent Prints* (Laboratory and Identification Divisions, Federal Bureau of Investigation, 1987), pp. 151–152.
12. M. C. Cubuk and S. Saygi, "A rising value in evidence detection: ultraviolet light," *Forensic Sci. Int.* **136**, 128 (2003).
13. E. R. Menzel and J. M. Duff, "Laser detection of latent fingerprints—treatment with fluorescers," *J. Forensic Sci.* **24**, 96–100 (1979).
14. E. R. Menzel, "Laser detection of latent fingerprints—treatment with phosphorescers," *J. Forensic Sci.* **24**, 582–585 (1979).
15. E. R. Menzel and K. E. Fox, "Laser detection of latent fingerprints: preparation of fluorescent dusting powders and the feasibility of a portable system," *J. Forensic Sci.* **25**, 150–153 (1980).
16. D. W. Herod and E. R. Menzel, "Laser detection of latent fingerprints: ninhydrin," *J. Forensic Sci.* **27**, 200–204 (1982).
17. D. W. Herod and E. R. Menzel, "Laser detection of latent fingerprints: ninhydrin followed by zinc chloride," *J. Forensic Sci.* **27**, 513–518 (1982).
18. K. E. Creer, "Operational experience in the detection and photography of latent fingerprints by argon-ion laser," *Forensic Sci. Int.* **23**, 149–160 (1983).
19. E. R. Menzel, J. A. Burt, and T. W. Sinor, "Laser detection of latent fingerprints: treatment with glue containing cyanoacrylate ester," *J. Forensic Sci.* **28**, 307–317 (1983).
20. R. Pfister, "The optical revelation of latent fingerprints," *Fingerprint World* **10**, 64–70 (1985).
21. C. J. Lennard and P. A. Margot, "Sequencing of reagents for the improved visualisation of latent fingerprints," *J. Forensic Ident.* **38**, 197–210 (1988).
22. E. R. Menzel, *Fingerprint Detection with Lasers* (Marcel Dekker, 1999).
23. D. Maltoni, D. Maio, A. K. Jain, and S. Prabhakar, *Handbook of Fingerprint Recognition* (Springer-Verlag, 2003).
24. R. Schwind, "Zonation of the optical environment and zonation in the rhabdom structure within the eye of the backswimmer, *Notonecta glauca*," *Cell Tissue Res.* **232**, 53–63 (1983).
25. G. Horváth, "Reflection polarization patterns at flat water surfaces and their relevance for insect polarization vision," *J. Theor. Biol.* **175**, 27–37 (1995).
26. L. B. Wolff, "Relative brightness of specular and diffuse reflection," *Opt. Eng.* **33**, 285–293 (1994).
27. B. E. Dalrymple and T. Menzies, "Computer enhancement of evidence through background noise suppression," *J. Forensic Sci.* **39**, 537–546 (1994).
28. T. Ko, "Fingerprint enhancement by spectral analysis techniques," in *Proceedings of the 31st Applied Imagery Pattern Recognition Workshop* (IEEE Press, 2002), pp. 133–139.

29. S.-S. Lin, K. M. Yemelyanov, E. N. Pugh, Jr., and N. Engheta, "Polarization enhanced visual surveillance techniques," invited paper, in *Proceedings of IEEE International Conference on Networking, Sensing and Control* (IEEE Systems, Man and Cybernetics Society, 2004).
30. K. M. Yemelyanov, S.-S. Lin, W. Q. Luis, E. N. Pugh, Jr., and N. Engheta, "Bio-inspired display of polarization information using selected visual cues," in *Polarization Science and Remote Sensing*, J. A. Shaw and J. S. Tyo, eds., Proc. SPIE **5158**, 71–84 (2003), Vol. 1, pp. 216–221.
31. L. B. Wolff, "Polarization camera for computer vision with a beam splitter," J. Opt. Soc. Am. A **11**, 2935–2945 (1994).
32. L. B. Wolff and A. G. Andreou, "Polarization camera sensors," Image Vis. Comput. **13**, 497–510 (1995).
33. L. B. Wolff, T. A. Mancini, P. Pouliquen, and A. G. Andreou, "Liquid crystal polarization camera," IEEE Trans. Rob. Autom. **13**, 195–203 (1997).
34. M. P. Rowe, E. N. Pugh Jr., and N. Engheta, "Polarization-difference imaging: a biologically inspired technique for observation through scattering media," Opt. Lett. **20**, 608–610 (1995).
35. J. S. Tyo, M. P. Rowe, E. N. Pugh Jr., and N. Engheta, "Target detection in optically scattering media by polarization-difference imaging," Appl. Opt. **35**, 1855–1870 (1996).
36. J. S. Tyo, E. N. Pugh Jr., and N. Engheta, "Colorimetric representation for use with polarization-difference imaging of objects in scattering media," J. Opt. Soc. Am. A **15**, 367–374 (1998).
37. J. S. Tyo, "Optimum linear combination strategy for an N -channel polarization-sensitive imaging or vision system," J. Opt. Soc. Am. A **15**, 359–366 (1998).
38. K. M. Yemelyanov, M. A. Lo, E. N. Pugh Jr., and N. Engheta, "Display of polarization information by coherently moving dots," Opt. Express **11**, 1577–1584 (2003).
39. R. C. Gonzalez and R. E. Woods, *Digital Image Processing* (Prentice Hall, 2001).
40. J. H. Lambert, *Photometria sive de mensura et gradibus luminis, colorum et umbrae* (Eberhard Klett, 1760).
41. K. E. Torrance and E. M. Sparrow, "Theory for off-specular reflection from roughened surfaces," J. Opt. Soc. Am. **57**, 1105–1114 (1967).
42. R. L. Cook and K. E. Torrance, "A reflectance model for computer graphics," Comput. Graph. **15**, 307–316 (1981).
43. B.-T. Phong, "Illumination for computer generated pictures," Commun. ACM **18**, 311–317 (1975).
44. J. D. Foley, A. vanDam, S. K. Feiner, and J. F. Hughes, *Computer Graphics: Principles and Practice* (Addison-Wesley, 1990).
45. S. K. Nayar, K. Ikeuchi, and T. Kanade, "Surface reflection: physical and geometrical perspectives," IEEE Trans. Pattern Anal. Mach. Intell. **13**, 611–634 (1991).
46. E. Hecht, *Optics* (Addison-Wesley Longman, 1998).
47. S. K. Bramble, K. E. Creer, W. G. Qiang, and B. Sheard, "Ultraviolet luminescence from latent fingerprints," Forensic Sci. Int. **59**, 3–14 (1993).

Fabrication of a dual-tier thin film micropolarization array

Viktor Gruev, Alessandro Ortu, Nathan Lazarus, Jan Van der Spiegel and Nader Engheta

*Electrical and Systems Engineering Department
University of Pennsylvania
Philadelphia, PA USA
vgruev@seas.upenn.edu*

Abstract: A thin film polarization filter has been patterned and etched using reactive ion etching (RIE) in order to create 8 by 8 microns square periodic structures. The micropolarization filters retain the original extinction ratios of the unpatterned thin film. The measured extinction ratios on the micropolarization filters are ~1000 in the blue and green visible spectrum and ~100 in the red spectrum. Various gas combinations for RIE have been explored in order to determine the right concentration mix of CF₄ and O₂ that gives optimum etching rate, in terms of speed and under-etching. Theoretical explanation for the optimum etching rate has also been presented. In addition, anisotropic etching with 1μm under cutting of a 10μm thick film has been achieved. Experimental results for the patterned structures under polarized light are presented. The array of micropolarizers will be deposited on top of a custom made CMOS imaging sensor in order to compute the first three Stokes parameters in real time.

©2007 Optical Society of America

OCIS codes: (120.5410) Polarimetry, (230.5440) Polarization-sensitive devices, (110.5220) Photolithography.

References and links

1. M. Born and E. Wolf, *Principles in Optics*, (Pergamon, New York, 1965).
2. J. K. Boger, "Pupil-plane speckleimaging with a referenced polarization technique," *Opt. Lett.* **24**, 611-613 (1999).
3. T. J. Rogne, F. G. Smith, and J. E. Rice, "Passive target detection using polarized components of infrared signature," *Proc. SPIE* **1317**, 3756-3764 (1990).
4. Y. Y. Schechner and N. Karpel, "Clear underwater vision," *Proc. IEEE CVPR* **1**, 536-543 (2004).
5. T. W. Cronin and J. Marshall, "Parallel Processing and Image Analysis in the Eyes of Mantis Shrimps," *The Biological Bulletin* **200**, 177-189 (2001).
6. T. Labhart, "Polarization opponent interneurons in the insect visual system," *Nature*, **331**, 435-437 (1988).
7. A. G. Andreou and Z. K. Kalayjian, "Polarization imaging: principles and integrated polarimeters," *IEEE Sens. J.* **2**, 566-576 (2002).
8. M. Momeni and A. H. Titus, "An analog VLSI chip emulating polarization vision of octopus retina," *IEEE Trans. Neu. Net.* **17**, 222-232 (2006).
9. L. B. Wolff, T. A. Mancini, P. Pouliquen, and A. G. Andreou, "Liquid crystal polarization camera," *IEEE Trans. on Rob. and Aut.* **13**, 195-203 (1997).
10. J. S. Tyo, M. P. Rowe, E. N. Pugh, and N. Engheta, "Target Detection in Optically Scattering Media by Polarization-Difference Imaging," *Appl. Opt.* **35**, 1855-1870 (1996).
11. J. S. Tyo, E. N. Pugh, and N. Engheta, "Colorimetric Representations for Use with Polarization-Difference Imaging of Objects in Scattering Media," *J. Opt. Soc. Am. A* **15**, 367-374 (1998).
12. Z. K. Kalayjian, "VLSEye: Optoelectronic Vision and Image Processing," Ph.D. dissertation, Johns Hopkins Univ., Baltimore, MD., 1999.
13. Z. K. Kalayjian, A. G. Andreou, and L. B. Wolff, "1D polarisation contrast retina," *Electron. Lett.* **33**, 38-40 (1997).
14. T. Hamamoto, H. Toyota, and H. Kikuta, "Microretarder array for imaging polarimetry in the visible wavelength region," *Proc. SPIE* **440**, 293-300 (2001).
15. J. Guo and D. Brady, "Fabrication of high-resolution micropolarizer array," *Opt. Eng.* **36**, 2268-2271 (1997).

16. J. Guo and D. Brady, "Fabrication of thin-film micropolarizer arrays for visible imaging polarimetry," *Appl. Opt.* **39**, 1486-1492 (2000).
17. G. P. Nordin, J. T. Meier, P. C. Deguzman, and M. W. Jones, "Micropolarizer Array for Infrared Imaging Polarimetry," *J. Opt. Soc. Am. A* **16**, 1184-1193 (1999).
18. V. Gruev and R. Etienne-Cummings, "Implementation of steerable spatiotemporal image filters on the focal plane," *IEEE Trans. on Circ. and Sys. II: Anal. and Dig. Sig. Proc.* **49**, 233-244 (2002).
19. V. Gruev, J. Van der Spiegel, and N. Engheta, "Image Sensor With Focal Plane Extraction of Polarimetric Information," *Proc. IEEE ISCAS* 213-216 (2006).
20. D. Goldstein, *Polarized Light*, Marcel Dekker, New York, NY, 2003.
21. <http://www.dymax.com>
22. <http://www.microchem.com>
23. J. F. Battey, "Design criteria for uniform reaction rates in an oxygen plasma," *IEEE Electron. Device Lett.*, 140-146 (1977).
24. J. M. Cook and B. W. Benson, "Application of EPR spectroscopy to oxidative removal of organic materials," *J. Electrochem. Soc.* **130**, 2459-2464 (1983).
25. T. T. Wydeven, C. C. Johnson, M. A. Golub, M. S. Hsu, and N. R. Lerner, "Plasma Polymerization," *Proc. ACS Symposium Series* 299-314 (1979).
26. <http://www.edmundoptics.com>

1. Introduction

Polarization vision contains important information about the imaged environment, such as surface shapes, curvature and material properties, which are ignored with traditional imaging systems [1]. Polarization vision techniques have been extensively used in applications such as pupil-plane speckle imaging [2], passive target detection [3], underwater imaging [4] and others. Several species of invertebrate, such as cuttlefish, mantis shrimp [5], desert ants and various other species of insects [6], rely on contrast enhancement using polarized vision, which is a vital survival mechanism in optically scattering media. The human eye perceives visual information in terms of color and intensity but it is essentially blind to polarization. Here, we are developing an imaging system capable of extracting almost the complete set of polarimetric properties for partially polarized light in parallel and real time. This sensory system integrates an array of imaging elements, a micropolarization array and analog processing circuitry for polarimetric computation at the focal plane in order to achieve a compact, low power polarization sensitive system.

Biologically inspired, polarization difference (contrast) imaging (PDI) sensors have been one of the dominant research topics in developing polarization sensitive systems [7-10]. Several imaging systems have been made where polarization-contrast information has been computed at the focal plane [7,8] or with bulky, power hungry set-ups composed of CMOS/CCD imaging sensors, electro/mechanically controlled polarization filters and DSPs/CPU's [9-11]. These systems sample the environment via two orthogonal polarization filters and compute contrast information at the focal plane with translinear circuits or in the digital domain with a DSP/CPU. The sampling of the environment is achieved with spatially distributed polarization orthogonal filters over the neighborhood of two pixels or by temporally sampling the scene with two sequential orthogonal filters. Tradeoffs between these two approaches are reduction of spatial resolution in the former vs. reduction of frame rate in the latter system.

Incorporating pixel-pitch-matched polarization filters at the focal plane has been first reported by Andreou et al. [7,12,13], where birefringent materials and thin film polarizers have been explored. The pixel pitch for the birefringent and thin film micropolarizer arrays was 50 μ m and 25 μ m, respectively. The large pixel pitch was limited by the wet isotropic etching technique employed for patterning the thin-film polarization filter and by the in-pixel circuit processing for extracting polarization contrast information in the birefringence imaging system. A birefringent micropolarization element array with pixel-pitch size of 25 μ m and 128 μ m was reported in [14] and [8] respectively. The large pixel pitch in these polarimetric imaging systems limits the fidelity of the imaged environment, which is a major shortcoming for high resolution imaging applications.

Another avenue of research has been the design of micropolarization array for extracting the complete set of polarimetric properties of partially linearly polarized light. A micropolarization array with three spatially distributed polarizers was fabricated and described by Guo et al. [15]. The polymer thin film was used to create a three axial micropolarizer array with 25 micron pixel pitch elements. A dual axel dichroic-on-threated-glass micropolarizer array with 5 μ m pixel pitch and extinction ratio of \sim 330 was reported in [16]. Wire grid micropolarization array for near infrared spectrum have been reported in [17].

The previously reported PDI systems, which have been directly inspired from biological systems, compute polarimetric information in simplified and compact form [7,8,10]. In contrast, the complete polarimetric information tends to be far more complex and its computational demands usually prevent real time extraction [10]. These complex polarization properties are fully described by the four fundamental parameters known as the Stokes parameters. For natural lights, which are usually polychromatic and partially polarized and for which the phase information between the components is not available, only the first three Stokes parameters are needed. In order to fully determine these three Stokes parameters, the imaged scene must be sampled at least with three different polarization filters.

We are developing a high resolution imaging system capable of extracting the first three of the four Stokes parameters from the imaged environment in parallel and in real time. This novel sensory system integrates imaging array with 10 μ m pixel pitch with a photodiode area of 8x8 μ m square, pitch-matched micropolarization array and polarization processing at the focal plane.

In this paper we solely focus on the microfabrication steps necessary for patterning a commercially available thin film polarizer in order to create a dual axel micropolarization array with 8 μ m by 8 μ m square filters. The paper is organized as follows. In Section 2, a theoretical background on light polarization is presented in order to introduce a technique for polarimetric computation at the focal plane. Section 3 presents the micro fabrication steps necessary to manipulate thin film polarizer. RIE effects on the polarizer are theoretically analyzed in Section 4. Experimental data is presented in Section 5 and concluding remarks are summarized in Section 6.

2. Overview of polarization information and Stokes parameters

Stokes parameters can describe the polarization information of light. There are different ways to express Stokes parameters, one of which is presented by Eqs. (1) through (4), which describe fully the polarization state of the electric-field vector [16].

$$S_0 = I_t \quad (1)$$

$$S_1 = 2I(0^\circ, 0) - I_t \quad (2)$$

$$S_2 = 2I(45^\circ, 0) - I_t \quad (3)$$

$$S_3 = I_t - 2I(45^\circ, \pi/2) \quad (4)$$

In Eqs. (1) through (4), I_t is the total intensity; $I(0^\circ, 0)$ is the intensity of the e-vector filtered with a 0 degree polarizer and no phase compensation between the x and y components; $I(45^\circ, 0)$ is the intensity of the e-vector filtered with a 45 degree polarizer and no phase compensation as above; and $I(45^\circ, \pi/2)$ is the intensity of the e-vector filtered with a 45 degree polarizer and $\pi/2$ phase compensator between the x and y components.

It is worth mentioning that the first three Stokes parameters describe the polarization of light, when the phase information between the components is not available. Therefore, in order to describe the polarization state of such light in nature, three linearly polarized projections (for example, 0 degree, 60 degree and 120 degree polarization, or 0 degree, 45 degree and 90 degree) or two (non-orthogonal) linearly polarized projections in combination

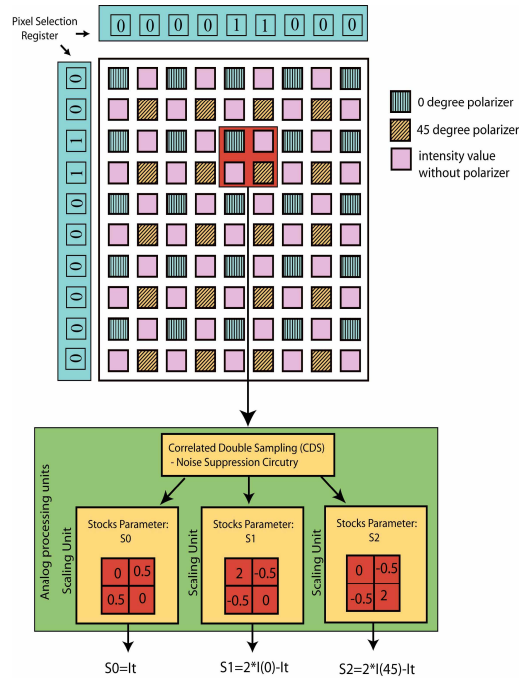


Fig. 1. Block diagram of the complete imaging system: imaging array, processing circuitry and micropolarization array

with the total intensity are needed. The latter method is preferred for focal plane implementation since it only requires two thin film polarizers offset by 45 degrees, patterned and placed on neighboring pixels. The overall thickness of the complete filter will be thinner for a two-tier vs. a three tier filter, which has two main advantages. The first advantage is in minimizing light attenuation through multiple layers and increasing the angle of incidence. The second advantage is in reduction of fabrication steps and minimization of alignment errors

The patterning of the thin film polarizer is similar to the Bayer pattern used in color imaging and it is shown in Fig. 1 together with the image sensor. The image sensor is composed of an array of 256 by 256 photo pixels, and the noise suppression and analog computation circuitry is included at the focal plane. The micropolarizer array is separately attached on the image sensor with the pattern shown in Fig. 1.

In the image sensor presented in Fig. 1, a neighborhood of 2 by 2 pixels is addressed and accessed simultaneously. In the pixels neighborhood of interest, one pixel records the 0 degree projected polarized image ($I(0^\circ, 0)$), another records the 45 degree projected polarized image ($I(45^\circ, 0)$) and two pixels record the unfiltered intensity image (I_t). The polarimetric parameters are estimated by reading out all four pixels in parallel [18] and scaling them individually at the periphery, i.e. away from the imaging array, with programmable analog scaling circuitry in accordance to the first three Stokes parameter equations (Eqs. (1) through (3)). The details of the addressing scheme of block of 2 by 2 pixels and analog processing circuitry are described in [18,19].

3. Micro fabrication steps for thin film polarizer manipulation

A commercially available thin film polarizer is used to create an array of micropolarizers. The thin film polarizer consists of an iodine-doped Polyvinyl Alcohol (PVA) layer, which acts as a dense array of thin microscopic wires. These microscopic wires are formed by mechanically stretching the polymer film, allowing the molecules of the PVA to align in the direction of stretching. In order to have an effective polarizer, the size and spacing between the thin

microscopic wires should be $\sim 1/100^{\text{th}}$ and $\sim 1/10^{\text{th}}$ of the light's wavelength, respectively [20]. For example, for blue light wavelengths or 450nm wavelength, the distance between the microscopic wires should be on the order of 45nm, while the thickness of the wires should be around 5nm. The mechanical stretching of the polymer creates a very good $\sim 10\mu\text{m}$ thick polarization filter for the visible spectrum, with extinction ratios of about 1000 in the blue and green spectrum and 100 in the red spectrum. The PVA thin film is placed between two $300\mu\text{m}$ thick transparent Cellulose Acetate Butyrate (CAB) or polyethylene layers (Fig. 2-a). The CAB layers provide structural stability to the fragile and thin PVA layer.

In order to be able to manipulate the PVA layer, at least one of the protective CAB layers must be removed. Since CAB is a form of acetate, it is therefore acetone soluble. Hence, the sample is submerged in an acetone bath for 30 minutes. One side of the sample is taped with an acetone resistant tape, i.e. rubber tape, to a glass substrate in order to protect the bottom layer of CAB which provides structural stability for the PVA layer. The sample is rinsed with de-ionized water (DI) in order to remove the soft CAB layer. The DI water also solidifies the CAB layer, upon which the sample is submerged in the acetone bath again. These two steps are repeated several times, until no residual CAB layer remains on top of the PVA layer (Fig. 2-b).

The next step is to glue the PVA to a substrate. In the final imaging system, the PVA will be glued directly to the die of the imaging system. For testing purposes, however, the PVA is glued to a microscopic glass in order to be able to back illuminate the filter and to fully characterize the optical properties of the micropolarizer elements. A UV sensitive adhesive promoter, Dymax AD420 [21], is used between the PVA and the IC/Glass substrate (Fig. 2-c). The UV adhesion promoter has 95% transparency, which allows for minimal absorption of the impinging light wave. The adhesive promoter exhibits minimum expansion when heated and it has an important property for preserving the extinction properties of the PVA layer.

The next step is to remove the bottom CAB layer in order to allow patterning the PVA film. This step is similar to the initial step, where a repeated acetone bath and DI water rinsing are used. The final structure after this process is shown in Fig. 2-d.

The remaining steps describe the patterning and etching process of the PVA. These steps are as follow:

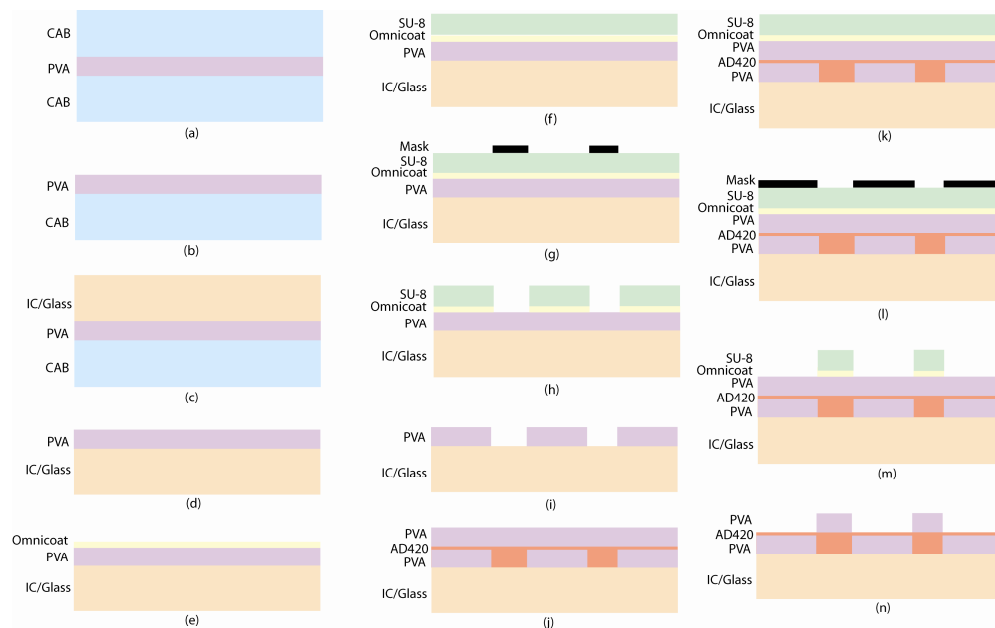


Fig. 2. Microfabrication steps for creating a dual layer polarization structures

(1) Heat the sample to a temperature of 95°C for 5 minutes. This ensures that the surface of the PVA is completely dry. An adhesion promoter, Omnicoat [22], is applied directly and spin coated at 3000 rpm for 60 seconds. The sample is then baked for 1 minute at 95°C. The Omnicoat layer promotes adhesion between the PVA and the SU-8 photoresist (Fig. 2-e).

(2) Immediately apply an SU-8 2015 negative photoresist [22] on top of the PVA. The negative photoresist is hydrophobic and requires the surface of the PVA to be absolutely free of any water molecules. If the sample is cooled down to room temperature, water molecules due to humidity will coat the surface of the PVA. The adhesion of the SU-8 will be virtually non-existent when patterning 10µm or smaller structures. Larger structures tend not to have problems with adhesion when the PVA is cooled down to room temperature.

(3) Spin coat the photoresist at 500rpm for 10 seconds and then at 3000 rpm for 50 seconds with 500 rpm per second acceleration. The resulting photoresist thickness is 3µm.

(4) Bake the sample at 65°C for 1min and then at 95°C for 2min. It is recommended that the sample cools down at 65°C for 1 min in order to gradually decrease the temperature of the sample. Gradual increase and decrease of the temperature during the baking process avoids rapid temperature differences and prevents the photoresist from cracking (Fig. 2-f).

(5) Expose the photoresist at 375nm wavelength for 20 seconds at 8mW/cm² intensity. The mask used to pattern features for the imaging sensor contains 10 µm by 10 µm square patterns (Fig. 2-g). This mask allowed us to closely evaluate isotropic etching properties using an electron scanning microscope.

(6) Post-bake the sample at 65°C for 1 min and then at 95°C for 2 min. The sample is cooled down at 65°C for 1 min in order to gradually decrease the temperature and minimize stress and cracking on the photoresist.

(7) Develop the photoresist for 4 min in an SU-8 developer and gently rinse it with isopropyl alcohol. If white colored liquid appears on the surface, the photoresist is not completely developed and it is submerged in the developer again (Fig. 2-h).

(8) Selective reactive ion etching is performed on the sample. A mixture of gasses composed of 28 sccm Ar, 30 sccm O₂ and 10 sccm CF₄ is used. The RF power is 150W, at 17°C temperature and 20mbar pressure. The selected ratio of the appropriate gasses is optimized to maximize the etching of the PVA while minimizing the destructive etching of the SU-8 photo resist. The etching rate of the PVA is 0.5µm/min, while the etching rate of the SU-8 is 0.75µm/min. Since the thickness of the PVA is ~10µm, the sample is etched for ~20 minutes. The thickness of the SU-8 is optimized to be 15µm and it will be etched completely by the time the PVA layer is etched. This optimization simplifies the microfabrication procedure at the cost of slightly damaging the PVA structures which might occur due to variations in the PVA and SU-8 thickness.

A more conservative approach can be employed, where the SU-8 thickness can be increased above 15µm. Once the etching of the PVA layer is completed, the remaining photoresist can be removed with an SU-8 photoresist stripper. The Omnicoat layer helps lift the SU-8 photoresist and remove it from the PVA structures. The RIE provided anisotropic etching with ~1µm under cutting, compared to 4µm and 10µm under cutting with oxygen plasma and wet etching, respectively (Fig. 2-i).

The next step is to add a second layer of PVA on top of the first layer offset by 45 degrees via a UV adhesive promoter and etch it with the desired mask pattern. First, the adhesive promoter is spin coated at 1500rpm for 60 seconds ensuring ~1µm epoxy layer on top of the first PVA layer. The second PVA layer is placed under an angle starting from one end of the sample and it is gradually lowered toward the other side of the sample. This step helps in eliminating air bubble being trapped in the epoxy layer as well as planarization is achieved due to the liquid state of the epoxy layer.

As an alternative method of merging the two PVA layers, we placed the adhesive promoter on top of the first PVA layer without being spin coated. The second PVA layer is gradually lowered toward the first layer while maintaining parallel alignment of the two layers. Once an initial contact is established between the adhesive promoter and the second

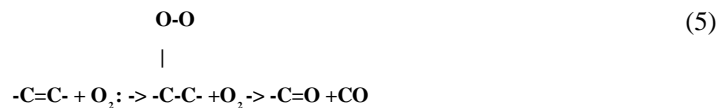
PVA layer, due to the dispersion forces of the adhesive promoter, the adhesive promoter flows to the periphery of the sample without any air bubbles being trapped. The excess adhesive promoter will flow outside the sample as the top layer is lowered toward the first layer. When the second PVA layer is completely pressed against the first layer, the sample is exposed with UV light. This procedure was performed using an aligner, where the control of the contact pressure can be used to vary the thickness of the adhesive promoter layer. In both cases reliable repeatability of merging the two PVA layers was achieved with adhesive layer of $\sim 1\mu\text{m}$.

Following the adhesion procedure, the top CAB layer is removed with acetone in order to be able to pattern the PVA layer. This step is similar to the initial step, where a repeated acetone bath and DI water rinse is used. The final structure after this process is shown in Fig. 2-j. The remaining steps for patterning the top layer of PVA are identical to the one for patterning the bottom layers. These steps are shown in Fig. 2-k through Fig. 2-n. The final two-axial micropolarization filter is shown Fig. 2-n, with a total thickness of around $20\mu\text{m}$.

Alignment structures were used on both the PVA layer and the CMOS imager, in order to properly align the various layers. The first layer of PVA was aligned on the CMOS image sensor using four alignment makers on the corners of the image sensor. The second PVA layer was aligned with the first PVA layer using different sets of alignment makers placed throughout the sample in order to increase precision.

4. Reactive Ion Etching (RIE) Effects on the PVA

Cold plasma or RIE has been widely used to modify or etch polymers. The etching process of polymers is linearly dependent on the concentration of the atomic-oxygen free radicals [23] or on the number of oxygen atoms consumed during the etching process [24]. Since the PVA is an unsaturated polymer, the etching process is represented as addition to unsaturated moieties [24,25]. The addition of oxygen to the unsaturated PVA creates a saturated radical with a weakened C-C bond. Any subsequent attack by free oxygen radicals will break the C-C bond and it will divide the saturated molecule. Carbon monoxide (CO) and carbon dioxide (CO₂) are released during the etching procedure (equation 5).



In order to increase the etching rate of the PVA, the concentration of oxygen atoms must be increased. This is achieved with the addition of fluorine gases, such as CF₄, CF₃, C₂F₆, SF₆ and others. In our experiment, CF₄ was used. The enhanced etching rate is due to the increased density of electrons, as well as increased energy of electrons in the RIE. At the molecular level, the addition of fluorine atoms further weakens the C=C bond of the PVA molecule and it creates a saturated radical prone to chain scission. The fluorine gases combine with the carbon and oxygen atoms and create a fluorinated ethane and ethylene derivative. These stable fluorine products remain on the surface of the PVA. If the concentration of the fluorine atoms is increased beyond a threshold, fluorinated ethane will have retarding effects on the etching rate. The fluorinated ethane has to be removed before reaching the PVA surface and etching the PVA surface. Hence, the etching rate exhibits a maximum for a given concentration ratio of O₂ and CF₄ and it rapidly decreases with the increase or decrease of the CF₄ concentration.

We have performed experiments where the concentration of CF₄ was varied in order to determine the optimum etching rate. From Fig. 3, we can observe that for 30% of CF₄ in a total mixture of O₂ and CF₄, the PVA exhibits a maximum etching rate. Deviations from this optimal concentration have retarding effects on the etching rate as it is expected from the theory. Since the SU-8 photoresist is a polymer, it also exhibits similar etching behavior as the PVA. Due to its different molecular composition, the SU-8 has slightly higher etching rate than the PVA. This should be taken into account for the final thickness of the SU-8, as the

SU-8 acts as protective layer for the PVA and it should remain until the unprotected PVA is etched completely. From the experimental data, an Oxygen-to-Freon (CF_4) ratio of 3:1 yields an optimum etching results. For this gases concentration, the etching rate of the SU-8 is $0.75\mu\text{m}/\text{min}$, while the etching rate for the PVA is $0.5\mu\text{m}/\text{min}$. High etching rate and low selectivity was chosen in order to minimize the etching time of the PVA layer and hence minimize the under etching.

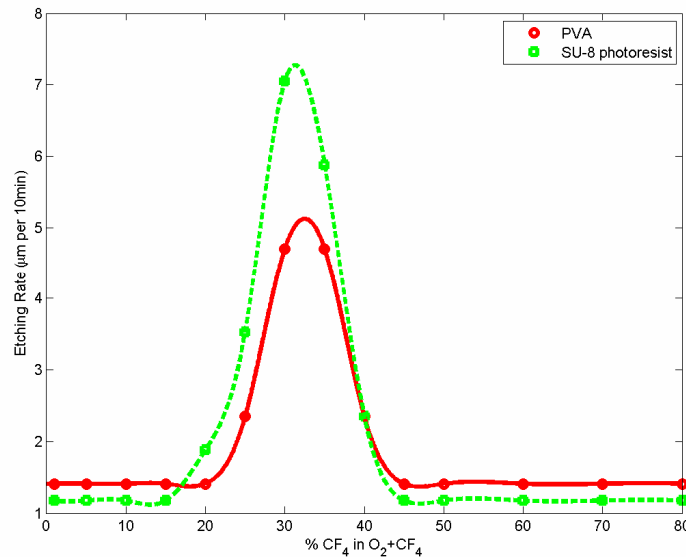


Fig. 3. Etching rate of PVA and SU-8 as a function of a CF_4 concentration in an O_2 and CF_4 gas mix.

5. Dual-tier micropolarization array: Experimental results

The final two-tier micropolarization array was tested for its structural and optical properties. A scanning electron microscope (SEM) was used to evaluate the photoresist and the etched PVA structures. A comparison of the size of both structures indicated the amount of under-etching due to the selective RIE procedure.

In Fig. 4-a and Fig. 4-b, the SU-8 square structures obtained after the photolithography procedure (see Fig. 2-h) are presented. Fig. 4-a presents the photoresist structures viewed from the top, while Fig. 4-b present an array of photoresist pillars recorded under 52 degree angle tilt. The photoresist squares are $10\mu\text{m}$ by $10\mu\text{m}$ wide and $15\mu\text{m}$ tall, with $10\mu\text{m}$ spacing between neighboring structures. The corners of the square structures are slightly rounded due to edge diffraction effects from the mask. The rounding effects are minimized by optimizing pre-baking, post-baking and exposure time of the photoresist. The uniform periodic structures are observed in Fig. 4-b.

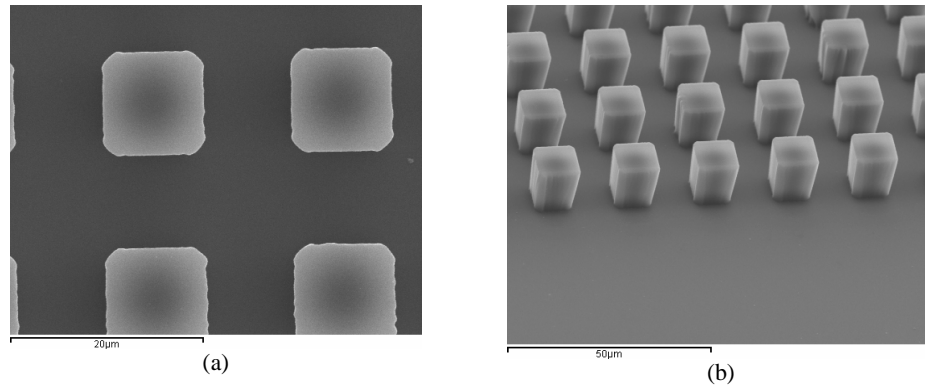


Fig. 4. Scanning electron microscope images of the developed SU-8 photoresist structures. Left panel shows a top view of a small neighborhood of SU-8 squares with $10\mu\text{m}$ by $10\mu\text{m}$ pitch. Right image shows an array of periodic SU-8 square structures with $15\mu\text{m}$ thickness, which was recorded under 52° angle tilt.

After the selective reactive ion etching of the top PVA layer (see Fig. 2-n), the micropolarization structures were evaluated under an SEM. Fig. 5-a and Fig. 5-b present the top PVA layer of the complete two-tier filter. The left panel presents a top view of a small neighborhood of micropolarizer structures. The square PVA structures have $8\mu\text{m}$ by $8\mu\text{m}$ size with $12\mu\text{m}$ spacing between neighboring structures. Therefore, the undercutting due to the RIE is $1\mu\text{m}$ per side and the final size of the PVA square structures has decreased by $2\mu\text{m}$ from the original $10\mu\text{m}$ photoresist structures. Readjusting the size of the squares on the mask (i.e. photoresist structure) to $12\mu\text{m}$ will lead to $10\mu\text{m}$ PVA square structures. Since, our photo pixel has a fill factor of 64% (i.e. the photodiode area is $8\mu\text{m}$ by $8\mu\text{m}$), the obtained size of the PVA structures satisfied the minimum size requirements.

The right image in Fig. 5, which was recorded under 52° angle tilt, presents a single PVA micro structure of size $8\mu\text{m}$ by $8\mu\text{m}$ and $10\mu\text{m}$ thickness. The PVA structure does not contain any residual SU-8 photoresist since the thickness of the photoresist was optimized to be completely etched away during the selective RIE procedure. Furthermore, we can observe that the top of the PVA structure is not smooth, which indicates that it has been partly etched. This is a result of small variations in the PVA thickness as well as variations in the SU-8 photoresist. Hence, precise etching time for the PVA can not be determined. The top of the PVA structures was spin coated with an adhesive promoter AD420 since it has an index of refraction similar to the PVA ($n=1.41$). This prevented any undesirable diffraction which might occur at the surface of the PVA. Although the top portion of the PVA has been etched (around $0.3\mu\text{m}$ from the $10\mu\text{m}$ total thickness), the optical measurements of the PVA structures have shown that the extinction ratios have been preserved during the etching procedure.

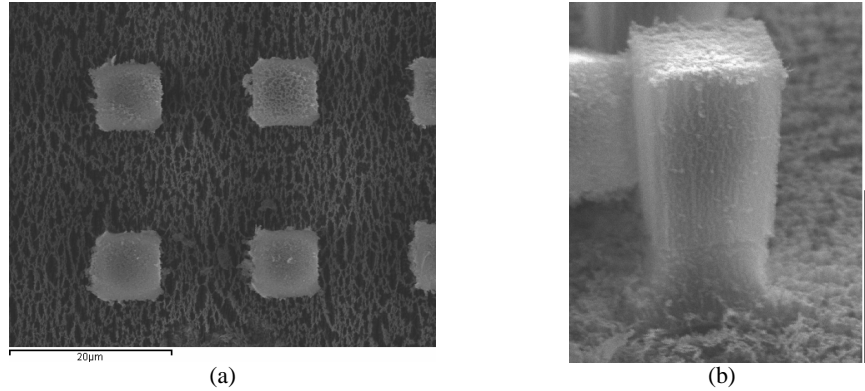


Fig. 5. Scanning electron microscope images of the top PVA tier. Left image shows an array of $8\mu\text{m}$ by $8\mu\text{m}$ PVA structures. Right panel shows a single PVA structure with $8\mu\text{m}$ pitch and $10\mu\text{m}$ thickness, which was recorded under 52° angle tilt.

The optical properties of the dual-tier micropolarization filter were evaluated under an optical microscope via back polarized illumination of the sample with three different wavelengths: 720nm wavelength (red light), 580nm wavelength (green light) and 480nm wavelength (blue light). We have created two samples of a dual-tier micropolarization filter. In the first sample the two layers of micropolarizers are offset by 90° , while in the second sample they are offset by 45° . The second sample contains the desired pattern which will be integrated with a CMOS image sensor in order to extract the first three Stokes parameters. The first sample was used for measurement purposes and for visual clarity, although it can be used for a polarization difference (contrast) computation [4,9,10].

The optical characteristics of the dual axial micropolarizers offset by 90° are presented in Fig. 6. In Fig. 6-a, the sample was illuminated with polarized light having polarization perpendicular (parallel) to the transmission axis (axis of polarization) of the PVA structures in the first tier. The square structures in the first tier appear bright in intensity and little darker compared to the background since the PVA attenuates part of the parallel polarized light (PVA transmission of about 40% has been measured and reported in the literature [26]). The square structures in the second tier appear opaque. They attenuate the intensity of the incoming light waves since their axis of polarization is oriented perpendicular to the polarization of the incident polarized light. In Fig. 6-b the sample was illuminated with polarized light perpendicular (parallel) to the transmission axis (axis of polarization) of the

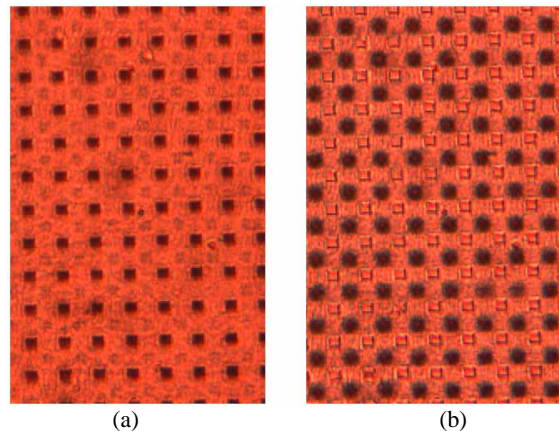


Fig. 6. Experimental results for the dual-tier micropolarization filters offset by 90° . The first layer in the left sample attenuates perpendicular polarized light while the second layer is transparent. The reverse is observed in the right sample.

PVA structures in the second tier. The reverse effects are observed in this image, where the top layer is opaque and the bottom layer is transparent due to the 90 degree polarization offset of the illuminating light source.

Since the square structures in the dual axial filter reside in different tiers separated by $10\mu\text{m}$ and the images were taken under a microscope with $5\mu\text{m}$ depth of focus, the contours of the square structures in the bottom tier appear slightly blurred. Refocusing the microscope to image the bottom tier structures verified the sharpness of the squarely-etched structures. Since the final thickness of the dual axial filter is $\sim 20\mu\text{m}$, the angle of incidence of the incoming light will be limited. For example, for large angles of incidence, the incoming light will be filtered with one micro filter and registered by a neighboring pixel on the CMOS image sensor. Using thinner layers will reduce this effect. In addition, introducing micro lenses on top of the micropolarization array in the future will circumvent this problem.

The optical characteristics of the dual-axial micropolarizers offset by 45 degrees are presented in Fig. 7. The images in Fig. 7-a, 7-b, 7-c and 7-d are recorded with 0, 45, 90 and 135 degrees of polarized light, respectively. In Fig. 7-a (Fig. 7-c), the sample was illuminated with polarized light with polarization parallel (perpendicular) to the transmission axis of the PVA structures in the first tier i.e. with 0 (90) degree polarized light. Hence, the square structures in the first tier appear opaque in intensity in Fig. 7-a and transparent in Fig. 7-c. Since the second tier is offset by 45 degrees, it is difficult to visualize its relative offset. The polarization properties of the second tier are clearly evident in Fig. 7-b and Fig. 7-d. In Fig. 7-b (Fig. 7-d), the sample was illuminated with polarized light parallel (perpendicular) to the transmission axis of the PVA structures in the second tier i.e. with 45 (135) degree polarized light. Hence, the square structures in the second tier appear opaque in intensity in Fig. 7-b and transparent in Fig. 7-d.

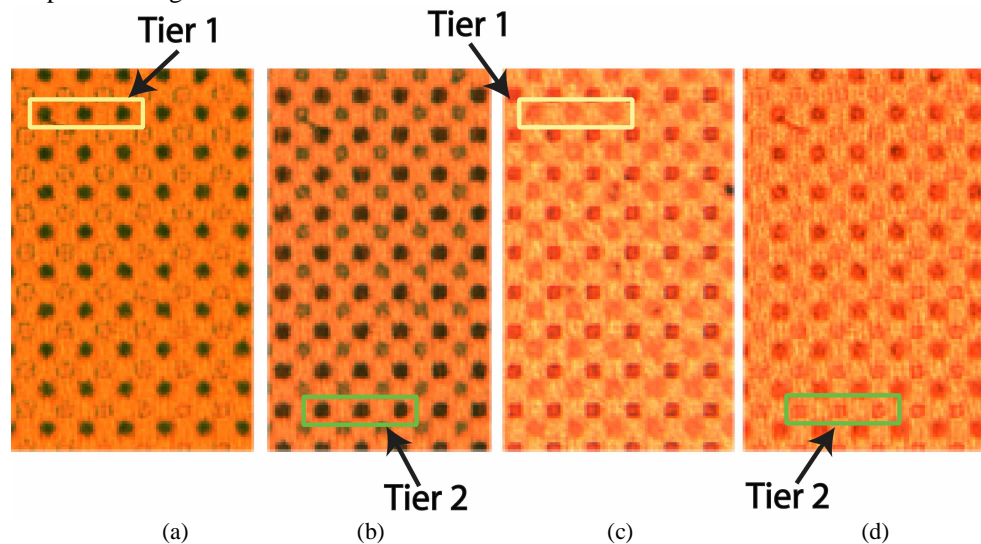


Fig. 7. Experimental results for the two axial micropolarization filters offset by 45 degrees. The images are illuminated with 0, 45, 90 and 135 degree polarization for the incident polarized light, respectively.

Figure 8 and Fig. 9 present movies, demonstrating the polarization filtering capabilities of the dual-tier and single-tier micro-structured PVA, respectively. The offset of the two-tier samples is 45 degrees. The movie files are composed of 36 frames, where the angle of polarization of the light source is varied between 0 degrees and 180 degrees in increments of 5 degrees between frames. The filter was illuminated with red-light wavelength in both examples; hence the transparent background of the sample appears red. The samples were illuminated with all three wavelengths separately in order to evaluate the dependence of the extinction ratios on the wavelength, but for the sake of brevity only one wavelength is

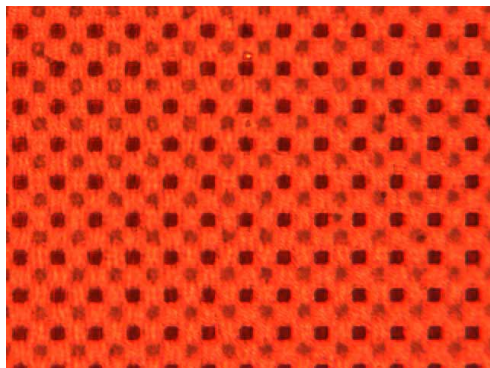


Fig. 8. (3 MB) Movie of the dual axial micropolarizer array (13MB version).

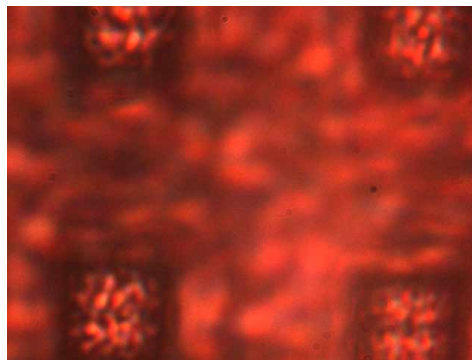


Fig. 9. (3 MB) Movie of a single micropolarizer element (12MB version).

presented here in the movie files. In Fig. 8, it can be observed that initially the bottom layer is transparent and the top layer is opaque. As the angle of polarization is varied between frames, the transparency shifts from the top PVA tier to the bottom PVA tier. Since the data was taken while focusing on the PVA structures on the top tier, the PVA structures in the bottom tier appear slightly blurred and unfocused. In Fig. 9, we observe the polarization behavior of a single PVA tier. The PVA structure gradually changes from transparent to opaque as the angle of polarization is changed. In this Fig., we can closely monitor that the effective size of the PVA structures is $8\mu\text{m}$ by $8\mu\text{m}$, demonstrating anisotropic under-etching of $1\mu\text{m}$ during the RIE procedure.

The two-tier filter, where the tiers were offset by 90 degrees, was also recorded with a 12 bit grayscale camera. Since the extinction ratio of the un-patterned PVA is around 1000 [26], the sensitivity of the imaging devices has to be at least 10 bits or higher. Two regions of 10 by 10 pixels were selected in Fig. 8, which corresponded to two PVA structures in separate tiers. The average intensity value was computed and normalized to the incident light intensity on the filter. The data was recorded over 36 frames, where the angle of polarization was incremented by 5 degrees between frames. The transmission properties of both tiers, presented in Fig. 10, closely follow Malus' cosine law for polarization irradiance [1]. Since the two PVA layers were offset by 90 degrees, the maximum and minimum transmissions between the two-tiers are expectedly shifted by 90 degrees.

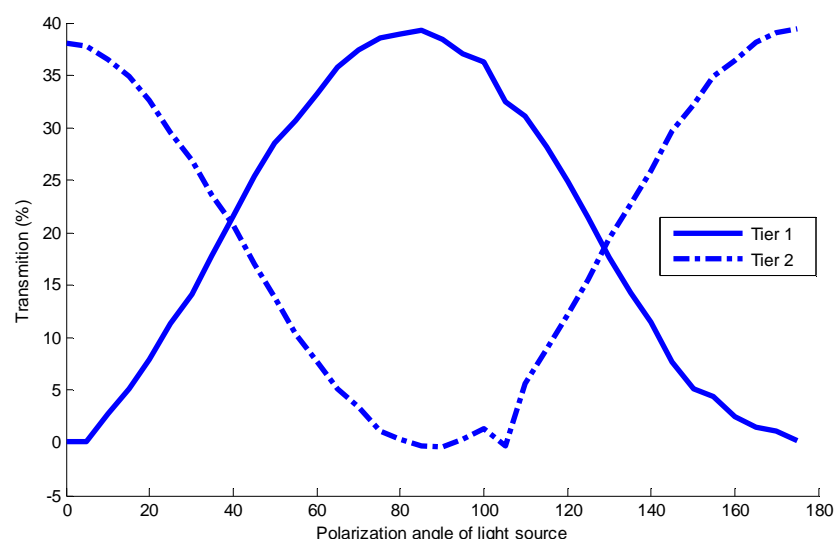


Fig. 10. Transmission of both PVA structures follow Malus' law for polarization irradiance

The extinction ratios for the patterned PVA structures were also evaluated at three different wavelengths. Figure 11 presents the transmission percentage as a function of the angle of polarization for three different wavelengths. Also, transmission data for an unpatterned PVA sample was recorded and presented with black dotted line in Fig. 11. From this data, the extinction ratios, defined as the ratio of the maximum to minimum transmission for a given wavelength, were calculated. The maximum transmissions for red and blue wavelength were recorded to be 45% and 40% respectively. The minimum transmissions for the red and blue wavelength were recorded to be 0.4% and 0.04% respectively. Therefore, the extinction ratio for blue and green wavelengths is ~1000 and for red wavelengths the extinction ratio is ~100. The extinction ratios for unpatterned PVA evaluated with red wavelength is ~100. The data in Fig. 11 demonstrates that the polarization properties of the micropolarization PVA structures, created using selective RIE are not altered and they are similar to the polarization properties of an unpatterned and an un-etched PVA filter.

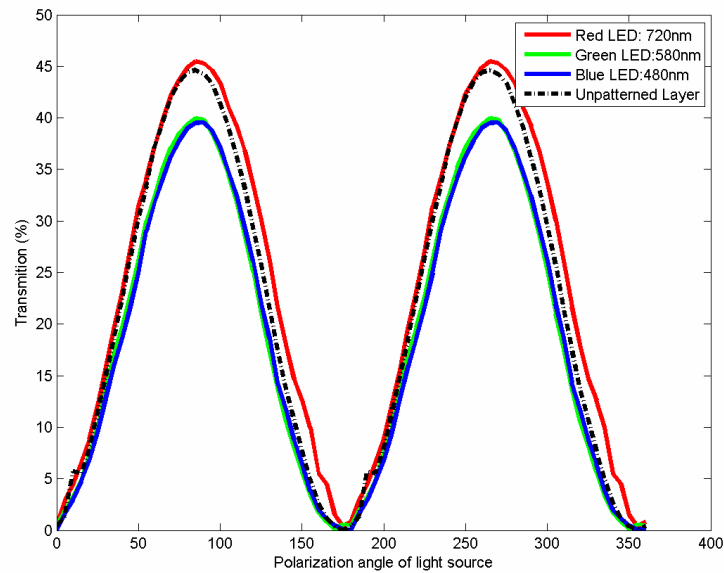


Fig. 11. Transmission of a single PVA micro structure under different wavelengths. The transmission properties of unpatterned PVA are also presented.

6. Conclusion

An outline of a novel polarization filtering architecture for real time polarimetric imaging has been described. This sensory system requires accurate patterning of thin film polarizers. We have outlined the methodology necessary to pattern and etch $10\mu\text{m}$ -thick PVA polarizer in order to create $8\mu\text{m}$ by $8\mu\text{m}$ square structures. These methods would allow patterning of polarization micro structures necessary to be placed on top of an imaging sensor. The extinction ratios of the polarization filter are around 1000 for blue and green wavelength and 100 for red wavelengths. In our next phase of research efforts, the final array of micropolarizer will be mounted on top of a custom made image sensor for real time polarimetric computation.

Acknowledgments

This work is support in part by U.S. Air Force Office of Scientific Research (AFOSR) grant number FA9550-05-1-0052. The authors like to acknowledge the support of ATMEL and NSF through an REU grant (No. EEC-0244055).